UNIVERSITY OF CALIFORNIA, SAN DIEGO

Geophysical Inversion with Adaptive Array Processing of Ambient Noise

A dissertation submitted in partial satisfaction of the
requirements for the degree
Doctor of Philosophy

in

Oceanography

by

James Traer

Committee in charge:

Doctor Peter Gerstoft, Chair
Professor William Hodgkiss
Professor William Kuperman
Professor Michael Buckingham
Professor Peter Shearer
Professor Barnaby Rickett
Doctor Peter Bromirski
Doctor Hee Chun Song

2011

The dissertation of James Traer is approved, and it is acceptable in quality and form for publication on microfilm and electronically:

_____

_____

_____

_____

_____

_____

_____

_____

Chair

University of California, San Diego

2011

DEDICATION

To my family. To my friends. To DSDP 220 and asymptotic matching. To the memory of Tim Ray, Hans Morsbach, Jim Staab and Jeff and Ilona Njus.

EPIGRAPH

The universe is full of magical things patiently waiting for our wits to grow sharper.

—Eden Phillpotts, A Shadow Passes

TABLE OF CONTENTS

LIST OF FIGURES

ACKNOWLEDGEMENTS

Thanks, first and foremost, to my adviser and mentor, Peter Gerstoft, for patiently correcting all the flawed manuscripts I have placed on his desk over the years and for kindly letting me win most of our races on the beach. Thanks to my committee for their time, their interest and their feedback. Thanks to my co-authors for all their help and their indispensable contributions. Thanks to my officemates, past and present, who have helped solve many of the problems my research presented and, failing that, they patiently listened to me vent. Thanks to the MPL computer administrators for their help and measured reprimands whenever I crashed the network or filled a hard drive with a terabyte of error messages. Thanks to Evelyn Doudera and Norissa Gastelum both for keeping the lab running and making it a joyful environment. Thanks to Krystle Shertz, Josh Reeves and Denise Darling for their kindness, good humor and tireless help with all my administrative paperwork.

Thanks to Glenn Ierley, Bill Young, Daniel Tartakovsky, Ken Kreutz-Delgado, Rick Salmon, Myrl Hendershott, Bob Guza, Bill Hodgkiss, Bill Kuperman, Mike Buckingham, Paul Dayton, Ken Melville, Dariusz Stramski, LeRoy Dorman, Peter Shearer, Guy Masters, Peter Franks, Clint Winant and Lynne Talley who taught me much of what I know of physics, mathematics and the ocean.

Thanks to the Cornell University Center for Advanced Computing for giving me the keys to their supercomputer cluster so I could continue to run CPU-intensive projects even after I'd crashed the MPL network.

Chapter 2, in full, is a reprint of the material as it appears in the Journal of the Acoustical Society of America 2008. Traer, James; Gerstoft, Peter; Bromirski, Peter D.; Hodgekiss, William S.; Brooks, Laura A., Acoustical Society of America, 2008. The dissertation author was the primary investigator and author of this paper.

Chapter 3, in full, is a reprint of the material as it appears in the Journal of the Acoustical Society of America 2009. Traer, James; Gerstoft, Peter; Song, Hee C.; Hodgekiss, William S., Acoustical Society of America, 2009. The dissertation author was the primary investigator and author of this paper.

Chapter 4, in full, is a reprint of the material as it appears in the Journal of the Acoustical Society of America 2011. Traer, James; Gerstoft, Peter; Hodgekiss, William S., Acoustical Society of America, 2011. The dissertation author was the primary investigator and author of this paper.

Chapter 5, in part, is a reprint of material to be submitted for publication to the Journal of the Acoustical Society of America in 2011.

VITA

2005	B. S. in Physics, University of Cambridge, UK
2006	M. S. in Physics, University of Cambridge, UK, awarded Neville-Mott Prize for best experimental project in the Cavendish labs (2006)
2011	Ph. D. in Oceanography, University of California, San Diego

PUBLICATIONS

J. Traer, P. Gerstoft, P. D. Bromirski, W. S. Hodgkiss and L. A. Brooks, "Shallow-water seismoacoustic noise generated by tropical storms Ernesto and Florence," J. Acoust. Soc. Am. **124**, EL170–EL176 (2008).

J. Traer, P. Gerstoft, H. C. Song and W. S. Hodgkiss, "On the sign of the adaptive passive fathometer impulse response," J. Acoust. Soc. Am. **126**, 1657–1658 (2009).

J. Traer, P. Gerstoft and W. S. Hodgkiss, "Ocean bottom profiling with ambient noise: A model for the passive fathometer," J. Acoust. Soc. Am. **129**, 1825–1836, (2011).

ABSTRACT OF THE DISSERTATION

Geophysical Inversion with Adaptive Array Processing of Ambient Noise

by

James Traer

Doctor of Philosophy in Oceanography

University of California, San Diego, 2011

Doctor Peter Gerstoft, Chair

Land-based seismic observations of microseisms generated during Tropical Storms Ernesto and Florence are dominated by signals in the 0.15–0.5Hz band. Data from seafloor hydrophones in shallow water (70m depth, 130 km off the New Jersey coast) show dominant signals in the gravity-wave frequency band, 0.02–0.18Hz and low amplitudes from 0.18–0.3Hz, suggesting significant opposing wave components necessary for DF microseism generation were negligible at the site. Both storms produced similar spectra, despite differing sizes, suggesting near-coastal shallow water as the dominant region for observed microseism generation.

A mathematical explanation for a sign-inversion induced to the passive fathometer response by minimum variance distortionless response (MVDR) beamform-

ing is presented. This shows that, in the region containing the bottom reflection, the MVDR fathometer response is identical to that obtained with conventional processing multiplied by a negative factor.

A model is presented for the complete passive fathometer response to ocean surface noise, interfering discrete noise sources, and locally uncorrelated noise in an ideal waveguide. The leading order term of the ocean surface noise produces the cross-correlation of vertical multipaths and yields the depth of sub-bottom reflectors. Discrete noise incident on the array via multipaths give multiple peaks in the fathometer response. These peaks may obscure the sub-bottom reflections but can be attenuated with use of Minimum Variance Distortionless Response (MVDR) steering vectors.

A theory is presented for the Signal-to-Noise-Ratio (SNR) for the seabed reflection peak in the passive fathometer response as a function of seabed depth, seabed reflection coefficient, averaging time, bandwidth and spatial directivity of the noise field. The passive fathometer algorithm was applied to data from two drifting array experiments in the Mediterranean, Boundary 2003 and 2004, with 0.34 s of averaging time. In the 2004 experiment, the response showed the array depth varied periodically with an amplitude of 1 m and a period of 7 s consistent with wave driven motion of the array. This introduced a destructive interference which prevents the SNR growing with averaging time, unless the motion is removed by use of a peak tracker.

Chapter 1

Introduction

1.1 Background

The scale of geophysical systems, such as the Earth's oceans, crust and interior, range from 10's of meters to thousands of kilometers and powerful acoustic transmitters are required to map these large scales. Such active source profiling, in which a signal is transmitted into the ocean or crust and measured by receivers some distance away, remains the most effective way to probe the Earth. Such techniques have been used for seabed mapping, oceanic exploration for mineral and hydrocarbon deposits, mapping the Earth's crust for structural information and to measure the structure and stress distribution around fault lines. Measurements of the deep Earth, once done with nuclear explosions, now require data from large earthquakes which are sporadic, irregular and produce complicated and unknown source waveforms. Acoustic tomography has been proposed as a method to map deep ocean temperatures across global scales.

In all the aforementioned measurements, ambient noise is ubiquitous and for many years has been considered a nuisance to be overcome. However, in the last decade it has been shown that the cross-correlation of ambient noise detected by two sensors can be related to the Green's function between the two sensor locations. Thus ambient noise correlations can extract the same information as active source experiments with the source element/array replaced by a sensor element/array. This has been demonstrated in helioseismology[1], ultrasonics [2],

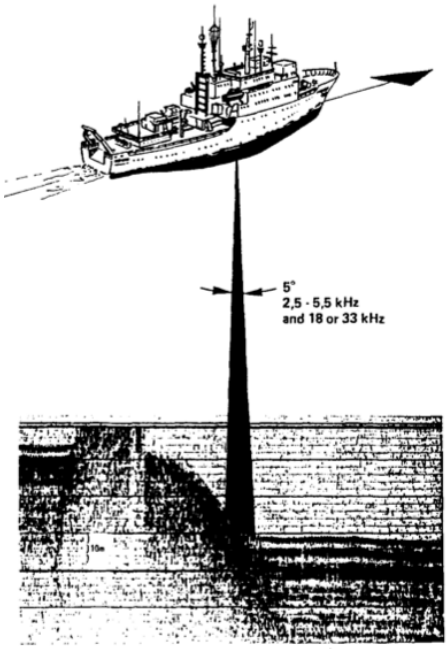

Figure 1.1: Seabed profiling with an active source. Ref. [7]

ocean acoustics[3] seismics [4] and theoretically[5, 6].

Ambient noise correlation has been the subject of much work in recent years. It has been shown that given a diffuse noise field and infinite averaging time the noise cross-correlation, or its derivative, or partial derivative, depending on the dimensionality of the system[8], yields a series of peaks. The location of these peaks gives the travel-time between the sensors from which the average wave-speed in the medium and the internal structure is inferred. A theoretical model has been put forth to describe the effect of the correlation peak SNR as a function of averaging time [9] but little experimental data has been published on this matter. Most work to date has focused on interpreting the peak locations and little has been published on extracting information from the correlation peak amplitudes.

Sensor arrays offer an increase in spatial resolution and an ability to extract low-amplitude noise "signals", incident from a specific direction, from an arbitrary omnidirectional "interfering" noise field. Adaptive array processing techniques can be used to create nulls in the directional sensitivity of the array which can attenuate

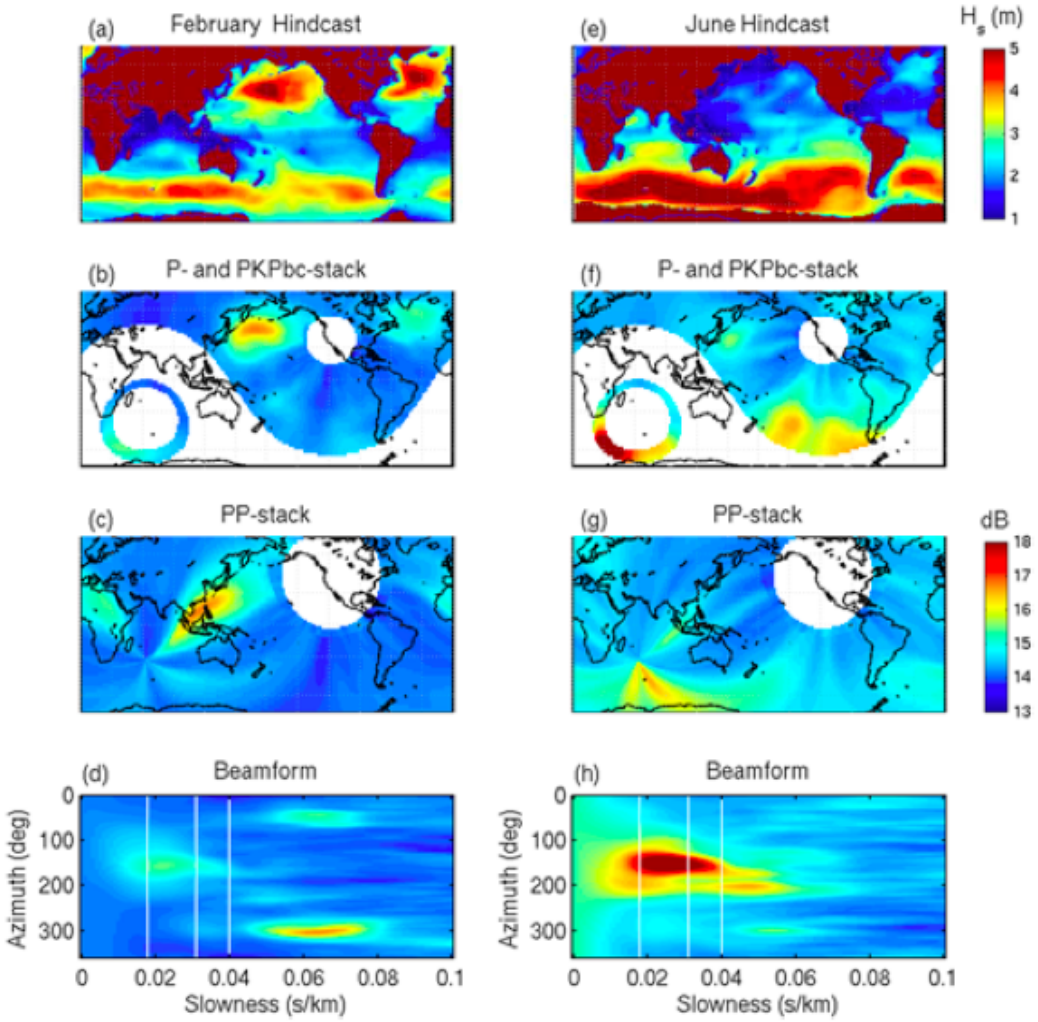

Figure 1.2: Global ocean significant wave heights in (a) February and (e) June. The microseism signals detected from (b),(f) the direct path and after reflecting off the Earth's core. (c),(g) The microseism signals detected after a single reflection from the Earth's surface. (d),(h) The beamform response from the array in Southern California. Ref. [12]

the contribution from strong directional interferers[10]. Seismic arrays have been used to track oceanic storms which generate seismic signals between 0.01–0.1 Hz [11], known as microseisms. Such signals can be detected even after undergoing reflections off boundary layers within the deep earth[12]. The passive fathometer, a technique that has received considerable interest in recent years[13, 14, 15, 16, 17, 18, 19] employs a vertical drifting array to extract vertically propagating noise produced by winds and waves at the ocean surface[17] from a noise field that may include interfering sources from ships[18].

1.2 Objectives of this dissertation

The objectives of this dissertation are threefold:

1. The noise cross-correlation depends on the noise field as well as the propagation environment. Therefore, in order to accurately extract environmental information from ambient noise, the spatial and spectral characteristics of the ambient noise field must be known. To this effect, measurements of the acoustic signal and microseism signal generated by two oceanic tropical storms were made. Comparison of the *in situ* acoustic and distant seismic measurements of the two storms is used to infer the mechanism by which storm generated waves interact with coastlines to generate microseisms.

2. It has been established that a drifting vertical array can extract the depth of the seabed and sub-bottom reflecting layers[13, 14]. It is also well established that the adaptive array processing technique of Minimum Variance Distortionless Response (MVDR) beamforming can improve the directional sensitivity of a sensor array.[10] This dissertation seeks to explicitly describe the theoretical response of an MVDR passive fathometer both to a 1D noise model and a 3D oceanic noise model including an infinite sheet of surface noise, discrete interferers and sensor noise, such as the noise model presented by Ref. [20]

3. A model is developed to explicitly describe the passive fathometer correlation

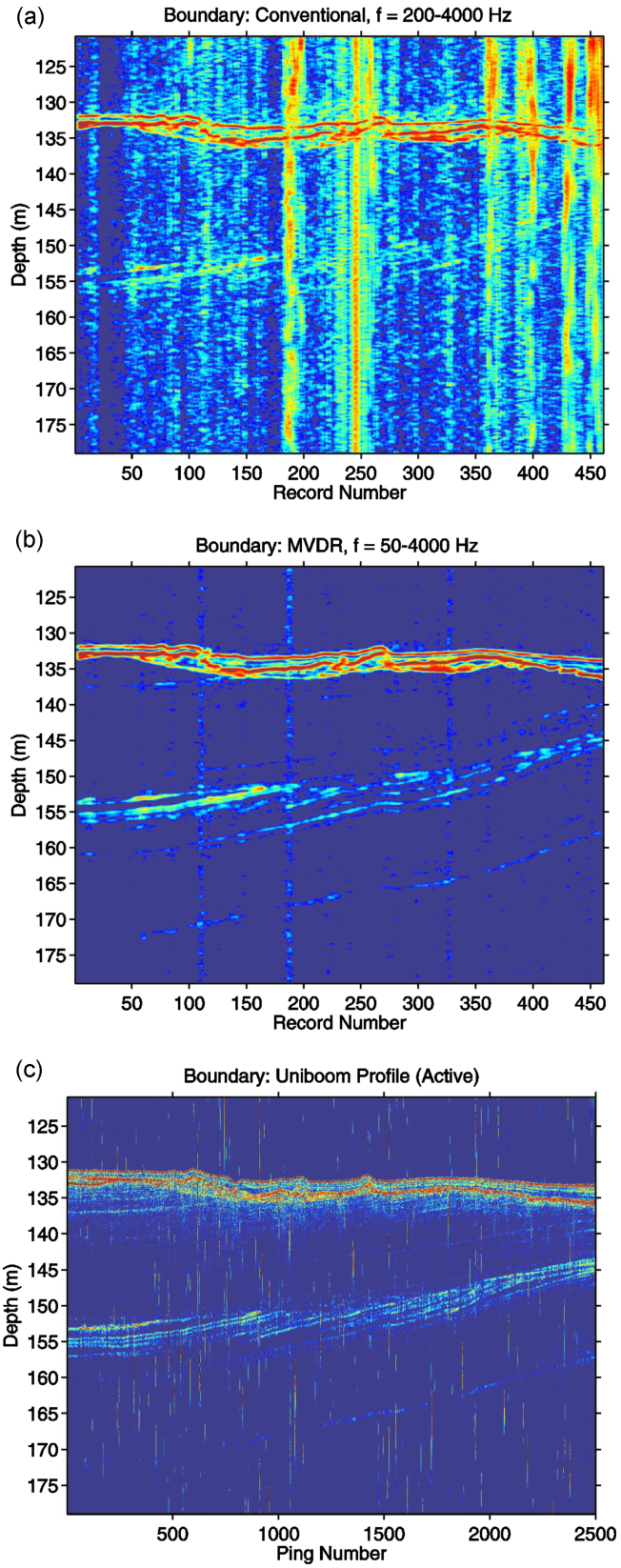

Figure 1.3: The passive fathometer response obtained with (a) plane-wave and (b) adaptive beamforming. (c) An active source map of the same transect. Ref. [18]

peak SNR as a function of environmental properties, averaging time and bandwidth. Experimental data are used to investigate the correlation peak SNR as a function of averaging time and averaging times of less than a second are used to track the motion of the array which oscillates with the surface wave motion.

The first two objectives allow for more robust interpretations of ambient noise correlations. The third objective, by providing a model for the correlation peak height as a function of environmental and measurement parameters, paves the way for extraction of seabed properties from the passive fathometer response. It has been shown that the wave properties seabed are related to it's mechanical properties and measurement of the reflection coefficient would yield estimates of the seabed layer density, porosity, compression and shear wave velocities and attenuations[21]. Therefore a robust model of the passive fathometer correlation peak height might allow inference of all of these properties from ambient noise measurements.

1.3 Basic Concepts

1.3.1 Ambient noise processing

Given a random noise signal, $S(t)$ and a reflected signal $R(t) = rS(t - \xi/c)$ where r is the reflection coefficient ξ is the two-way-travel distance and c is the average medium wave-speed, the signal recorded by a sensor at the origin is

$$x_0 = S(t) + R(t) \ . \tag{1.1}$$

Autocorrelating this signal gives

$$\begin{aligned} C_{00}(\tau) &= \int_{-\infty}^{\infty} x_0(t)x_0(t+\tau)\,d\,t \\ &= \int_{-\infty}^{\infty} S(t)S(t+\tau) + S(t)R(t+\tau) + R(t)S(t+\tau) + R(t)R(t+\tau)\,d\,t \\ &= (1+r^2)\delta(\tau) + r\delta(\tau \pm \xi/c) \ , \end{aligned} \tag{1.2}$$

where we have used the property of a random time series integrated over infinite time $\int S(t)S(t+\tau)\,dt = \delta(\tau)$. This yields a peak at zero-correlation time

and two more at positive and negative values of the two-way-travel-time ξ/c. In practice, infinite averaging time is not possible and these peaks will be embedded in a background random noise. Using an array of m sensors allows m^2 pairwise cross-correlations which yield similar results with slight shifts of the central and reflection peaks. Delay-and-sum techniques can then be used to increase the height of the reflection peak relative to the central peak and the background noise in the correlation.

It is convenient to do this processing in the frequency domain as time delays of Δ can be implemented by multiplying the frequency domain correlation by exponential terms $e^{\imath\omega\Delta}$. In the frequency domain Eq. (1.2) becomes

$$\begin{aligned} C_{00}(\omega) &= \mathrm{E}\left\{x_0(\omega)x_0(\omega)^*\right\} \\ &= |S(\omega)|^2\left[(1+r^2)+re^{\pm\imath\omega\xi/c}\right] . \end{aligned} \tag{1.3}$$

Given a 3D noise field $s(\theta,\phi,\omega)$ where θ and ϕ indicate polar and azimuthal angles and it is assumed that the noise field is white and spatially uncorrelated such that $\mathrm{E}\{s(\theta,\phi)s(\theta',\phi')\} = |S|^2\delta(\theta-\theta',\phi-\phi')/(4\pi)$. Given two sensors $x_{1,2}$ separated by d along the $\theta = 0$ axis, in free space, the frequency domain cross-correlation is

$$\mathrm{E}\{x_1(\omega)x_2(\omega)^*\} = \int_{\theta=0}^{\pi}\int_{\phi=-\pi}^{\pi} s(\theta,\phi)^2 e^{-\imath kd\cos\theta}\sin\theta\, d\theta d\phi . \tag{1.4}$$

Due to the azimuthal symmetry of the system the substitution $S(\theta) = \int s(\theta,\phi)\,d\phi$ can be made without loss of generality. Eq. (1.4) then becomes

$$\begin{aligned} \mathrm{E}\{x_1(\omega)x_2(\omega)^*\} &= \int_{\theta=0}^{\pi}\frac{-S^2}{\imath kd}\frac{d}{d\theta}\left(e^{-\imath kd\cos\theta}\right)d\theta \\ &= \frac{-S^2}{\imath kd}e^{-\imath kd\cos\theta}\Big|_{\theta=0}^{\pi} + \int_{\theta=0}^{\pi}\frac{2SS'}{\imath kd}e^{-\imath kd\cos\theta}d\theta \qquad (1.5) \\ &\approx \frac{1}{\imath kd}\left[e^{-\imath kd}S(0)^2 - e^{\imath kd}S(\pi)^2\right] , \qquad (1.6) \end{aligned}$$

where the integral $\int SS'e^{-\imath kd\cos\theta}\,d\theta$ is assumed small. Explicit evaluation of this term with the stationary phase approximation, which utilizes the property that an integral over an oscillatory term tends to zero except where the frequency is zero,

shows that as $kd \to \infty$ this integral is asymptotically dominated by peaks at $\theta = 0$ and $\theta = \pi$.

The factor of $1/k$ outside the bracket is equivalent to c/ω and hence in the time domain this is equivalent to the application of an integration in time over the time domain form of the expression inside the brackets (δ-functions located at $t = \pm kd/c$). Therefore in this three-dimensional case the differential of the cross-correlation with respect to time yields δ-functions located at $t = \pm kd/c$.

Introducing a reflecting boundary a distance ξ from the sensor pair along the $\theta = 0$ axis introduces a reflected field $R(\theta, \omega) = r_\theta S(\psi, \omega) e^{\imath\omega\xi_\theta/c}$ where r_θ is an angle dependent reflection coefficient (assumed to be zero for $\psi > \pi/2$) and ξ_θ is an angle dependent two-way-travel-distance. The mapping of ψ to θ is assumed arbitrary except $\psi = 0 \to \theta = \pi$ Thus the cross-term of the correlation is

$$\begin{aligned}
\mathrm{E}\{S_1(\omega)R_2(\omega)^*\} &= \int_{\theta=0}^{\pi} \frac{-r_\theta S(\theta)S(\psi)e^{\imath k\xi_\theta}}{\imath kd} \frac{d}{d\theta}\left(e^{-\imath kd\cos\theta}\right) d\theta \\
&= \frac{-r_\theta S^2 e^{\imath k\xi_\theta}}{\imath kd} e^{-\imath kd\cos\theta}\Big|_{\theta=0}^{\pi} - \int_{\theta=0}^{\pi} \frac{d}{d\theta}\left[S(\theta)S(\psi)e^{\imath k\xi_\theta}\right] \frac{e^{-\imath kd\cos\theta} d\theta}{\imath kd} \\
&\approx \frac{r_0 S(0)^2 e^{-\imath k(d+\xi_0)}}{\imath kd} \ , \qquad (1.7)
\end{aligned}$$

which yields a δ-function at a correlation time of $\tau = (\xi_0 + d)/c$, i.e. the two-way-travel-time from the midpoint between 1 and 2 to the reflecting boundary.

The asymptotic form of the noise cross-correlation [Eq. (1.7)] assumes that $S(\theta)S(\psi)e^{\imath k\xi_\theta}$ is continuous such that its θ-derivative is small. However, if the noise field $S(\theta)$ contains a discontinuity due to the presence of a discrete noise source such as a ship the noise field becomes

$$S(\theta) = S_c(\theta) + A_k\delta(\theta_k) \ , \qquad (1.8)$$

where $S_c(\theta)$ is a continuously varying field and $A_k >> \max_\theta S(\theta)$. Substituting Eq. (1.8) into Eq. (1.7) gives

$$\mathrm{E}\{S_1(\omega)R_2(\omega)^*\} \approx \frac{r_0 S(0)^2 e^{-\imath k(d+\xi_0)}}{\imath kd} + r_{\theta_k} A_k e^{\imath k(\xi_{\theta_k} - d\cos\theta)} \ , \qquad (1.9)$$

which includes both the seabed reflection peak and a larger spurious peak located at correlation time $(\xi_{\theta_k} - d\cos\theta)/c$.

1.3.2 Microseisms

Microseisms are mainly seismic signals generated by ocean waves[22, 23]. Although they are small in amplitude compared to many earthquakes they are ubiquitous in seismic measurements[24]. The peak of the microseism occurs near twice that of the ocean surface wave spectrum and these double frequency (DF) microseisms are generated by opposing wave fields[22] of the same wavenumber. These opposing wave fields generate a standing wave that does not decay in amplitude with depth. Propagating surface gravity waves decay exponentially with depth and therefore have very little interaction with the seabed except in shallow water. Double frequency waves can interact with the seabed at arbitrary depth and transfer ocean surface wave energy into the Earth's crust even in the deep ocean. Beamforming with seismic arrays shows that primary microseisms (those at the frequency of the surface gravity waves) are produced only when waves approach the shore while DF microseisms are detected throughout the ocean[25] and increase with the presence of winds[26] and storms[12].

Microseisms propagate onto land and are detected at seismic stations thousands of kilometers form the ocean. Thus microseisms form an ideal candidate for an ambient noise for seismic mapping. Using a network of seismic stations across California, microseisms generated by interaction of ocean waves with the California coast were measured and, after removing earthquakes from the data, the noise was cross-correlated across all sensor pairs to estimate the average surface wave speed along the transect defined by each sensor pair. A tomographic inversion was then used to generate a map of surface wave group-speeds. Comparison of the map made with one month of microseism data with a similar map formed with several years of accumulated earthquake data showed a good agreement[27].

1.3.3 Ocean noise

The predominant source of ambient noise in the ocean is often the ocean surface[28] which, through the action of of wind and waves, entrains bubbles. In large numbers these bubbles generate patches of white noise. The amount of noise produced by the surface is strongly dependent on the surface conditions[29, 30].

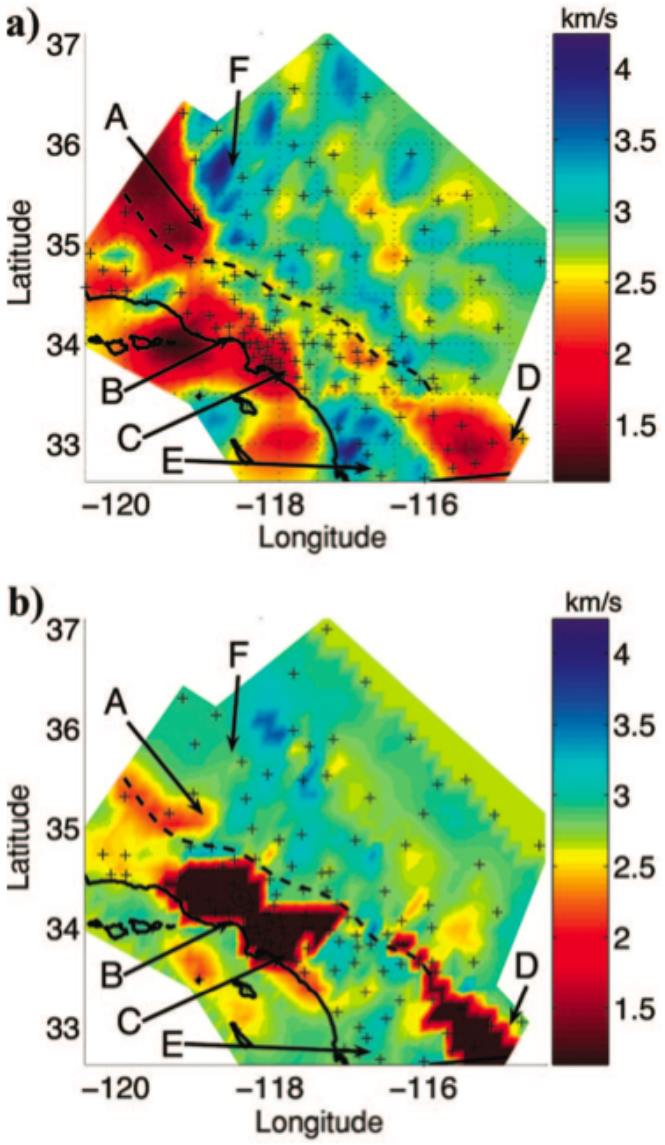

Figure 1.4: Maps of seismic surface wave velocities computed with (a) one month of ambient noise and (b) several years of earthquake data. Ref. [27]

The ocean also contains many biological noise sources and at times large numbers of snapping shrimp[31] form a volume source. Ships produce high amplitude noise and act as point sources.

Green's functions have been extracted from ocean surface noise, shipping noise, volume sources[3] and storm generated noise[32]. In the case of the passive fathometer[13, 14, 15, 16, 17, 18, 19] a drifting vertical array has been used to measure the Green's function of the seabed reflection from surface noise measurements.

1.3.4 Adaptive array processing

Given an array of m-sensors, subject to a plane wave signal $s(\theta)$ incident on the array at an angle of θ_s, the jth element records

$$x_j(\omega) = s(\omega)e^{\imath\omega\Delta_j(\theta_s)} + n_j \ , \tag{1.10}$$

where $\Delta_j(\theta_s)$ is the time-delay associated with plane wave propagation from the reference sensor to the $j$the sensor and n_j is random noise.

The array response is

$$\begin{aligned} X(\omega) &= \sum_{j=1}^{m} a_j x_j(\omega) e^{\imath\omega b_j} \\ &= \mathbf{a}^H \mathbf{x} \end{aligned} \tag{1.11}$$

where the signal recorded by the jth sensor is scaled by a_j and time delayed by b_j and the resulting signals are summed.

In the case of MVDR beamforming the steering vector $\mathbf{a}$ is selected such that the total power of the array response $\mathbf{a}^H \mathrm{E}\left\{\mathbf{x}\mathbf{x}^H\right\}\mathbf{a}$ is minimized while $\mathbf{a}$ is subject to the constraint that the signal of interest is not distorted. This implies

$$\begin{aligned} \mathrm{E}\left\{\mathbf{a}^H\mathbf{x}\right\} &= s \\ \mathbf{a}^H\mathbf{w} &= 1 \end{aligned} \tag{1.12}$$

where $w_j = e^{\imath\omega\Delta_j(\theta)}$ defines the plane wave steer vector [Eq. (1.10)].

The minimization is obtained by varying the $2m$ parameters of $\mathbf{a}$, subject to Eq. (1.12),

$$\begin{aligned} \min_{\mathbf{a}} \left[\mathbf{a}^H \mathrm{E}\left\{\mathbf{x}\mathbf{x}^H\right\}\mathbf{a}\right] &= \min_{\mathbf{a}} \left[\mathbf{a}^H \mathrm{E}\left\{|s|^2\mathbf{w}\mathbf{w}^H + \mathbf{n}\mathbf{n}^H\right\}\mathbf{a}\right] \\ &= |s|^2 + \min_{\mathbf{a}} \left[\mathbf{a}^H \mathrm{E}\left\{\mathbf{n}\mathbf{n}^H\right\}\mathbf{a}\right] \ . \end{aligned} \tag{1.13}$$

Thus it can be seen that the MVDR steer vector $\mathbf{a}$ minimizes the component from noise $\mathbf{a}^H \mathrm{E}\left\{\mathbf{n}\mathbf{n}^H\right\}\mathbf{a}$ while leaving the signal undistorted.

Using a Lagrange multiplier to obtain the constrained minimization the explicit form of $\mathbf{a}$ is[10]

$$\mathbf{a} = \frac{\mathbf{C}^{-1}\mathbf{w}}{\mathbf{w}^H\mathbf{C}^{-1}\mathbf{w}} \tag{1.14}$$

where $\mathbf{C} = \mathrm{E}\left\{\mathbf{x}\mathbf{x}^H\right\}$ is the data cross-spectral density matrix.

1.4 Experiments

This dissertation contains data from two acoustic experiments.

1.4.1 Boundary 2003 and 2004

The Boundary experiments were conducted off the coast of Sicily in 100–120 m of water. Several experiments on ambient noise and active source experiments were performed over several days but both the 2003 and 2004 experiments included deployment of a drifting 32-element vertical array with 0.18 m element-spacing conducted in the absence of any active source experiments.

The 23 July 2003 drift was conducted in extremely calm conditions and recorded 14 hr of data. Applying the passive fathometer algorithm with MVDR steering vectors to this data set yielded a sub-bottom profile that showed good agreement with active source measurements of the the same transect. The 12 May 2004 drift was performed about 12 hr after gale force winds (sustained winds of 25 m/s for 2 hr) were measured and was conducted in large swell.

1.4.2 Shallow Water 2006 (SW06)

The shallow water 2006 (SW06) experiment[33] was a multidisciplinary experiment conducted off the coast of New Jersey from mid-July to mid-September of 2006 in 80 m water depth. Many hydrophone arrays and surface buoys were deployed for a period of several weeks. Many active source experiments were conducted over this time but these could often be removed from the recorded data sets allowing for extensive processing of ambient noise. During the experiment two tropical storms, Ernesto and Florence, passed near the experiment site generating large wave conditions. These periods provided excellent data for ambient noise experiments due to the large surface noise.

1.5 Scope of the disertation

Chapter 2 investigates the nature of ambient noise in the Earth's oceans and crust generated by tropical storms over the ocean. The acoustic signature recorded by bottom-mounted hydrophones on the SW06 site as two tropical storms passed overhead show the presence of wave generated signals at 70 m water depth. The spectral signature of these recordings are compared with land-based microseism measurements. Despite differences in size the two storms produced similar microseism energy suggesting that the transmission of surface wave energy to seismic energy is complex and proximity of the storm to the coast may play a role.

Chapter 3 considers the application of MVDR steering vectors to a 1D model of the passive fathometer. The fathometer response is derived with an eigenvalue decomposition which shows that the MVDR passive fathometer response consists of the same features as that obtained with plane-wave beamforming but the reflection signal is preferentially weighted relative to noise and is multiplied by a negative factor. This negative factor is consistent with simulations and experimental data.

Chapter 4 expands the passive fathometer model of chapter 3 to include a 3D model of oceanic noise including an infinite sheet of surface noise and discrete interference sources. The fathometer response to the 2D sheet of noise sources

is evaluated explicitly with the stationary phase approximation to give the first-order response. The effect of plane-wave and MVDR beamforming on the model CSDM are shown theoretically and through numerical simulations. It is shown theoretically that array processing, and MVDR processing in particular, improve the seabed Green's function extraction.

Chapter 5 considers theoretically the height and SNR of the passive fathometer response as a function of environmental parameters, averaging time and bandwidth. Using data from the Boundary experiments the passive fathometer response is obtained with less than a second of averaging time and this allowed surface-wave driven motion of the array during the high wave conditions of the 2004 experiment to be observed. It is demonstrated that this array motion attenuates the hight and SNR of the reflection peak when averaged over more than one tenth of the surface-wave period. A peak tracker and realignment algorithm is used on the passive fathometer response and the realigned data is averaged over several wave cycles to yield a better results.

Bibliography

[1] J. Rickett and J. Claerbout, "Acoustic daylight imaging via spectral factorization: Helioseismology and reservoir monitoring," The Leading Edge **18**, 957–960 (1999).

[2] R. L. Weaver and O. I. Lobkis "Ultrasonics without a source: Thermal fluctuation correlations at MHz frequencies," Phys. Rev. Lett. **87**, 134301 (2001).

[3] P. Roux and W. A. Kuperman "Extracting coherent wave fronts from acoustic ambient noise in the ocean," J. Acoust. Soc. Am. **116**, 1995–2005 (2004).

[4] K. G. Sabra, P. Gerstoft, P. Roux, W. A. Kuperman and M. C. Fehler "Surface wave tomography from microseisms in Southern California," Geophys. Res Lett. **32**, L14311 (2005).

[5] O. I. Lobkis and R. L. Weaver "On the emergence of the Greens function in the correlations of a diffuse field," J. Acoust. Soc. Am. **110**, 3011–3017 (2001).

[6] P. Roux, K. G. Sabra, W. A. Kuperman and A. Roux "Ambient noise cross-correlation in free space: Theoretical approach," J. Acoust. Soc. Am. **117**, 79–84 (2005).

[7] J. A. Grant and R. Schrieber, "Modern swathe sounding and sub-bottom profiling technology for research applications: The Atlas Hydrosweep and Parasound Systems", Marine Geophys. Res., **12**, 9–19, 1990

[8] H. Nakahara, "A systematic study of theoretical relations between spatial correlation and Green's function in one-, two- and three-dimensional random scalar wavefields," Geophys. J. Int. **167**, 1097–1105 (2006).

[9] K. G. Sabra, P. Roux and W. A. Kuperman "Emergence rate of the time-domain Green's function from the ambient noise cross-correlation function," J. Acoust. Soc. Am. **118**, 3524-3531 (2005).

[10] Van Trees, H. L., *Optimum array processing* (Wiley, New York, 2002).

[11] P. Gerstoft, M. C. Fehler and K. G. Sabra, "When Katrina hit California", Geophys. Res. Lett., **33**, L17308, (2006).

[12] P. Gerstoft, P. M. Shearer, N. Harmon and J. Zhang, "Global P, PP, and PKP wave microseisms observed from distant storms", Geophys. Res. Lett., **35**, L23306, (2008).

[13] M. Siderius, C. H. Harrison and M. B. Porter, "A passive fathometer technique for imaging seabed layering using ambient noise," J. Acoust. Soc. Am. **120**, 1315–1323 (2006).

[14] P. Gerstoft, W. S. Hodgkiss, M. Siderius, C. F. Huang, and C. H. Harrison "Passive fathometer processing," J. Acoust. Soc. Am. **123**, 1297–1305 (2008).

[15] C. H. Harrison "Anomalous signed passive fathometer impulse response when using adaptive beam forming," J. Acoust. Soc. Am. **125**, 3511–3513 (2009).

[16] J. Traer, P. Gerstoft, H. C. Song and W. S. Hodgkiss "On the sign of the adaptive passive fathometer impulse response," J. Acoust. Soc. Am. **126**, 1657–1658 (2009).

[17] S. L. Means and M. Siderius "Effects of sea-surface conditions on passive fathometry and bottom characterization," J. Acoust. Soc. Am. **127**, 2193–2200 (2010).

[18] M. Siderius, H. C. Song, P. Gerstoft, W. S. Hodgkiss and C. H. Harrison "Adaptive passive fathometer processing," J. Acoust. Soc. Am. **127**, 2193–2200 (2010).

[19] J. Traer, P. Gerstoft and W. S. Hodgkiss, "Ocean bottom profiling with ambient noise: A model for the passive fathometer ", J. Acoust. Soc. Am., **129**, 1825–1836, (2011).

[20] W. A. Kuperman and F. Ingenito "Spatial correlation of surface generated noise in a stratified ocean," J. Acoust. Soc. Am. **67**, 1988–1996 (1980).

[21] M. J. Buckingham, "Theory of acoustic attenuation, dispersion, and pulse propagation in unconsolidated granular materials including marine sediments ", J. Acoust. Soc. Am., **102**, 2579–2596 (1997).

[22] M. S. Longuet-Higgins, "A theory of the origin of microseisms," Philos. Trans. R. Soc. London 1–35 (1950).

[23] P. D. Bromirski and F. K. Duennebier, "The near-coastal microseism spectrum: Spatial and temporal wave climate relationships, J. Geophys. Res., **107**, 2166 (2002).

[24] K. Hasselmann, "A statistical analysis of the generation of microseisms," Rev. Geophys. **1**, 177–210 (1963).

[25] R. K. Cessaro, "Sources of primary and secondary microseisms", Bull. Seism. Soc. Am., **84**, 142–148 (1994).

[26] J. Zhang, P. Gerstoft and P. M. Shearer "High-frequency P-wave seismic noise driven by ocean winds," Geophys. Res. Lett. **36**, L09302 (2009).

[27] P. Gerstoft, K. G. Sabra, P. Roux, W. A. Kuperman and M. C. Fehler "Green's functions extraction and surface-wave tomography from microseisms in southern California," Geophys. **71**, SI23SI31 (2006).

[28] B. F. Cron and C. H. Sherman, "Spatial Correlation Functions for Various Noise Models ," J. Acoust. Soc. Am., **34**, 1732–1736, (1962).

[29] W. A. Kuperman and M. C. Ferla, "A shallow water experiment to determine the source spectrum level of wind generated noise", J. Acoust. Soc. Am., **77**, 2067–2073, (1985)

[30] C. S. McCreery, F. K. Dunnebier and G. H. Sutton "Correlation of deep ocean noise (0.4–30 Hz) with wind, and the Holu spectrum- A worldwide constant," J. Acoust. Soc. Am. **93**, 2639–2648 (1993).

[31] C. L. Epifanio, J. R. Potter, G. B. Deane, M. L. Readhead, and M. J. Buckingham, "Imaging in the ocean with ambient noise: the ORB experiments", J. Acoust. Soc. Am., **106**, 3211–3225, (1999)

[32] L. A. Brooks and P. Gerstoft "Green's function approximation from cross-correlations of 20–100 Hz noise during a tropical storm," J. Acoust. Soc. Am. **125**, 723–734 (2009).

[33] D. Tang, J. N. Moum, J. F. Lynch, P. Abbot, R. Chapman, P. H. Dahl, T. F. Duda, G. G. Gawarkiewicz, S. M. Glenn, J. A. Goff, H. C. Graber, J. N. Kemp, A. R. Maffei, J. D. Nash, A. E. Newhall, "Shallow Water 06 : a joint acoustic propagation/nonlinear internal wave physics experiment," Oceanography **20**, 156–167, (2007).

Chapter 2

Shallow-water seismoacoustic noise generated by tropical storms Ernesto and Florence

Land-based seismic observations of double-frequency (DF) microseisms generated during Tropical Storms Ernesto and Florence are dominated by signals in the 0.15–0.5Hz band. In contrast, data from seafloor hydrophones in shallow water (70m depth, 130 km off the New Jersey coast) show dominant signals in the gravity-wave frequency band, 0.02–0.18Hz and low amplitudes from 0.18–0.3Hz, suggesting significant opposing wave components necessary for DF microseism generation were negligible at the site. Florence produced large waves over deep water while Ernesto only generated waves in coastal regions, yet both storms produced similar spectra. This suggests near-coastal shallow water as the dominant region for observed microseism generation.

2.1 Introduction

Microseisms are ubiquitous seismic signals generated by ocean waves[1]. The peak of the microseism spectrum occurs near twice that of ocean surface waves [double frequency (DF) microseisms], generated by the interaction of opposing surface waves of nearly the same wavenumber [2]. Unlike traveling ocean waves

which decay exponentially with depth, the amplitude of the DF pressure pulse does not decay appreciably with depth [2]. Primary microseisms are observed at ocean wave frequencies and are generated only in shallow water by breaking waves or interaction with the sloping bottom [3]. The results from beamforming with seismic arrays suggests that the dominant source regions for primary and double frequency signals may differ in space and/or time[4].

Recent work suggests that microseisms are only generated when surface waves approach coastal areas[5, 6, 7, 8] and that the generation of microseisms is well-correlated with ocean surface conditions[5],[9]. Storms over the ocean generate large waves causing elevated microseism levels that have been attributed to specific storm events[4],[10].

The surface gravity-wave induced pressure at the seafloor is[5],

$$p = \frac{p_0}{\cosh kH}, \tag{2.1}$$

where p_0 is the pressure at the surface, H ocean depth and k wavenumber, determined by the surface gravity wave dispersion, $\omega^2 = gk \tanh kH$ where ω is the angular frequency, $\omega = 2\pi f$, with f the surface wave frequency. For example, with $H = 70\,m$ (as in the experiment discussed), the pressure from a 0.1 Hz wave will be $p = 0.1p_0$ and the pressure from a 0.3 Hz wave will be $p = 10^{-11}p_0$. This indicates that the decay of wave pressure with depth is strongly dependent on the wave frequency, and that the pressure spectrum from overhead wave activity observed at the bottom in a shallow water environment will be dominated by direct forcing from low frequencies. DF pressure fluctuations will become dominant in deep water because they do not decay appreciably with depth regardless of their frequency.

An opportunity to study storm generated microseisms on both the ocean bottom and land occurred when waves generated by Tropical Storms Ernesto and Florence passed over the SW06 site during September 2006. Seafloor hydrophones from the SWAMI32, SWAMI52 and SHARK arrays measured pressure variations at the ocean bottom on the shallow-water continental shelf. These were compared with broadband seismic data from the HRV (Harvard) station in Massachusetts.

2.2 Array environment

The edge of the leading right-hand quadrant of Tropical Storm Ernesto passed over the arrays on September 2 while the inland storm center moved northward [Fig. 2.1(a)]. The storm, recorded by University of Miami Air-Sea Interaction Spar (ASIS) Buoys [11] generated steady high winds and wave energy [see Fig.2.1 (c)–(e)] over the arrays for two days. The wind speed suddenly dropped and changed direction near the end of September 2 as the storm passed the arrays [Fig. 2.1(c)–(d)]. Throughout September 1–2 the winds blew from the east with speeds from 10–20 m/s. From 20 Zulu (20 Z) September 2 through September 3 the winds blew from the west at speeds from 2–10 m/s. Wave energy remained strong for a further 28 hours after the wind dropped [Fig.2.1 (e)]. The waves underwent a change in direction over September 2 (not shown), transitioning from eastward to south-west incidence, potentially producing an opposing wave-field for standing wave generation and transmission of microseisms to the seabed [2]. NOAA hindcasts[12] showed Ernesto produced large waves in shallow water such as the SW06 site, but not in deep waters [Fig. 2.1(f)]. The large waves in Fig. 2.1(f) at (42°N, 55°W) were from another storm. Wave data from the ASIS buoy was consistent with the hindcast results at the site.

On September 10, large waves from Tropical Storm Florence arrived at the site. Florence moved northward through the Atlantic Ocean with the storm center remaining in deep water [Fig. 2.1(a) and (g)]. The ASIS buoys and both SWAMI arrays were removed prior to the arrival of Florence and no wind or wave data were available. The SHARK array recorded acoustic data through September 14. The SWAMI and SHARK arrays were situated on a sandy floor at a depth of 70–80 m, 20 km west of the continental shelf and 130 km from the New Jersey coast [Fig. 2.1(b)].

Although the hydrophones were not designed to work at frequencies less then 2 Hz, the relative spectrogram levels (Fig. 2.2) were corrected using the SWAMI hydrophone frequency response and the characteristics of the electronic filters. From 10–15 Z, September 2, the SWAMI32 hydrophones recorded broadband clicks likely attributed to motion of the array. This distortion was minimized

by excising any segments with an amplitude greater than four standard deviations of the signal within each 6:24 min file. For the SHARK array any segment with an amplitude greater than eight standard deviations was excised. The frequency response of the SHARK hydrophones is unknown. The SHARK frequency response was estimated by comparing the spectra obtained by the SHARK and SWAMI52 arrays over the period of time when the two arrays overlapped (18 Z August 25 to 17 Z September 6) and assuming the two arrays are measuring the same signal.

2.3 Acoustic spectrograms

At frequencies above 30 Hz, the acoustic levels are well correlated with the local wind speed, while below 2 Hz a significant signal is observed for two days after the passing of the storm [Fig. 2.2(a)–(d)]. This suggests the signals observed above 30 Hz are generated by wind-induced breaking waves, in agreement with others [13], and signals below 2 Hz are generated by surface waves. Wave-wave interactions can produce signals as high as 7 Hz [14], and may be the source of the large signals on September 2 from 2–5 Hz.

The signals recorded by the two arrays are similar at frequencies below 2 Hz, suggesting that either these signals travel over the 23 km distance separating the arrays, or that the surface wave spectra are similar over many kilometers. The dominant signal occurred at 0.02–0.18 Hz [Fig. 2.2(e)–(f)] throughout the five-day period, corresponding to the surface wave frequency band [Fig. 2.1(e)]. This 0.02–0.18 Hz signal is at a maximum when the storm is above the array. Seismic arrays in California detected a strong 0.07–0.11 Hz signal at this time, originating along an azimuth consistent with the signal being generated in coastal waters between 38–40° N [4]. This region includes the SWAMI and SHARK arrays. The peak in seismic signal at this time is not correlated with an increase in wave amplitudes, suggesting that microseism generation may be dependent on the location of the waves. Near these times, NOAA hindcasts show large waves impacting the Coast of Cape Cod [12], which has previously been identified as a site of strong microseism generation[10].

Relatively low spectral levels were observed in the 0.14–0.18 Hz band during times when the peak in wave energy near 0.08 Hz occurred. The frequency range of the low energy band should include high amplitude DF microseism signals. The ASIS buoy measured the dominant wave direction as westward over September 1 and northward over September 2, towards the coasts of New Jersey and Cape Cod, respectively. Conceptually, opposing waves from coastal reflection interacting with incoming swells should produce standing waves, however, no DFs were observed at magnitudes equivalent to the primary pressure wave. The absence of DF signal associated with the dominant wave frequency indicates that little opposing wave energy was present. Note that DF microseisms on land and in the deep ocean typically have much higher amplitudes than primary microseisms[10, 14, 5]. DF levels at HRV are much higher than associated primaries during Ernesto, but the opposite is true at the seafloor arrays, indicating that the signal observed by the arrays is dominated by direct pressure from overhead waves, not from microseisms.

The 0.2–2 Hz signal is 20–30 dB weaker than the 0.02–0.18 Hz signal. It does not appear in the wave spectra, which suggests that this signal is likely either DF microseisms, or due to an inaccurate response of the wave buoy at higher frequencies. The signal maximum in this 0.2–2 Hz band occurs at 03 Z September 2 [Fig. 2.2(c)-(f)]. A second signal maxima is observed between 0.2–2 Hz at 18 Z September 2 and corresponds to a shift in local wind direction [Fig. 2.2(c)–(d)], suggesting that opposing seas forcing necessary for the DF mechanism occurred.

The SHARK array was used to compute spectrograms from August 25–September 14 [Fig. 2.3(b)]. As with the SWAMI measurements of Ernesto, during Florence the dominant signal occurred between 0.02–0.18 Hz, corresponding to the dominant wave frequency band, with little signal observed in the associated DF band. As Florence did not make landfall, it had a much larger fetch than Ernesto and produced lower frequency ocean waves for a longer time. The lack of DF signals during both tropical storms suggests that opposing wave components at swell frequencies are not generated by wave reflection/scattering at the coastline nearest the arrays and/or because these components are dissipated by bottom interaction when crossing the relatively wide shallow shelf.

2.4 Seismic spectrograms

In contrast to the spectrograms from the acoustic arrays, the land-based seismic spectra at HRV are dominated by DF signals between 0.15–0.5 Hz, which are 20 dB stronger than the primary signal [Fig. 2.3(c)]. The microseisms from Ernesto's waves are initially seen at 0.15 Hz on August 29 as Ernesto impacts Florida. The signals are present for 6 days as Ernesto travels northward, increasing in frequency as the storm center moves on land and the fetch of the storm decreases generating more short period wave energy near-shore. The 0.2–0.4 Hz signal present from August 29–30 is likely due to a smaller storm to the northeast [Fig. 2.1(f)]. During the period when Ernesto was over the arrays (September 2), the 0.02–0.18 Hz band that dominated the SWAMI array data was largely absent at HRV, confirming that the signals in that band at the arrays were dominated by direct pressure from overhead waves.

After Ernesto dissipated, another strong set of signals appear from September 12–14, attributed to waves generated by Tropical Storm Florence. The signal from Florence has higher amplitude than that of Ernesto and lower frequency, consistent with the larger waves and fetch of Florence [Fig. 2.1(f),(g)]. These waves impacted the coasts from Florida to Nova Scotia. As with the seismic signal from Ernesto, the DF signal at HRV from Florence is 20 dB stronger than the primary signal.

2.5 Discussion

The seismic signals of both storms recorded on land were dominated by the DF signals, which is consistent with previous studies and implies that both storms generate DF waves. However, the acoustic levels of Ernesto and Florence contained a weak signal in the lower part of the DF range (0.18–0.25 Hz). Rather they are dominated by signals at the same frequency as the ocean waves, consistent with a linear forcing mechanism. Despite both storms producing westward traveling waves, no evidence of a wave-wave interaction due to reflection of waves from the coast was observed. This suggests that low frequency opposing waves and

corresponding DF microseisms are negligible near the SW06 site, consistent with observations at HRV during the 1991 "Perfect Storm" [10] and that the DF signals detected by the HRV seismic station were generated elsewhere.

When Ernesto reached the SW06 site, the storm center was inland [Fig. 2.1(f)] and most of the storm generated waves were in shallow waters. Ernesto produced a significant DF signal at nearby seismic stations over a much longer period of time than the larger storm Florence, which produced larger waves over a greater area in the deep ocean [Fig. 2.1(g)]. Babcock *et al.*[9] et al. [1994] observed high amplitude DF microseisms with an ocean bottom array at a nearby deep water site, indicating that even smaller storms can generate appreciable DF energy and that waves from Florence and Ernesto were likely generating DF microseisms offshore in the open ocean. Despite these large disparities in the size of storms Florence and Ernesto [Fig. 2.1(f)–(g)] the associated microseism signals were similar [Fig. 2.3(c)] suggesting only near-shore waves produce the signals detected at the HRV seismic station.

The absence of DF signals at the SW06 site may be due to variations in local bathymetry. The SW06 site is separated from the nearest coast by 130 km of shallow water. Waves below 0.1 Hz interact with the bottom at this depth and may attenuate before reaching the coast. It may be be the case that the DF microseisms observed at the HRV seismic station are generated in waters shallower than the SW06 site (70 m). The continental shelf narrows substantially near Cape Hatteras to the south and Cape Cod to the north. These regions may be sites of high microseism generation as low frequency waves may attenuate less and hit the coast with more energy.

Acknowledgments

This chapter is a reprint of the material as it appears in the Journal of the Acoustical Society of America 2008. Traer, James; Gerstoft, Peter; Bromirski, Peter D.; Hodgekiss, William S.; Brooks, Laura A., Acoustical Society of America, 2008. The dissertation author was the primary investigator and author of this paper.

This project was funded by: the Office of Naval Research, the Department of Energy National Energy Technology Laboratory via the Gulf of Mexico Hydrates Research Consortium, University of Mississippi, and the California Department of Boating and Waterways (to P.D. Bromirski).

Data assistance are appreciated from Neil Williams and Hans Graber, University of Miami (local wind and wave data); Arthur Newhall, Woods Hole Oceanographic Institute (SHARK); and Applied Research Laboratories, University of Texas (SWAMI).

Bibliography

[1] S. C. Webb, "The Earth's 'hum' is driven by ocean waves over the continental shelves," Nature **445**, 754–756 (2006).

[2] M. S. Longuet-Higgins, "A theory of the origin of microseisms," Philos. Trans. R. Soc. London 1–35 (1950).

[3] K. Hasselmann, "A statistical analysis of the generation of microseisms," Rev. Geophys. **1**, 177–210 (1963).

[4] P. Gerstoft and T. Tanimoto, "A year of microseisms in southern California," Geophys. Res. Lett. **34**, L20304 (2007).

[5] P. D. Bromirski and F. K. Duennebier, "The near-coastal microseism spectrum: Spatial and temporal wave climate relationships," J. Geophys. Res. **107**, 2166 (2002).

[6] A. Friedrich, F. Krüger, and K. Klinge, "Ocean-generated microseismic noise located with the Gräfenberg array," J. Seismol. **2**, 47–64 (1998).

[7] T. Tanimoto, "Excitation of microseisms," Geophys. Res. Lett. **34**, L05308 (2007).

[8] P. Gerstoft, M. C. Fehler, and K. G. Sabra, "When Katrina hit California," Geophys. Res. Lett. **33** L17308 (2006).

[9] J. M. Babcock, B. A. Kirkendall, and J.A. Orcutt, "Relationships between ocean bottom noise and the environment," Bull. Seismol. Soc. Am. **84**, 1991–2007 (1994).

[10] P. D. Bromirski, "Vibrations from the Perfect Storm," Geochem. Geophys. Geosys. **2**, 000119 (2001).

[11] H. C. Graber, E. A. Terray, M. A. Donelan, W. M. Drennan, J. C. Van Leer, and D. B. Peters, "ASIS — a new air–sea interaction spar buoy: Design and performance at sea," J. Atmos. Ocean. Technol. **17**, 708–720 (2000).

[12] "NOAA wavewatch III",

URL `http://polar.ncep.noaa.gov/waves/nww3_hist.html`, National Oceanic and Atmospheric Administration, downloaded 20 March 2008.

[13] D. P. Knobles, S. Joshi, and R. D. Gaul, "Character of wind-driven ambient noise in a shallow water environment with a sandy seabed," J. Acoust. Soc. Am. (submitted) (2008).

[14] C. S. McCreery, F. K. Duennebier, and G. H. Sutton, "Correlation of deep ocean noise (0.4–30 Hz) with wind, and the Holu Spectrum - A worldwide constant," J. Acoust. Soc. Am. **93**, 2639–2648 (1993).

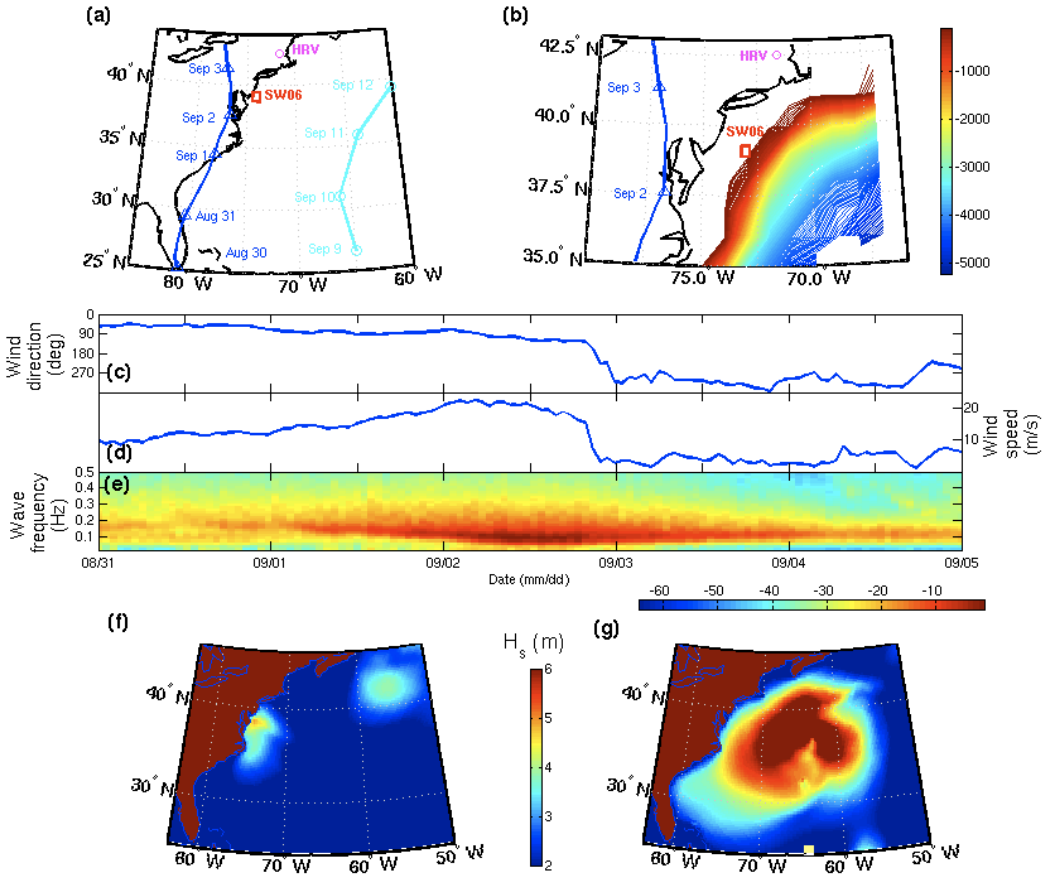

Figure 2.1: (Color online) The experiment environment. (a) Experiment location (rectangle) and the recorded path of the storm centers. Triangles mark the storm center for Ernesto and circles the center for Florence every 24 hours starting 0 Z Aug 30 and Sep 9, respectively. (b) Bathymetry contours from 100-5000 m depth. Water depth less than 100 m is white. (c) Wind direction. (d) Wind speed. (e) The surface wave spectra (dB) from 0.02–0.5 Hz for Aug 30–Sep 3. The wave spectral energy is normalized with respect to the highest observed signal. Wind and wave data from the ASIS buoys are averaged over half-hour periods. (f)–(g) Significant wave heights (Hs) from Ernesto (9 Z 2 Sep) and Florence (9 Z 12 Sep), respectively.

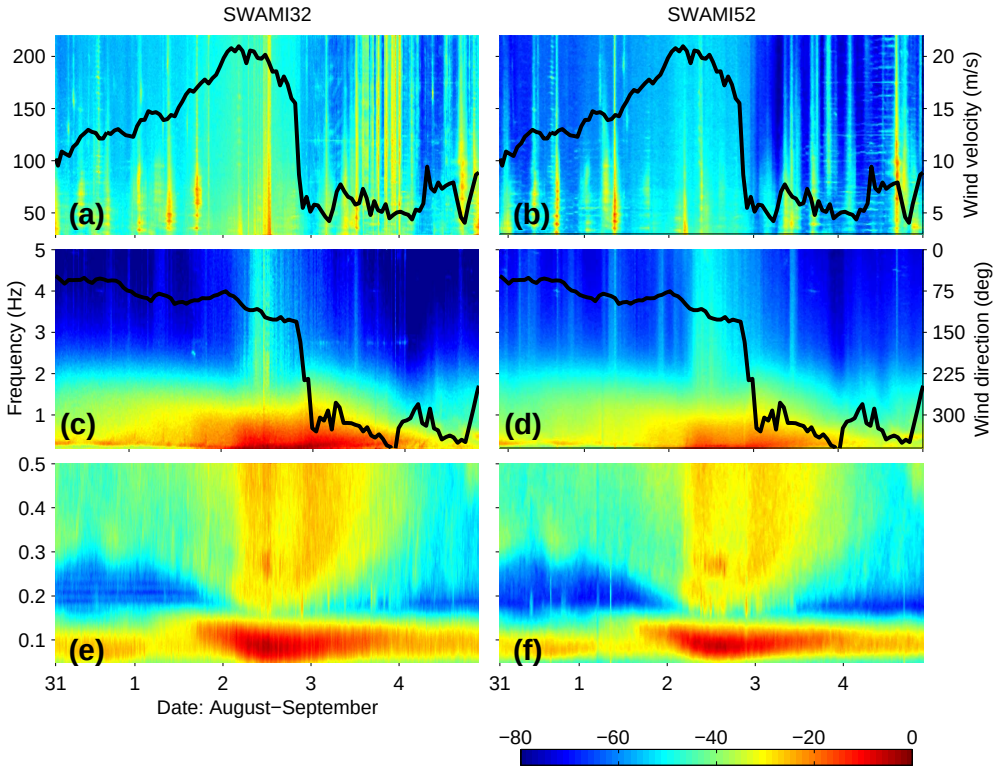

Figure 2.2: (Color online) Normalized spectrograms (dB) of the acoustic data at three frequency scales [(a)–(b) 30–220 Hz, (c)–(d) 0.2–5 Hz, and (e)–(f) 0.02–0.5 Hz] obtained over a five day period (Aug 31-Sep 4) from the SWAMI32 [(a), (c) and (e)] and SWAMI52 [(b), (d) and (f)] arrays. The wind velocity trace from Fig. 2.1(d) is superimposed in (a) and (b) and the wind direction from Fig. 2.1(c) is superimposed in (c) and (d). The spectrograms are averaged over five hydrophones and normalized with respect to the highest power spectral density in the observed range.

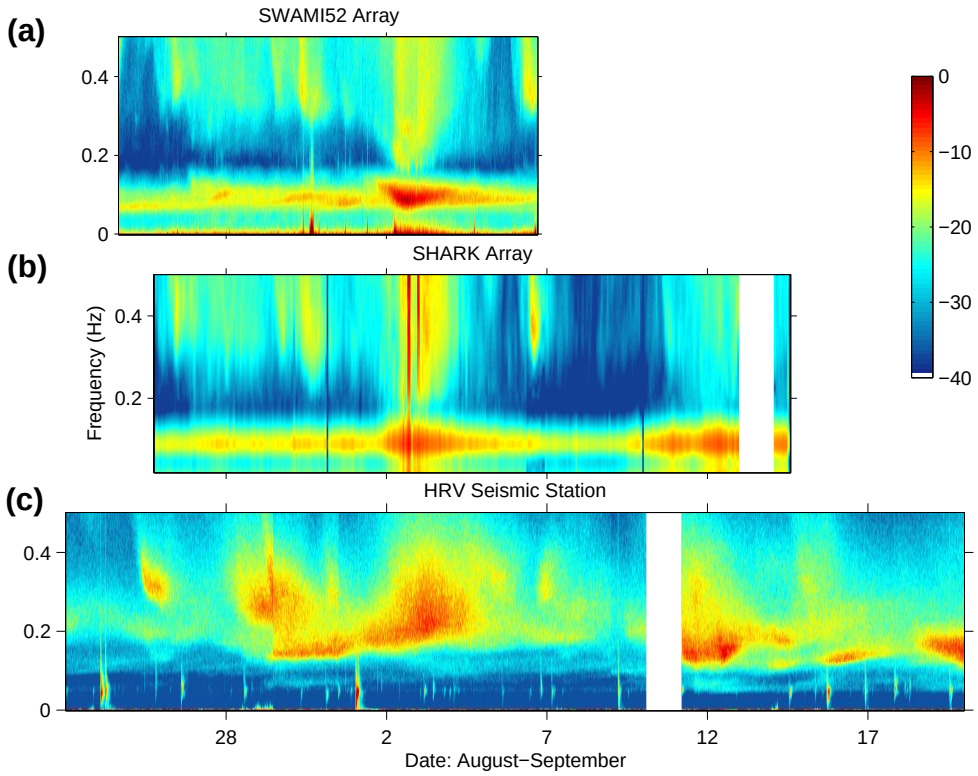

Figure 2.3: (Color online) Normalized spectrograms (dB) of the acoustic data between 0.01–0.5 Hz from the (a) SWAMI52 array, (b) SHARK array and (c) HRV seismic station. SWAMI52 data was available from Aug 24–Sep 6, SHARK data from Aug 25–Sep 19 and HRV data from Aug 23–Sep 20.

Chapter 3

On the sign of the adaptive passive fathometer impulse response

Harrison [J. Acoust. Soc. Am. **125**, 3511–3513 (2009)] presented a mathematical explanation for a sign-inversion induced to the passive fathometer response by minimum variance distortionless response (MVDR) beamforming. Here a concise mathematical formulation is offered, which decomposes the cross-spectral density matrix into coherent and incoherent components and allows the matrix inversion to be obtained exactly by eigendecomposition. This shows that, in the region containing the bottom reflection, the MVDR fathometer response is identical to that obtained with conventional processing multiplied by a negative factor.

3.1 Introduction

A drifting vertical array can be used as a passive fathometer by cross-correlating up- and down-ward beams [Siderius *et al.*, 2006]. A more detailed analysis and an introduction to the application of adaptive beamforming to the passive fathometer is given in Gerstoft *et al.* [2008]. Recently it was found that adaptive processing induced a sign change in the fathometer cross-correlation. An explanation was given in Harrison [2009] using the Woodbury matrix identity to

invert the cross-spectral density matrix (CSDM). Here we offer a simple explanation using eigendecomposition to perform this matrix inversion. This approach is exact given the idealized noise model described below.

A simple physical model is used consisting of a vertically downward propagating signal and its vertically upward propagating reflection in the presence of incoherent background noise. It should be noted that this is an idealization and a realistic ocean environment would likely contain a more complicated spatial structure. The passive fathometer requires the reflected signal to be coherent with the downward propagating signal to extract the depths of the reflecting layer boundaries. Consequently the two coherent signals are not separable and act as a single coherent component in constructing the CSDM. We show that, in the region of interest for the fathometer attributed to this coherent component, the adaptive response obtained using the minimum variance distortionless response (MVDR) beamformer is identical to that obtained using the conventional beamformer multiplied by a *negative* factor.

3.2 Theory

Consider the response of the fathometer to a single frequency plane wave. The conventional response is given by [Gerstoft *et al.*, 2008]

$$C(\omega) = \mathbf{w}^T \mathbf{R} \mathbf{w} \qquad , \tag{3.1}$$

where $\mathbf{w}$ is the downward directed steering vector, the superscript T denotes the matrix transpose and $\mathbf{R}$ is the CSDM. The MVDR adaptive response is given by [Harrison, 2009]

$$C_{\mathrm{MVDR}}(\omega) = \Lambda(\omega) \mathbf{w}^T \mathbf{R}^{-1} \mathbf{w} \qquad , \tag{3.2}$$

where $\Lambda = |\mathbf{w}^H \mathbf{R}^{-1} \mathbf{w}|^{-2}$ is a positive normalization factor and the superscript H denotes the complex conjugate transpose. Thus, excluding the normalization factor, MVDR processing is of the same functional form as conventional processing with the CSDM inverse in place of the CSDM.

Decomposing the CSDM into coherent and incoherent components,

$$\mathbf{R} = \mathbf{d}\mathbf{d}^H + \sigma^2\mathbf{I} \qquad , \tag{3.3}$$

where $\mathbf{d} = \mathbf{d}_{\text{down}} + \mathbf{d}_{\text{up}}$ is the sum of the downward propagating signal and the upward propagating reflection. $\mathbf{d}_{\text{down}}$ is proportional to the steering vector $\mathbf{w}$. $\sigma^2\mathbf{I}$ is the component due to incoherent background noise, with $\mathbf{I}$ designating the identity matrix. This allows the CSDM to be expanded by eigendecomposition to yield

$$\mathbf{R} = (\sigma^2 + a)\mathbf{u}_1\mathbf{u}_1^H + \sigma^2\sum_{j=2}^{N}\mathbf{u}_j\mathbf{u}_j^H \qquad , \tag{3.4}$$

where N is the number of array elements, a is the eigenvalue component corresponding to the coherent signal and $\mathbf{u}_j$ are the normalized eigenvectors. The CSDM inverse is

$$\begin{aligned}
\mathbf{R}^{-1} &= \frac{1}{(\sigma^2+a)}\mathbf{u}_1\mathbf{u}_1^H + \frac{1}{\sigma^2}\sum_{j=2}^{N}\mathbf{u}_j\mathbf{u}_j^H \\
&= \frac{1}{\sigma^2}\left[\frac{\sigma^2}{(\sigma^2+a)}\mathbf{u}_1\mathbf{u}_1^H + \mathbf{I} - \mathbf{u}_1\mathbf{u}_1^H\right] \\
&= \frac{1}{\sigma^2}\left[\mathbf{I} - \frac{a}{\sigma^2+a}\mathbf{u}_1\mathbf{u}_1^H\right] \\
&= -\frac{1}{(\sigma^2+a)^2}\mathbf{d}\mathbf{d}^H + \frac{1}{\sigma^2}\mathbf{I} \qquad ,
\end{aligned} \tag{3.5}$$

where we have utilized $\sum \mathbf{u}_j\mathbf{u}_j^H = \mathbf{I}$. Thus the CSDM inverse contains the same terms as the CSDM with different coefficients. The component due to the coherent signal has been multiplied by a negative coefficient. The term due to background noise remains positive and the effect of this term is examined separately in both the frequency and time domains.

In the conventional case

$$C_{\text{noise}} = \sigma^2\mathbf{w}^T\mathbf{I}\mathbf{w} \qquad . \tag{3.6}$$

The effect of this term depends on the choice of reference element. For convenience, the lowermost element of the array is defined as the reference (see Fig. 3.1a). Thus

the kth term of the steering vector is $e^{\imath\omega\tau_k}$, where τ_k is the vertical propagation time to the kth element. Substituting this yields

$$C_{\text{noise}} = \sigma^2 \sum_{k=1}^{N} e^{2\imath\omega\tau_k} \quad . \tag{3.7}$$

In the time domain, assuming infinite bandwidth, Eq. (3.7) corresponds to a series of delta functions at $t = -2\,[\tau_{N-1}, \tau_{N-2}, \ldots, \tau_2, 0]$. For an equispaced array with inter-element vertical travel time τ this becomes $t = -2\tau\,[N-1, N-2, \ldots, 1, 0]$. The adaptive case is identical except the scalar coefficient, Λ/σ^2 replaces σ^2. Note that defining the lowermost element as the reference ensures these delta functions due to the background noise appear at negative times. Eqs. (3.1) and (3.2) are cross-correlations of a down- and up-ward propagating beam. In this model, the upward beam is a sum of time-delayed reflections of the downward beam. As the reflections lag the downward beam the correlation peaks will appear at positive times. Thus the seabed response will not be obscured by the contribution from background noise.

Neglecting the background noise component and substituting Eqs. (3.3) and (3.5) into Eqs. (3.1) and (3.2), respectively, reduces the fathometer response to

$$C(\omega) = \mathbf{w}^T \mathbf{d}\mathbf{d}^H \mathbf{w} \tag{3.8}$$

$$C_{\text{MVDR}}(\omega) = -\frac{\Lambda}{(\sigma^2 + a)^2} \mathbf{w}^T \mathbf{d}\mathbf{d}^H \mathbf{w} \quad . \tag{3.9}$$

where $\frac{\Lambda}{(\sigma^2+a)^2}$ is a positive factor.

3.3 Numerical Simulation

A simulation was constructed with a 32-element array with 0.5 m spacing (design frequency of 1500 Hz) over three reflection layers 60, 100 and 130 m below the bottom of the array with reflection coeffeicients of 0.1, 0.05 and 0.03, respectively (see Fig. 3.1a). A boxcar function with an SNR of -10 dB and a width of 1.3 ms was used as the down-going signal. The processing was done in the frequency domain with 1024 frequency bins from 0–750 Hz. A 40 Hz high pass filter

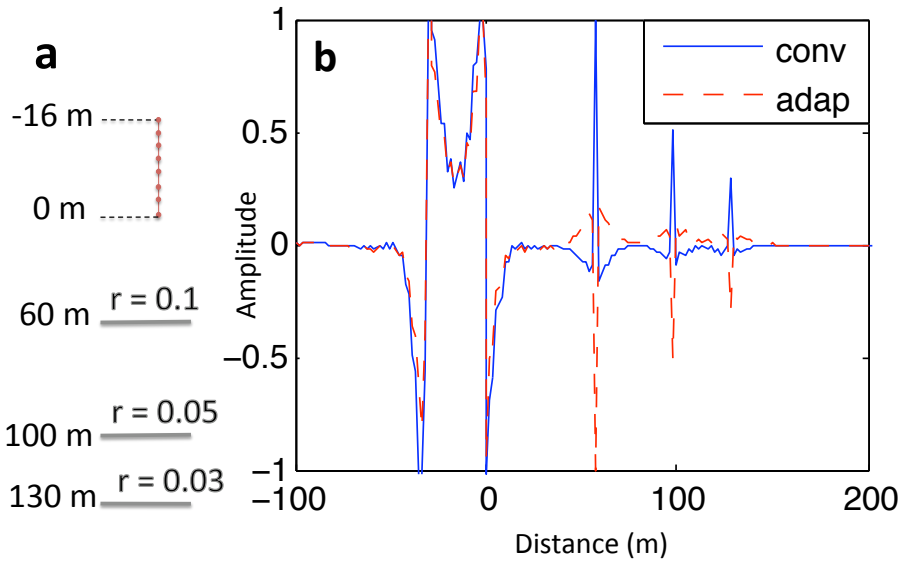

Figure 3.1: [color online] (a) A schematic of the model environment. The array is shown between −16–0 m (only every fourth hydrophone is shown) and the reflection layers with the associated reflection coefficients, r. (b) The conventional (solid) and MVDR (dashed) fathometer responses from simulated data.

was applied and the two responses were normalized such that the first reflection peak has an absolute magnitude of one.

The conventional and MVDR responses are shown in Fig. 3.1b against the depth associated with a two-way travel time in a medium with sound speed of 1500 m/s. At depths greater than 0 the conventional and MVDR traces are mirror images. In the region between −32–0 m the conventional and MVDR responses are similar. This is the region dominated by the incoherent noise term. The delta functions predicted in Eq. (3.7) are twice convolved with the box-car signal which obscures the individual peaks.

3.4 Summary

This analysis shows that adaptive processing will induce a negative sign to the seabed response given by conventional passive fathometer processing. In addi-

tion, it has been shown that the component from incoherent noise which obscures both conventional and adaptive processing can be confined to negative times by referencing the array elements relative to the bottom hydrophone.

3.5 Acknowledgements

This chapter is a reprint of the material as it appears in the Journal of the Acoustical Society of America 2009. Traer, James; Gerstoft, Peter; Song, Hee C.; Hodgekiss, William S., Acoustical Society of America, 2009. The dissertation author was the primary investigator and author of this paper.

Bibliography

[1] C. H. Harrison "Anomalous signed passive fathometer impulse response when using adaptive beam forming," J. Acoust. Soc. Am. **125**, 3511–3513 (2009).

[2] M. Siderius, C. H. Harrison and M. B. Porter, "A passive fathometer technique for imaging seabed layering using ambient noise," J. Acoust. Soc. Am. **120**, 1315–1323 (2006).

[3] P. Gerstoft, W. S. Hodgkiss, M. Siderius, C. F. Huang, and C. H. Harrison "Passive fathometer processing," J. Acoust. Soc. Am. **123**, 1297–1305 (2008).

Chapter 4

Ocean bottom profiling with ambient noise: A model for the passive fathometer

A model is presented for the complete passive fathometer response to ocean surface noise, interfering discrete noise sources, and locally uncorrelated noise in an ideal waveguide. The leading order term of the ocean surface noise contribution produces the cross-correlation of vertical multipaths and yields the depth of sub-bottom reflectors. Discrete noise incident on the array via multipaths give multiple peaks in the fathometer response. These peaks may obscure the sub-bottom reflections but can be attenuated with use of Minimum Variance Distortionless Response (MVDR) steering vectors. The seabed critical angle introduces discontinuities in the spatial distribution of distant surface noise and may introduce spurious peaks in the passive fathometer response. These peaks can be attenuated by beamforming within a bandwidth limited by the array geometry and critical angle.

4.1 Introduction

Ambient noise, which has long been considered an experimental nuisance, contains information from which environmental parameters can be inferred[1, 2] and correlations of oceanic ambient noise allows inference of medium properties[3,

4, 5, 6]. Application of array processing techniques enhance the fidelity of such correlations and may improve the performance of geophysical inversions of ambient noise.

One such array processing technique, beamforming on a vertical hydrophone array, can focus on vertically propagating noise that contains noise reflected from and therefore information about the seabed. This can be used to infer ocean bottom properties such as seabed critical angle[7, 8], reflection loss versus angle of incidence[9] and the depth of sub-bottom reflection layers [10, 11, 12, 13, 14, 15, 16]. The process of obtaining the latter by cross-correlating noise is referred to as passive fathometry. The noise source for the passive fathometer is wind and wave generated surface noise which, is often modeled as an infinite sheet of surface noise sources[17, 18, 19]. These models imply that there is much more acoustic energy propagating horizontally in the waveguide than vertically and hence, directional sensitivity attained by adaptive beamforming[15] and/or velocity sensors[11] may yield an improvement in the passive fathometer response.

Recent experiments with a drifting vertical array[20] have shown the bottom-reflection can be obscured by interference from shipping noise[15]. In order to determine the practical limits of the passive fathometer, a detailed analysis of its response to arbitrary noise fields is required. We use a simple ocean noise model[21] with three sources: correlated noise generated near the ocean surface by the action of wind and waves, discrete noise generated by point sources at arbitrary positions in the water column (i.e. ships), and spatially uncorrelated white noise due to electrical noise within the array. Both conventional and adaptive beamforming are considered.

As beamforming increases the contribution of vertically propagating noise to the passive fathometer response, a simple model is first considered in which the ocean surface produces only vertically propagating plane waves. This model allows many of the features of the passive fathometer response to be addressed qualitatively with a minimum of algebra. The passive fathometer model presented here also considers spatial aliasing, in which the array gain is applied to noise towards which the array is not intentionally steered.

Depending on the dimensionality of the system and noise source, the time domain Green's function can be proportional to the noise cross-correlation, its time derivative, time integral or fractional derivative[11, 22]. Assuming the dominant component of the passive fathometer response is due to vertically propagating noise, the system is approximately 1D and thus the Green's function is proportional to the noise correlation.

Prior models for the passive fathometer response have either numerically evaluated the integration over the ocean surface[10, 11, 12], or assumed that the array is preferentially sensitive to vertically propagating noise in order to make the surface integration tractable[11, 12]. The model presented here details how beamforming attenuates horizontally propagating signals (Sec. 5.2) and how the stationary phase approximation shows that the cross-correlation of vertically separated sensors under an infinite surface sheet of noise is preferentially weighted towards vertically propagating noise (App. A). Thus the leading order behavior is computed analytically.

The model presented is restricted to a horizontally stratified waveguide with a constant sound speed profile in the water column and a perfectly uncorrelated surface sheet of noise sources. These approximations are not sufficient to describe a real ocean, however small variations from this model will not effect the leading order characteristics of the model passive fathometer response.

4.2 Theory

Consider an m-element vertical array positioned in a water column of depth Δ and uniform sound speed c (Fig. 4.1). Define the bottom hydrophone depth as z_a and the inter-element separation as d, such that the inter-element travel time is $\tau = d/c$. It is convenient to define $\psi = e^{\imath\omega\tau}$ where ω is the angular frequency. In the frequency domain, multiplication of the data from the pth hydrophone, $x_p(\omega)$, by ψ is equivalent to shifting in the time domain by τ to yield $x_p(t+\tau)$. The array beam steered to add in phase vertically downward propagating noise D, and the corresponding beam steered to add in phase vertically upward propagating noise

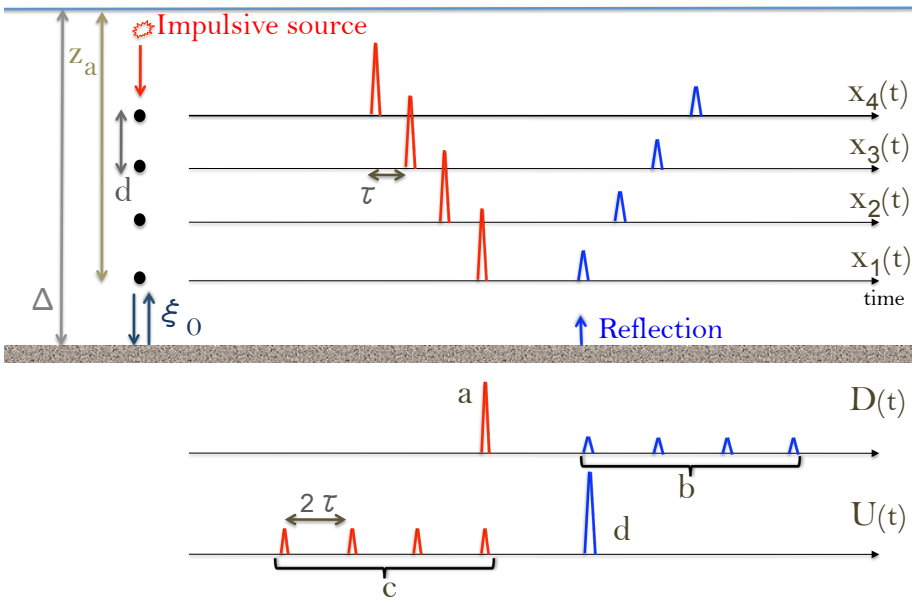

Figure 4.1: (Color online) Key variables in the analytical description of the passive fathometer. The water column depth, Δ, the depth of the lowermost array element, z_a, the inter-element separation, d, the inter-element propagation time for vertical signals, τ, the two way travel distance between the array and seabed, ξ_0, the data from the pth hydrophone, $x_p(t)$. $D(t)$ and $U(t)$ are the time domain form of the beams defined in Eq. (4.1). a, b, c and d are the key features within these beams.

U, are

$$\begin{aligned} D(\omega) &= \sum_{p=1}^{m} \psi^{-(p-1)} x_p(\omega) = \mathbf{w}^H \mathbf{x} \\ U(\omega) &= \sum_{p=1}^{m} \psi^{(p-1)} x_p(\omega) = \mathbf{w}^T \mathbf{x} \end{aligned} \tag{4.1}$$

where we have defined the steering vector for downward propagating noise as

$$\mathbf{w}^T = [1, \psi, \psi^2, \ldots, \psi^{(m-2)}, \psi^{(m-1)}] \tag{4.2}$$

and the reference phone ($p = 1$) is the lowermost element. The superscripts T and H represent a matrix transpose and Hermitian transpose respectively, such that $\mathbf{w}^H = (\mathbf{w}^*)^T$.

Consider a simple ocean noise model in which the environment is range independent and surface noise is spatially uncorrelated. Define the sound incident

on the above array as

$$\mathbf{x}(\omega) = \int_{r=0}^{\infty} \mathbf{g}(r, z = z_0; z_p) s(r, \omega) 2\pi r \, dr + \sum_{j=1}^{J} \mathbf{g}(r_j, z_j; z_p) n_j(\omega) + \mathbf{u} \tag{4.3}$$

where $s(r, \omega)2\pi r \, dr$ is the signal generated by the annulus of ocean surface around the array between radii r and $r + dr$, $\mathbf{g}(r, z; r_p, z_p)$ is a vector of Green's functions from the source at depth z and radial distance r to each hydrophone at depth z_p. z_0 is a depth near the ocean surface. The integral over r accounts for the noise generated by the ocean surface, which is assumed infinite. Assuming the presence of J discrete sources with frequency dependent amplitude $n_j(\omega)$, $\mathbf{g}(r_j, z_j)$ is a vector of Green's functions from each discrete source to the array. $\mathbf{u}$ denotes the uncorrelated white noise at each element. These three terms are referred to as the correlated noise, discrete noise and white noise[21]. These terms are assumed to be independent.

Using the steering vector as defined in Eq. (4.2), the fathometer response is[11]

$$C(\omega) = \mathbf{w}^T \mathbf{R}(\omega) \mathbf{w} \tag{4.4}$$

with Cross-Spectral Density Matrix (CSDM), $\mathbf{R}$ given by

$$\mathbf{R}(\omega) = E\left[\mathbf{x}(\omega)\mathbf{x}^H(\omega)\right] \tag{4.5}$$

where $E[\ ]$ denotes the expectation operator. As detailed in App. 4.A, substituting Eqs. (4.3) and (4.5) into Eq. (4.4) gives the fathometer model response as

$$C(\omega) = |S(\omega)|^2 \int_{r=0}^{\infty} \mathbf{w}^T \mathbf{g}\mathbf{g}^H \mathbf{w} 2\pi r \, dr + \sum_{j=1}^{J} |N_j(\omega)|^2 \mathbf{w}^T \mathbf{g}_j \mathbf{g}_j^H \mathbf{w} + \sigma^2 \mathbf{w}^T \mathbf{I} \mathbf{w} \tag{4.6}$$

where $\mathbf{I}$ denotes the identity matrix, $|S(\omega)|^2$ is the power spectrum per unit area of the surface noise with absolute magnitude independent of r and $|N_j(\omega)|^2$ is the power spectrum of the jth source. The individual terms are now examined in detail. A final subsection (Sec. 4.2.4) will consider the effect of Minimum Variance Distortionless Response (MVDR) beamforming.

4.2.1 White noise

The white noise component of the fathometer response is given by

$$\sigma^2 \mathbf{w}^T \mathbf{I} \mathbf{w} \;=\; \sigma^2 \sum_{p=1}^{m} \psi^{(p-1)} \psi^{(p-1)} = \sigma^2 \Psi \tag{4.7}$$

where $\Psi = \sum_p \psi^{2(p-1)}$. Assuming infinite bandwidth, each term in the summation gives a δ-function in the time domain located at $-2(p-1)\tau$. With a finite bandwidth the δ-functions become peaks of finite width with heights that scale with σ^2. The summation results in m equispaced δ-functions between $t = -2(m-1)\tau$ and $t = 0$. This is the only region in the time domain fathometer response that shows contribution from uncorrelated noise. As this region will be referred to repeatedly in this analysis, it is designated the sensor noise region.

4.2.2 Correlated noise

The correlated noise component contains an integral over the infinite ocean surface [Eq. (4.6)]. Before considering this integral in detail (Sec. 4.2.2 and App. 4.A) the leading order behavior can be obtained by considering the array response to a 1D vertical noise field. Neglecting non-vertical noise can be justified for two reasons: (1) contributions to the cross-correlation from sources situated on a ray-path that passes directly through both sensors are added in phase and hence are preferentially weighted[23, 24] and (2) the preferential weighting of vertical noise is increased by beamforming [Eq. (4.1)] and more so by MVDR beamforming. In Sec. 4.2.2 this will be shown to be a good first order approximation.

Vertical noise model

Assuming the surface signal is generated by a point source at $r = 0$ and depth z_0, $s(r, z, \omega) = \delta(r)\delta(z - z_0)s(\omega)$. Substituting the correlated term from Eq. (4.3) into Eq. (4.5) gives the component of the CSDM due to correlated noise

$$\mathbf{R}_c(\omega) = |S(\omega)|^2 \mathbf{g}(r{=}0, z{=}z_0; z_p) \mathbf{g}(r{=}0, z{=}z_0; z_p)^H \quad . \tag{4.8}$$

The Green's function for the pth hydrophone is

$$[\mathbf{g}]_p = e^{-\imath\omega\frac{z_a-z_0}{c}}\left[\psi^{(p-1)}+\psi^{-(p-1)}\sum_{l}^{L}\Gamma_l e^{-\imath\omega\xi_l/c}\right] \tag{4.9}$$

where the first term accounts for the downward propagating path and the summation accounts for a set of upward propagating reflections. Γ_l is the reflection coefficient of the lth reflecting layer and ξ_l is twice the distance from the array bottom, z_a to the lth layer. We assume no reflections between layers or reflections from the ocean surface as, assuming the reflection coefficient from each interface is small, the contribution from paths involving multiple reflections are negligible. Expanding the following analysis to include arbitrary reflections is conceptually simple and algebraically tedious and is described in App. 4.A.2.

Using the steering vector defined in Eq. (4.2), the vector of Green's functions for the array can be written as

$$\mathbf{g} = e^{-\imath\omega(z_a-z_0)/c}\left[\mathbf{w}+H(\omega)\mathbf{w}^*\right] \tag{4.10}$$

where $H(\omega)$ is seabed transfer function

$$H(\omega) = \sum_{l}^{L}\Gamma_l e^{-\imath\omega\xi_l/c} \tag{4.11}$$

and Γ_l is the reflection coefficient of the lth interface.

Substituting Eqs. (4.11–4.10) into Eq. (4.8) gives the CSDM elements

$$\begin{aligned}[\mathbf{R}_c]_{pq} = \quad & |S(\omega)|^2\Big[(1+|H|^2)\psi^{q-p} \\ & +H\psi^{-(p+q-2)}+H^*\psi^{(p+q-2)}\Big]\end{aligned} \tag{4.12}$$

which, using Eq. (4.4), gives the passive fathometer response component due to correlated noise

$$C_c(\omega) = \quad |S(\omega)|^2\Big[m^2H+(1+|H|^2)m\Psi+H^*\Psi^2\Big] \quad . \tag{4.13}$$

Transforming to the time domain gives,

$$C_c(t) \quad = \zeta(t) * (T_1+T_2+T_3+T_4) \tag{4.14}$$

where $*$ denotes convolution and

$$\begin{aligned} T_1 &= m^2 \sum_l \Gamma_l \delta(t - \xi_l/c) \\ T_2 &= m \sum_{p=1}^{m} \delta(t + 2(p-1)\tau) \\ T_3 &= \eta(t) * T_2(t) \\ T_4 &= m \sum_{l=1}^{L} \sum_{p=1}^{2m} \left(1 - \left|1 - \frac{p}{m}\right|\right) \Gamma_l \delta(t + \xi_l/c + 2(p-1)\tau) \ , \end{aligned} \tag{4.15}$$

where $\zeta(t)$ is the inverse Fourier transform of $|S(\omega)|^2$ (and therefore the autocorrelation of the surface noise). As the surface noise is assumed to be white and band limited, $\zeta(t)$ is a sinc-function with the pulse-width determined by the processing bandwidth. $\delta(t)$ is the Dirac δ-function and $\eta(t)$ is the time-domain representation of $|H(\omega)|^2 = (\sum_j \Gamma_j e^{-\imath\omega\xi_j/c})(\sum_l \Gamma_l e^{\imath\omega\xi_l/c})$

$$\eta(t) = \sum_{j,l}^{L} \Gamma_j \Gamma_l \delta\left(t - \frac{\xi_j - \xi_l}{c}\right) \quad . \tag{4.16}$$

The schematic form of these terms are shown in Fig. 4.2. All of the terms T_1–T_4 in the time domain are formed by the summation of m^2 δ-functions, each corresponding to one element of the $m \times m$ CSDM [Eq. (4.12)]. Due to the action of the steering vectors all the δ-functions in T_1 are produced at the same position for all values of p and q [Eq. (4.13)], resulting in a single peak with amplitude increased by a factor of m^2 for each reflecting layer. T_1 and T_4 are the contribution of the up-going and down-going signals correlated with each other and the m^2 gain applied to T_1 is consistent with both the vertical up-going and down-going signals subject to an array gain of m, Ref. [25]. This is the feature of interest for ocean bottom profiling and, other than T_3, which is scaled by Γ^2 and is likely to be small amplitude, T_1 is the only term due to surface noise that contains peaks at positive correlation times.

T_4 gives L sets of $2m$ δ-functions [the position of the m^2 δ-functions is now a function of p and q, Eq. (4.13)] between $t = -\xi_l/c - 4(m-1)\tau$ and $t = -\xi_l/c$, the latter of which is the negative of the two-way travel time of the lth layer. T_2 [produced by the autocorrelation of the down-going signal, Eq (4.10)] gives a set

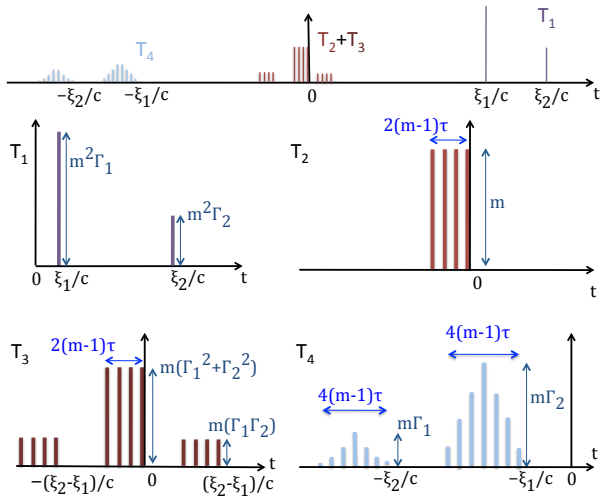

Figure 4.2: (Color online) Schematic of the terms from Eq. (4.15) for the case of a four element array (m=4) and two reflecting layers. The horizontal axis is time and the vertical axis is the passive fathometer response. The top plot is the complete time series with the lower four examining the individual components. Note the array gain of m^2 applied to T_1.

of m equispaced δ-functions in the sensor noise region of amplitude m, as the δ-function location is now a function of p only. T_3 (up-going signal) gives the same δ-functions convolved with the seabed impulse response and its time-reversed form.

Inclusion of non-vertical noise

The analysis of the previous section is now expanded to include signal contributions from an infinite ocean surface. The Green's function between a source at $\mathbf{r} = (r, z)$ and a receiver at $\mathbf{r}_p = (0, z_p)$ in a waveguide is[24, 28]

$$G(\mathbf{r}_p; \mathbf{r}) \quad = \quad \sum_{\alpha}^{1} \Gamma^{b_\alpha} \frac{e^{\imath \frac{\omega}{c} L_\alpha(\mathbf{r}_p, \mathbf{r})}}{4\pi L_\alpha(\mathbf{r}_p, \mathbf{r})} \tag{4.17}$$

where the subscript α distinguishes between different multipaths and b_α is the number of reflections from the seabed in the α path. L_α the travel-distance from receiver to source along the α path. Substituting Eq. (4.17) into the correlated component of Eq. (4.6). The integral over r can be computed by the stationary phase approximation[23, 24, 26] and, as detailed in App. 4.A, assuming one

seabed reflecting layer, a reflection coefficient Γ independent of grazing angle and no surface reflections, this result can be simplified to yield

$$C_c(\omega) = \frac{-\imath c|S(\omega)|^2}{8\pi\omega}\sum_{p=1}^{m}\sum_{q=1}^{m}\Big[(1+\Gamma^2)\frac{\psi^{2(q-1)}}{(q-p)d} + \Gamma\frac{\psi^{-\xi_0/d}+\psi^{\xi_0/d+2(p+q-2)}}{\xi_0+(p+q-2)d}\Big] \;\forall\; p\neq q \quad . \tag{4.18}$$

This is a summation of terms of the general form $B(p,q)\psi^{\mu(p,q)}$ which gives a set of δ-functions of amplitude $B(p,q)$ at location $-\mu(p,q)\tau$ in the time domain. Thus the first term in the response in Eq. (4.18), in the time domain, is a set of δ-functions at $-\mu\tau = -2(q-1)\tau$ with an amplitude of $B = c|S|^2(1+\Gamma^2)/[(q-p)d]$ for all values of $p \neq q$. The fathometer response has a $1/\omega$ dependence, consistent with other analytical treatments of ambient-noise cross-correlations in 3-D[22, 24]. This can be removed by the multiplication by ω, which is equivalent to a differentiation with respect to time in the time domain.

The terms in Eq. (4.18) are produced in the same locations as those in Eq. (4.15) and differ only in amplitude. The $\psi^{2(q-1)}$ term corresponds to $T_2 + T_3$, assuming only a single reflection from the seabed. The $\psi^{-\xi_0/d}$ term corresponds to T_1 and produces a single peak at ξ_0/c. The $\psi^{\xi_0/d+2(p+q-2)}$ term corresponds to T_4.

Note that the diagonal terms ($p = q$) of Eq. (4.18), are infinite. This is because the diagonal terms consist of autocorrelations for which the phase variation between the signals is zero and the stationary phase approximation is not valid.

4.2.3 Discrete sources

For simplicity, we consider a single discrete source ($J = 1$) in the waveguide described in Sec. 4.2.2. The analysis is extended to include more layers and higher order reflections in App. 4.A and moving sources in App. 4.B. In this case there are six distinct paths that undergo a single seabed reflection as shown in Fig. 4.3. In Fig. 4.3 the propagation paths are straight lines as the sound speed is constant throughout the water column. Introducing a variable sound speed will lead to curved paths that are algebraically more complex to describe. However it is still the path length difference between multipaths that determines the position of the

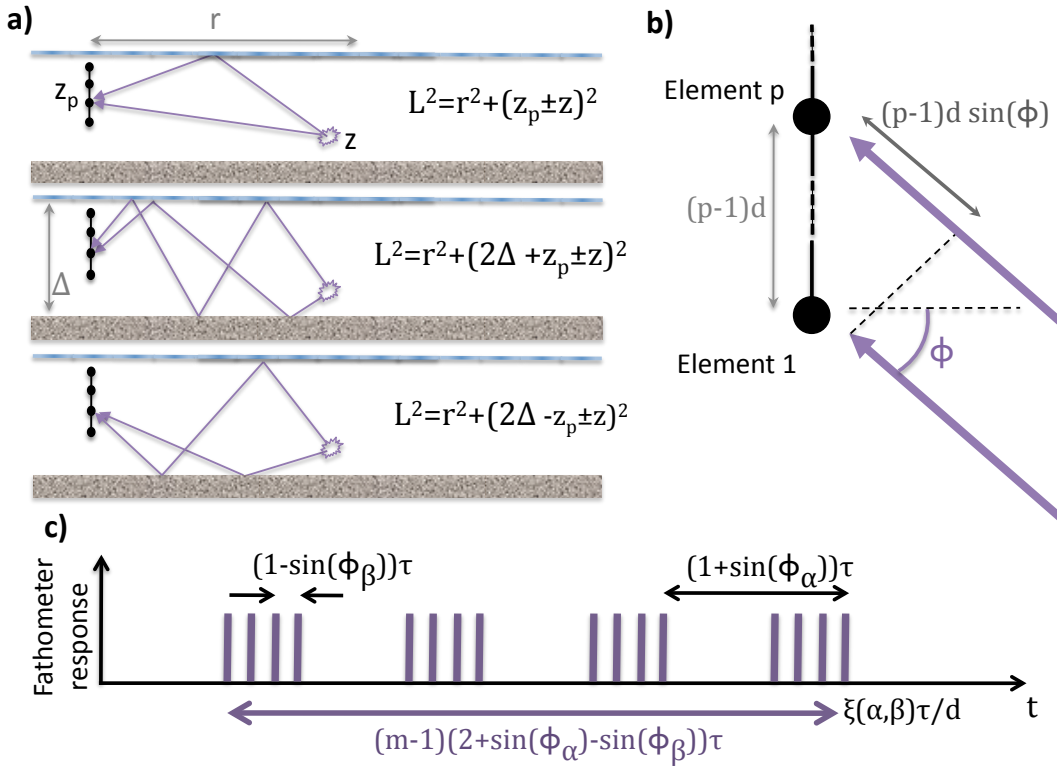

Figure 4.3: (Color online) (a) Multipaths in a waveguide with no more than one seabed reflection. (b) The phase difference between the lowermost element and the pth element is given by $(p-1)d\sin\phi$ where ϕ is the angle of incidence. (c) Time domain fathometer response induced by the correlation of two δ-functions incident from angles ϕ_α and ϕ_β on a four element array.

correlation peak. Substituting Eq. (4.17) into the discrete component of Eq. (4.6) and allowing for six possible multipaths [Fig. 4.3(a)] gives the component of the passive fathometer response due to discrete noise

$$\begin{aligned} C_d(\omega) &= \sum_{p,q=1}^{m}\sum_{\alpha,\beta=0}^{6}|N_j(\omega)|^2\frac{\Gamma^{b_\alpha+b_\beta}}{(4\pi)^2L_\alpha L_\beta}\psi^{(p+q-2)+\frac{L_\alpha-L_\beta}{d}} \\ &= \sum_{p,q=1}^{m}\sum_{\alpha,\beta=0}^{6}B(p,q,\alpha,\beta)\psi^{\mu(p,q,\alpha,\beta)} \end{aligned} \tag{4.19}$$

where p and q denote the indices of the array elements.

Assuming infinite bandwidth, each term $B\psi^\mu$ gives a δ-function in the time domain at $-\mu\tau$ with an amplitude B. Assuming paths α and β are incident on the

array as plane waves incident at angles ϕ_α and ϕ_β to the horizontal the path length differences of the α and β rays incident on the pth and qth elements respectively can be computed geometrically, as shown in Fig. 4.3(b). This yields

$$\begin{aligned} \mu &= (p+q-2) - \frac{L_\beta - L_\alpha}{d} \\ &= (p-1)(1+\sin\phi_\alpha)+(q-1)(1-\sin\phi_\beta)-\frac{\xi(\beta,\alpha)}{d} \end{aligned} \tag{4.20}$$

where $\xi(\beta,\alpha)$ is the path length difference at the lowermost hydrophone of the array. As such, signals with correlated multipaths will give sets of m^2 δ-functions at times $\xi/c-4(m-1)\tau \leq t \leq \xi/c$. The δ-functions will be spread over the entirety of this region if $\sin\phi_\alpha = 1$ and $\sin\phi_\beta = -1$, which occurs when both signals are vertical and is directly analogous to T_4 (Sec. 4.2.2). For any other values of ϕ_α and ϕ_β the δ-functions will be spread over a smaller region, as illustrated in Fig. 4.3(c). When a source is close enough to the array that the plane wave approximation is not valid, the peak locations will be slightly perturbed from the values presented here.

If $\alpha = \beta$ (equivalent to autocorrelating a signal as it implies identical travel paths), then $\xi(\alpha,\alpha) = 0$ and μ is constrained to be $0 < \mu < 2(m-1)\tau$. When summed over p and q, this gives a set of δ-functions in the sensor noise region.

Every pairwise combination of $\alpha \neq \beta$ produces two sets of m^2 δ-functions (one set at positive and one set at negative correlation time offsets, between $\pm\xi/d-4(m-1)\tau$ and $\pm\xi/d$). A discrete source incident on the array via N significant multipaths will therefore produce $N(N-1)/2$ sets in the positive time-domain that may obscure the sea-bed response.

4.2.4 MVDR fathometer processing

Minimum Variance Distortionless Response (MVDR) processing has been used to improve the passive fathometer response in the presence of interfering noise[11, 15]. It is identical to the processing in the previous sections with the steering vectors in Eq. (4.4) replaced by the MVDR steering vectors for upward

and downward propagating waves[27]

$$\begin{aligned}\tilde{\mathbf{w}}_U &= \frac{\mathbf{R}^{-1}\mathbf{w}^*}{\mathbf{w}^T\mathbf{R}^{-1}\mathbf{w}^*} \\ \tilde{\mathbf{w}}_D &= \frac{\mathbf{R}^{-1}\mathbf{w}}{\mathbf{w}^H\mathbf{R}^{-1}\mathbf{w}}\end{aligned} \tag{4.21}$$

where ˜ indicates use of MVDR processing. Substituting these steering vectors into Eq. (4.4) gives the MVDR passive fathometer response

$$\tilde{C}(\omega) = \tilde{\mathbf{w}}_U\mathbf{R}\tilde{\mathbf{w}}_D = \Lambda\mathbf{w}^T\mathbf{R}^{-1}\mathbf{w} \tag{4.22}$$

where $\Lambda = |\mathbf{w}^H\mathbf{R}^{-1}\mathbf{w}|^{-2}$ is a positive normalization factor. Other adaptive processing methods with additional constraints may be used and as also they provide a greater weighting to vertically propagating contributions they will yield a similar response. Given $J+1$ sources incident on the array [from J discrete interferers and the vertical component of the correlated noise, which is designated as the $(J+1)$th correlated signal and is asymptotically dominated by vertically propagating noise (App. 4.A) and hence can be accounted for with a single eigenvector], an eigendecomposition of the CSDM gives

$$\mathbf{R} = \sum_{j=1}^{J+1}(b_j+\sigma^2)\mathbf{u}_j\mathbf{u}_j^H + \sum_{j=J+2}^{m}\sigma^2\mathbf{u}_j\mathbf{u}_j^H \tag{4.23}$$

where b_j is the component of the eigenvalue due to the jth coherent source and scales as the trace of the CSDM associated with the jth coherent signal (i.e. $|N_j|^2\mathbf{g}_j\mathbf{g}_j^H$ for all $j \le J$ and $|S(\omega)|^2\int\mathbf{g}\mathbf{g}^H 2\pi r\,dr$ for $j = J+1$). The matrix inverse is then[14]

$$\begin{aligned}\mathbf{R}^{-1} &= \sum_{j=1}^{J+1}\frac{1}{(b_j+\sigma^2)}\mathbf{u}_j\mathbf{u}_j^H + \sum_{j=J+2}^{m}\frac{1}{\sigma^2}\mathbf{u}_j\mathbf{u}_j^H \\ &= \frac{1}{\sigma^2}\left[\sum_{j=1}^{J+1}\frac{\sigma^2}{(b_j+\sigma^2)}\mathbf{u}_j\mathbf{u}_j^H + \mathbf{I} - \sum_{j=1}^{J+1}\mathbf{u}_j\mathbf{u}_j^H\right] \\ &= \frac{1}{\sigma^2}\left[\mathbf{I} - \sum_{j=1}^{J+1}\frac{b_j\mathbf{u}_j\mathbf{u}_j^H}{(b_j+\sigma^2)}\right] \\ &= -\frac{|S(\omega)|^2\int\mathbf{g}\mathbf{g}^H 2\pi r\,dr}{(b_{J+1}+\sigma^2)^2} - \sum_{j=1}^{J}\frac{|N_j(\omega)|^2\mathbf{g}_j\mathbf{g}_j^H}{(b_j+\sigma^2)^2} + \frac{1}{\sigma^2}\mathbf{I}\end{aligned} \tag{4.24}$$

where we have utilized $\sum \mathbf{u}_j \mathbf{u}_j^H = \mathbf{I}$. This contains the same components as the CSDM [Eq. (4.28) in App. 4.A] due to correlated noise, J discrete interferers and white noise, but all except the component due to incoherent noise have been multiplied by negative factors. This is consistent with previous models that considered only surface noise[13] and surface noise as well as sensor noise[14].

Note that each component of the matrix inverse is scaled by $1/(b_j + \sigma^2)$. This acts to attenuate the contribution of strong signals to the fathometer response. The normalization factor is equivalent to[27]

$$\Lambda(\omega) = U_{MVDR}(\omega) D_{MVDR}(\omega) \tag{4.25}$$

where $U_{MVDR} = (\mathbf{w}^T \mathbf{R}^{-1} \mathbf{w}^*)^{-1}$ and $D_{MVDR} = (\mathbf{w}^H \mathbf{R}^{-1} \mathbf{w})^{-1}$ are the estimates of the up- and down-ward propagating spectral power obtained by the MVDR beamformer. This term is large at frequencies with large power contributions from vertical directions and will counteract the attenuation due to the $1/(b_{J+1} + \sigma^2)$ factor.

Thus the MVDR fathometer response is qualitatively similar to that of the conventional passive fathometer but all components except that due to incoherent noise are multiplied by a negative factor[13, 14] and the contribution from non-vertical sources is reduced by a factor proportionate to the power of that signal incident on the array.

4.3 Numerical simulation

4.3.1 Two-dimensional noise model

A simple fathometer model was generated assuming only vertically propagating surface noise, one discrete source and sensor noise. The discrete source is assumed stationary as implementations of the passive fathometer have used integration times[15] on the order of 100 s and the change in path-length from a distant ship would be negligible over this time (moving sources are considered in App. 4.B). Although only a single interferer is considered here the results are easily generalized to multiple interfering sources as the contribution from multiple interferers

add linearly provided the discrete sources are uncorrelated. A 16-element array with equispaced elements of 0.18 m separation (design frequency, $f_d = 4167$ Hz and total length 2.88 m) in uniform sound speed of 1500 m/s was used. A similarly spaced array with 32 elements was used in Ref. [15]. Here the number of array elements has been halved for clarity. The vertical noise was assumed to reflect off two layers at distances 50 and 58 m from the array bottom with reflection coefficients of 0.1 and 0.06 respectively.

The waveform used for both the vertical and interfering signals was a 60 μs box-car function which, when autocorrelated, becomes a triangle of width 120 μs. As the signal waveform is a narrow peak, the power spectrum of the signals are nearly flat. The vertical signal power spectrum was -20 dB relative to the power of the white noise. The discrete signal was assumed to be incident on the array via three multipaths with arrival angles of 5, -10 and 20° to broadside, with power spectra of 20, 0 and -20 dB respectively, relative to the white noise. The path length differences of the three multipaths were 0, 20 and 45 m.

A sampling rate of $8f_d$ (33 kHz) was used to generate the signals and all processing was done with 2^{13} point Fourier transforms. The data for each signal was processed with two bandwidths, f_d (10–4167 Hz) which ensured no aliasing (see Sec. 4.3.2) occurred, and $4f_d$ (10–16.5 kHz). The large bandwidth allows the individual peaks described in Sec. 5.2 to be obtained. When computing the passive fathometer response with the large bandwidth, the response of each component of the CSDM (i.e., the CSDM formed from each possible combination of non-independent signals) was computed separately to prevent artifacts due to aliasing. The responses computed with a bandwidth of f_d were normalized with respect to the reflection peak at 50 m, and those computed with $4f_d$ were scaled to have the same peak magnitude as their small bandwidth counterparts.

The passive fathometer response computed with a bandwidth of f_d is shown in Fig. 4.4. Both the conventional and MVDR responses are dominated by peaks in the sensor noise region and both responses show peaks at ± 20 m from discrete noise. The seabed reflection peaks in the conventional response are not visible on this scale. The individual contributions from the fathometer model components

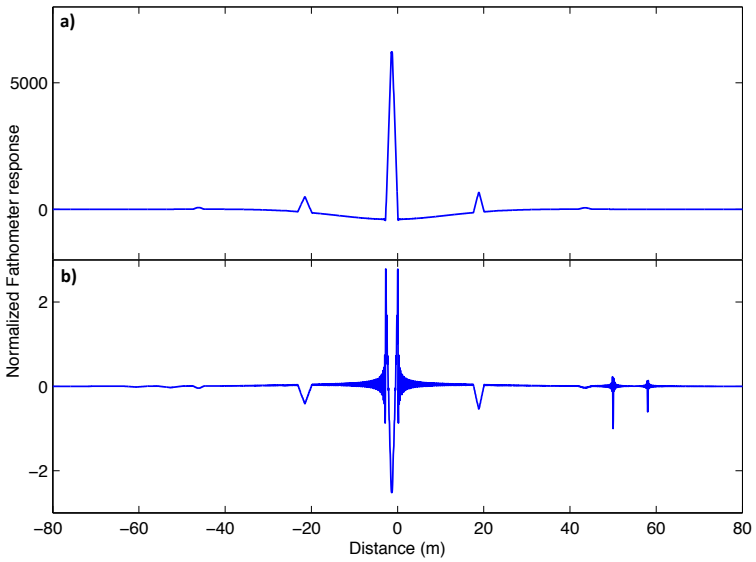

Figure 4.4: (Color online) The conventional (a) and MVDR (b) passive fathometer response for the noise model described in Sec. 4.3.1 computed with bandwidth of f_d (10–4167 Hz). The horizontal axis is the vertical distance corresponding to a two way travel time. Both responses are normalized to the correlation peak due to the seabed reflection at 50 m.

are shown in Figs. 4.5–4.7.

Conventional response

The conventional passive fathometer response to each combination of signals is shown in Figs. 4.5–4.6. The cross-term between the up and downward propagating signals gives δ-functions at the location of the reflecting layers at 50 and 58 m [Fig. 4.5(a)], consistent with T_1 of Eq. (4.15). The m^2 array gain increases the height of these peaks.

The component due to downward propagating noise gives a set of $m = 16$ equispaced peaks in the sensor noise region consistent with T_2 of Eq. (4.15) which contains a summation of m δ-functions spaced by τ. The right-most peak is a triangle with the left edge located at 0, consistent with a δ-function at 0 twice convolved with a box-car function. The width of the triangle is 120 μs $\times$1500 m/s = 0.09 m. These peaks grow broader when smaller bandwidths are processed.

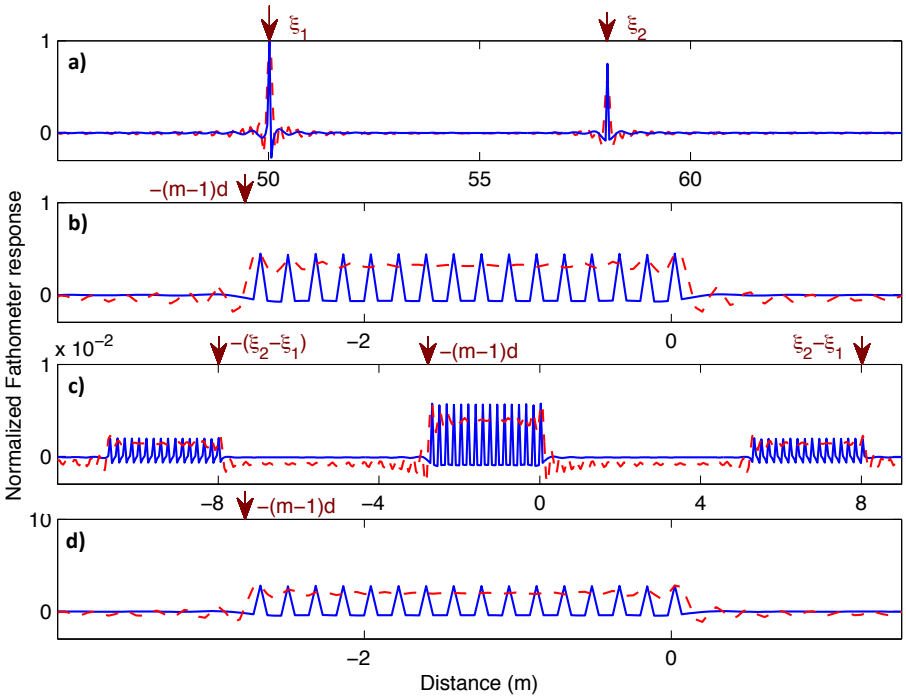

Figure 4.5: (Color online) The conventional passive fathometer response computed with a bandwidth of $4f_d$ (0–16.5 kHz, solid) and f_d (10–4167 Hz, dashed) to the following components of the CSDM plotted against the distance associated with a two way travel time. (a) The cross-term between downward and upward propagating noise [T_1 from Eq. (4.15)], (b) downward propagating noise (T_2), (c) upward propagating noise (T_3), and (d) white noise.

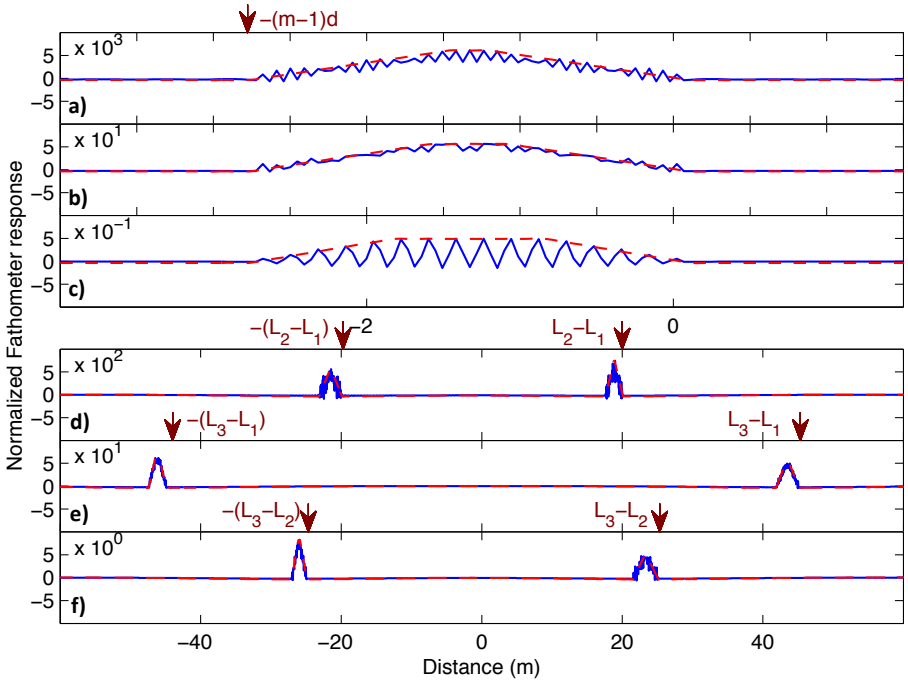

Figure 4.6: (Color online) As Fig. 4.5 for (a)–(c) the three multipath arrivals from the discrete source, (d)–(f) the cross terms between the first and second, first and third and second and third discrete source multipaths, respectively.

When a bandwidth of f_d is used, the individual peaks merge into a single broad peak that spans the sensor noise region.

The upward propagating noise gives multiple sets of δ-functions [Fig. 4.5(c)] consistent with T_3 of Eq. (4.15). In this case, η is a set of three δ-functions at $-8, 0, 8\,\mathrm{m}$ with heights of $[\Gamma_1\Gamma_2, \Gamma_1^2 + \Gamma_2^2, \Gamma_2\Gamma_1] = [0.006, 0.0136, 0.006]$. Note the upward propagating signal peaks are 2 orders of magnitude smaller than the downward [Fig. 4.5(b) and (c)], consistent with a reflection coefficient of 0.1. The term T_4 is not shown as it will neither interfere with the signal of interest (T_1) or be the largest term in the noise correlation.

The white noise gives m equispaced peaks in the sensor noise region [Fig. 4.5(d), Eq. (4.7)], as do the autocorrelations of the three multipaths of the discrete signal [Fig. 4.6(a)–(c), Eq. (4.20) with $\alpha = \beta$]. The response due to the three discrete multipaths scale, as expected, with relative peak heights of $0, -20$ and $-40\,\mathrm{dB}$.

The cross-terms associated with the discrete multipaths are the only terms producing a response in the positive time domain [Fig. 4.6(d)–(f)] other than the seabed reflection (T_1). All three cross-terms give one set of peaks in the positive time domain and one set in the negative time domain. The right-most peak of both sets occurs at $\pm\xi/d$, which is consistent with Eq. (4.20) where ξ is $\pm 20, \pm 45$ and ± 25 m respectively.

The smallest discrete cross-term [Fig. 4.6(f)] is larger than the vertical cross-term [Fig. 4.5(a)] and the other discrete cross-terms [Fig. 4.6(d) and (e)] are orders of magnitude larger still. Thus the dominant terms for $t > 0$ of the conventional passive fathometer response are due to the discrete source while the vertical seabed reflection is obscured, as shown in Fig. 4.4(a) in which the peak from Fig. 4.6(d) is the only prominent peak outside the sensor noise region.

MVDR response

In accordance with Eq. (4.24), the components of the conventional response were multiplied by $\frac{-1}{b_j+\sigma^2}$, except for the white noise term which was multiplied by σ^{-4}. In this case, σ was 1 and b_j is the trace of the CSDM associated with the jth coherent signal. The results are shown in Fig. 4.7.

All of the components have been multiplied by a negative factor, except the white noise, and the relative amplitudes are now different. The largest component is the white noise [Fig. 4.7(d)] followed by the vertical cross-term [Fig. 4.7(a)] which, in contrast to the conventional passive fathometer, is larger than the cross-term peaks due to the discrete source [Fig. 4.7(h)–(j)].

Although the peaks have been rescaled relative to the conventional response, the locations have remained unchanged. This is consistent with Eq. (4.24) which shows that the CSDM inverse used in MVDR processing contains the same components as the CSDM rescaled by real multiplicative factors.

4.3.2 Three-dimensional surface noise model

The response of the passive fathometer to an infinite sheet of sources near the surface, as considered in Sec. 4.2.2, is now simulated. Only the surface noise

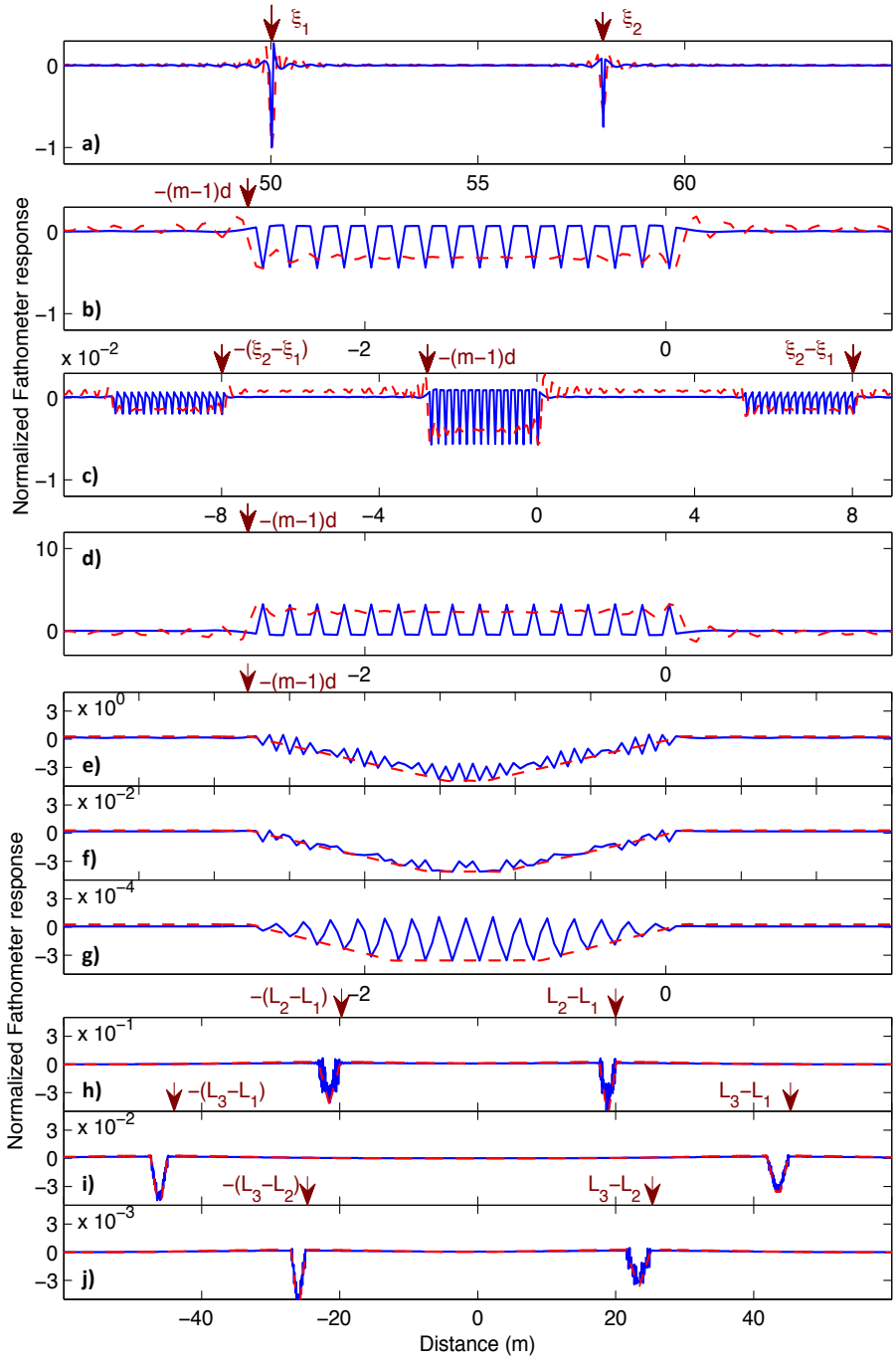

Figure 4.7: (Color online) The MVDR passive fathometer response to the same components of the CSDM as shown in (a)–(d) Fig. 4.5 and (e)–(j) Fig. 4.6

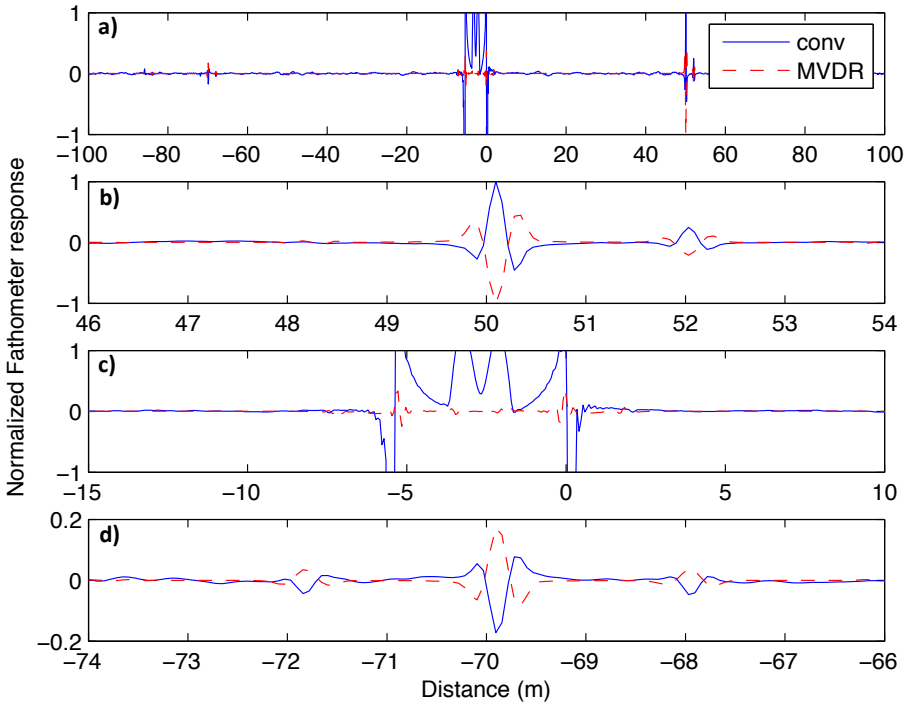

Figure 4.8: (Color online) The wavenumber integration simulation of the conventional and MVDR passive fathometer response two an infinite sheet of noise at two way travel time ranges of (a) −100 to 100, (b) 46 to 54, (c) −15 to 10 and (d) −74 to −66 m.

is shown, as discrete interferers and sensor noise yield results very similar to those in Sec. 4.3.1. A wavenumber integration[29] simulation of the noise generated by an infinite two-dimensional ocean surface in a horizontally homogenous waveguide (based on the Kuperman-Ingenito noise model[18]) was constructed with a 32-element array of the same inter-element spacing as the previous section and sampling frequency 12 kHz. The array was situated with the lowest element at 70 m depth with reflecting layers at 120 m depth (the sediment layer) and at 122 m depth (the bottom). The sound speeds of the three layers were 1500, 1550 and 1580 m/s. The conventional and MVDR fathometer responses were computed using simulated CSDMs for all frequency bins from 10–4167 Hz of 4096-point Fourier transforms.

The results are shown in Fig. 4.8. The prominent features are the peaks in the sensor noise region [Fig. 4.8(a) and (c), equivalent to T_2 and T_3 from the

1D model, Eq. (4.13)], the reflection peaks at 50 and 52 m [Fig. 4.8(a) and (b), T_1 from Eq. (4.13)] and the reflection off the ocean surface at -70 ± 2 m [Fig. 4.8(a) and (d)]. This is consistent with two signals reflecting off the sediment with a relative time-delay corresponding to a 2 m propagation distance. Both reflect off the surface such that a correlation of the signals yields four correlation peaks with two at the same location. Hence the central peak is twice the height of the adjacent peaks as shown [Fig. 4.8(d)]. This term follows from Eq. (4.37) in App. 4.A, but not from Eq. (4.13) which did not include surface reflections. T_4, which is subject to less array gain than any of the other terms, is not visible in Fig. 4.8.

There is a close correspondence between the prominent features in this simulation (which includes signal from an infinite surface sheet) and Eq. (4.15) (which assumed only a small patch of surface directly above the array). This correspondence suggests, subject to appropriate array geometries and processing bandwidths, the approximation that vertically propagating noise is the dominant contribution is valid. While a detailed description of what geometries and bandwidths are required to validate this model is beyond the scope of this paper, the effect of bandwidth on the simulated response is considered in the next section.

Exceeding the design frequency

The resolution that can be obtained by the fathometer is determined by the bandwidth used in the processing. However, as the array design frequency is exceeded, signals propagating in non-vertical directions alias into the beams steered to isolate vertically propagating noise. At frequency f any signal incident on the array at an angle

$$\phi_a = \pm \arcsin\left(1 + \frac{nc}{fd}\right) \tag{4.26}$$

will be added in phase and is thus subject to the same array gain as the vertically propagating noise. n is an integer value. As such, the fathometer response computed with frequencies above the design frequency will contain components from sound propagating in non-vertical directions. However, each frequency will contain energy aliased from a different angle of incidence. Integrating over a large bandwidth therefore results in the addition of many alias terms with different phases.

These terms interfere and attenuate relative to the reflection peak, which is added in phase. Previous work has suggested that the ocean bottom reflection peak can be extracted when frequencies up to about twice the design frequency are used[11].

To investigate the relationship between aliasing and the fathometer response, the simulated data were down-sampled spatially to yield a sub-array containing every third element (10-elements with 0.54 m spacing and design frequency 1389 Hz). The fathometer response was constructed with a range of bandwidths with MVDR [Fig. 4.9(b)] passive fathometer processing. The minimum frequency used was 10 Hz and the upper frequency bound was varied from 100–6000 Hz.

The critical angle of the bottom θ_c is $\arccos(1500/1580) = 18.3°$. The surface sources produce sound propagating in all directions of which sound propagating at angles shallower than the critical angle experiences little attenuation. This implies that there is a discontinuity in the angular distribution of incident energy with more acoustic energy incident at angles shallower than θ_c than at steeper angles. As discussed in App. 4.B, the stationary phase approximation is only valid for continuous noise distributions, and the presence of this discontinuity introduces spurious peaks in the passive fathometer response [Eq. (4.45)]. These peaks are due to energy incident at θ_c and alias into the vertical beams at 2200 Hz [Fig. 4.9(a)]. When this frequency is included in the processing the ocean bottom reflection peak is obscured [Fig. 4.9(b)]. Rearranging Eq. (4.26) gives this frequency as

$$f_{max} = \frac{2f_d}{(1+\sin\theta_c)} \quad . \tag{4.27}$$

A harder seafloor will have a larger critical angle and is thus limited to a lower bandwidth, as shown in Fig. 4.9(c) which was computed with the same processing as the previous example but with a sediment sound speed of 2000 m/s and a seabed soundspeed of 2030 m/s (critical angle of 42.3°). In this case, noise propagating at the critical angle aliases into the vertical beams at a frequency of 1670 Hz. At ∼1800 Hz the reflection peak is obscured.

Use of vertical velocity sensors rather than pressure sensors makes the array more sensitive to vertically propagating energy, and previous work has shown that a single vertical velocity sensor can extract the bottom reflection from ambient

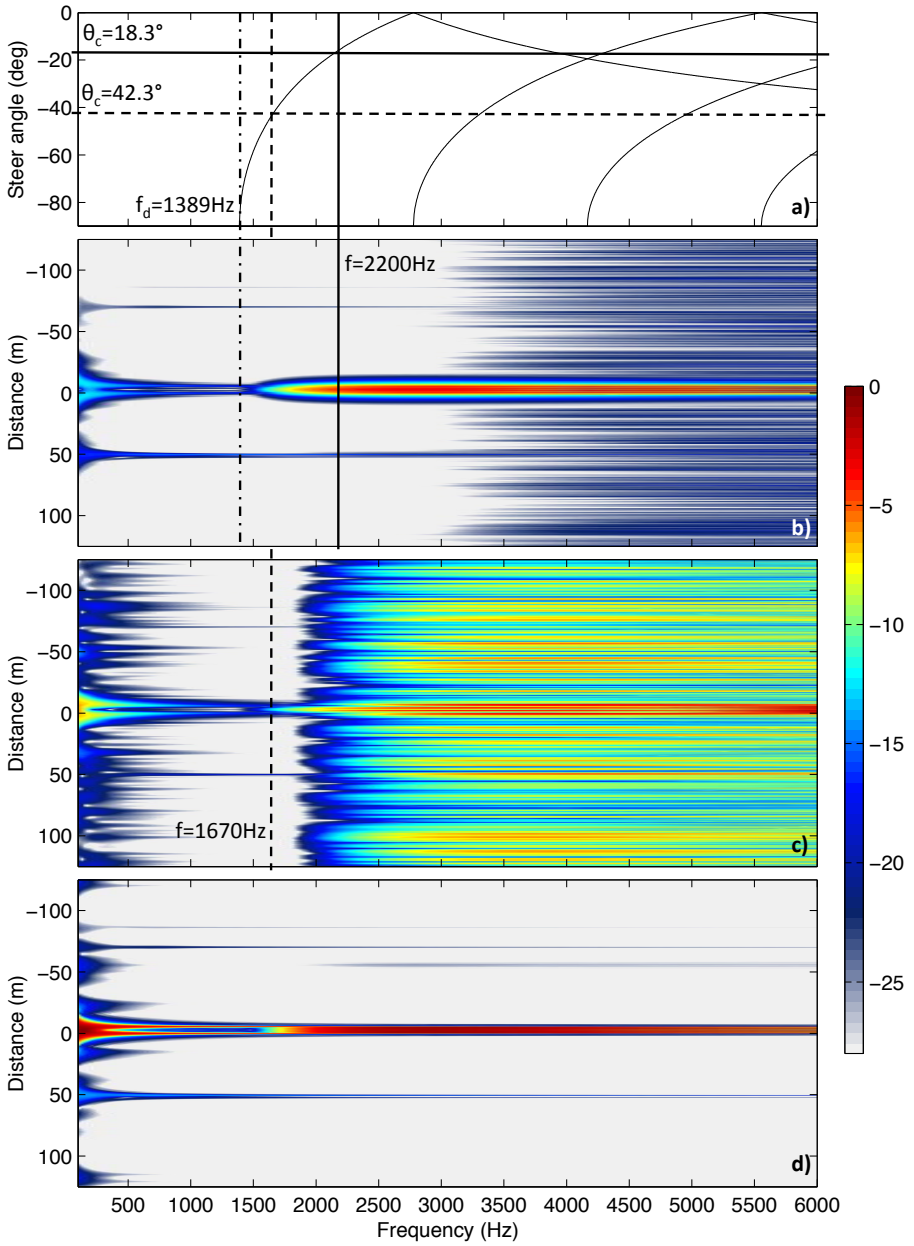

Figure 4.9: (Color online) (a) Alias structure of the downsampled array (f_d = 1389 Hz). The critical angle of the simulated seabeds (horizontal lines), the design frequency (vertical dash-dotted) and the frequencies at which significant signals alias into the vertical beams (vertical lines) are shown. The MVDR passive fathometer response computed with a lower frequency limit of 10 Hz and an upper limit shown on the horizontal axis is shown for (b) a bottom speed of 1580 m/s ($\theta_c = 18.3°$), (c) a bottom speed of 2030 m/s ($\theta_c = 42.3°$), and (d) a bottom speed of 1580 m/s and an array of vertical velocity sensors.

noise[11]. Replacing the hydrophones in the low bottom-speed environment with vertical velocity sensors shows that the effect of the horizontal noise is significantly attenuated [Fig. 4.9(d)]. This extends the upper frequency boundary to beyond 6000 Hz (4.3 times the design frequency) allowing for a greater resolution. In this case the diagonal elements of the CSDM were set to zero to alter the dynamic range.

Error terms in the stationary phase approximation

The passive fathometer response in Eq. (4.18) is the leading order asymptotic behavior of an integration over an infinite surface source. Higher order-terms have been neglected thus far but they become significant at low-frequencies and in the presence of spatial discontinuities in the noise field (see App. 4.B). In order to produce significant error terms the discontinuity in the noise field must be sharp relative to the wavelength of the oscillatory term in the integral of Eq. (4.32) and hence these error terms attenuate at high frequencies. The frequency dependence of these error terms is consistent with spurious peaks that appear in the passive fathometer response when only frequencies lower than 500 Hz are used [Fig. 4.9(c)–(d). Although not visible on this colorscale, they are also present in Fig. 4.9(b)].

The effect of these low frequency error terms is shown in Fig. 4.10. The conventional passive fathometer response is obscured when 150–350 Hz signals are processed [Fig. 4.10(a)]. Using the same model and bandwidth but higher frequencies (400–600 Hz) attenuates the spurious contributions [Fig. 4.10(b)]. Using the same frequency bands with increased seabed attenuation, which both decreases the horizontally propagating energy in the waveguide and softens the discontinuity in the noise field, attenuates the error terms [Fig. 4.10(c) and (d)]. MVDR processing is more robust to the influence of these error terms as they are produced, by definition, by non-vertical signals.

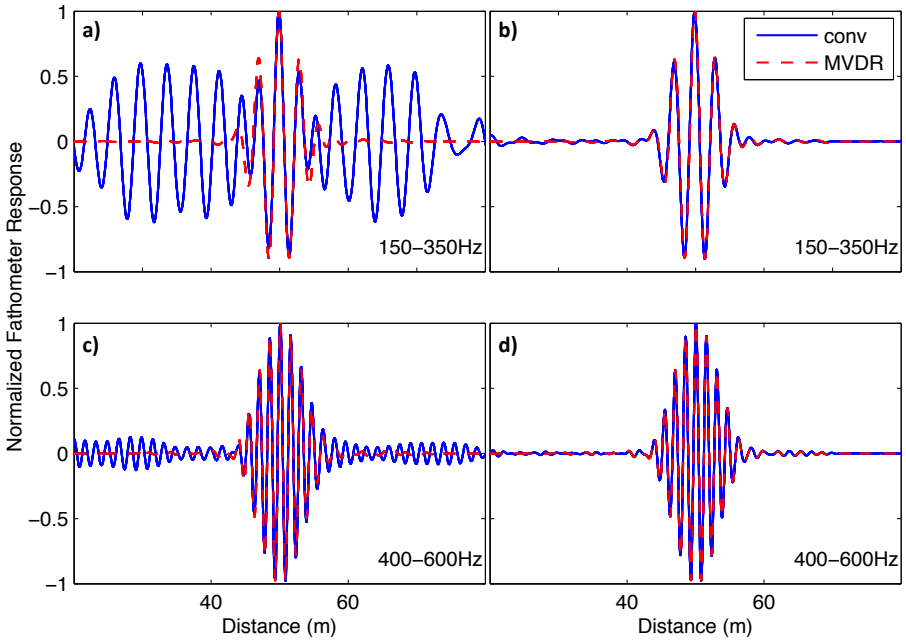

Figure 4.10: (Color online) The simulated passive fathometer response for the full array ($f_d = 4167\,\text{Hz}$) computed with a three layer simulation with sound speeds of 1500, 1550 and 1580 m/s and attenuations of (a and c) 0, 0.06 and 0.2 dB/λ and (b and d) 0, 1.06 and 1.2 dB/λ with (a and b) 150–350 and (c and d) 400–600 Hz. All plots were normalized with respect to the largest peak between 40–60 m. The MVDR trace has been multiplied by -1.

4.4 Conclusion

An analytical fathometer model, verified by numerical simulation, has been presented that describes the asymptotic behavior of the passive fathometer to ambient noise components in a simple waveguide. The leading order term of the surface noise yields the correlation of all possible vertical multipaths. The largest contribution is the correlation of the signal propagating directly from the surface with the signal reflecting from the seabed. This yields the travel-time for sound to propagate from the array to seabed reflecting layers. Vertical noise correlations of other multipaths yield spurious peaks but they are localized and the largest are restricted to negative correlation times.

MVDR processing attenuates the contributions from non-vertical surface noise and discrete noise sources which may obscure the seabed reflection. Contributions from non-vertical surface noise become negligible at high frequencies (shown in App. 4.B and Sec. 4.3.2) and in the presence of weakly reflective seabeds. Discrete noise incident on the array via multipaths generate localized peaks in the positive time-domain of the passive fathometer response (Sec. 4.2.3).

The maximum frequency that can be used while avoiding the application of the array gain to non-vertical signals (i.e. spatial aliasing) is determined by the array geometry and seabed critical angle. In a shallow-water waveguide, there is a discontinuity in the spatial distribution of distant surface noise at the critical angle θ_c which produces error terms in the passive fathometer response. This becomes important when noise incident at θ_c aliases into the vertical beams. Thus the bandwidth available for passive fathometer processing may be increased to include frequencies above the design frequency f_d without inducing substantial errors, providing the maximum frequency processed does not exceed $2f_d/(1+\sin\theta_c)$.

4.A Analytical model of passive fathometer response

Given the vector of data measured by the array, $\mathbf{d}(\omega)$, the cross-spectral density matrix is (see Sec. 5.2)

$$\begin{aligned}
\mathbf{R}(\omega) &= E\left[\mathbf{x}(\omega)\mathbf{x}^H(\omega)\right] \\
&= E\left[\int \mathbf{g(r)} s(r)\, 2\pi r\, dr \int s(r')^* \mathbf{g}(r')^H\, 2\pi r'\, dr'\right] \\
&\quad + E\left[\sum_{j=1}^{J} \mathbf{g}_j n_j n_j^* \mathbf{g}_j^H\right] + E\left[\mathbf{u}\mathbf{u}^H\right] \\
&= |S(\omega)|^2 \int \mathbf{g}\mathbf{g}^H 2\pi r\, dr + \sum_{j=1}^{J} |N_j(\omega)|^2 \mathbf{g}_j \mathbf{g}_j^H + \sigma^2 \mathbf{I} \\
&= \mathbf{R}_c + \mathbf{R}_d + \mathbf{R}_w
\end{aligned} \tag{4.28}$$

where we have defined the white noise component to be $E\left[\mathbf{u}\mathbf{u}^H\right] = \sigma^2\mathbf{I}$. The expectation of the correlation of the surface and discrete noise sources are defined to be $E\left[s(r)s(r')\right] = |S(\omega)|^2\delta(r-r')/(2\pi r)$ and $E\left[n_j n_j\right] = |N_j(\omega)|^2$ respectively. The Dirac-delta function, $\delta(r-r')/(2\pi r)$, results as the surface sources are assumed to be uncorrelated, consistent with previous surface noise models[17]. This allows the integral over r' to be eliminated which makes Eq. (4.28) tractable. $\mathbf{g}_j = \mathbf{g}(r_j, z_j)$ is the vector of Green's functions accounting for the possible multipaths from a source at $r = r_j$ and $z = z_j$ to each array element. Substituting this into Eq. (4.4) gives the fathometer response [Eq. (4.6)].

4.A.1 Discrete noise

Substituting the Green's function between a source at location $\mathbf{r}_j = (r_j, z_j)$ and a receiver at location $\mathbf{r}_p = (r_p, z_p)$ in a uniform waveguide with a single reflecting layer (i.e. the seabed) [Eq. (3) of Ref. [24] and Eq. (4.17) in the text] into the

discrete term of Eq. (4.28) gives the element of $\mathbf{R}_d$ in the pth row and qth column

$$\begin{aligned}[\mathbf{R}_d]_{pq} &= \sum_{j=1}^{J} |N_j(\omega)|^2 g_p(r_j, z_j) g_q(r_j, z_j)^* \\ &= \sum_{j=1}^{J} |N_j(\omega)|^2 \sum_{\alpha,\beta}^{\infty} \frac{\Gamma^{b_\alpha + b_\beta}}{(4\pi)^2 L_\alpha L_\beta} e^{\imath \frac{\omega}{c} L_\Delta} \end{aligned} \tag{4.29}$$

where $L_\Delta = L_\alpha - L_\beta$ and the path-length $L_\alpha = \sqrt{r_j^2 + (2b_\alpha \Delta \pm z_p \pm z_j)^2}$. Applying the steering vectors, the contribution to the fathometer response from the discrete noise is given by

$$\begin{aligned} C_d(\omega) &= \mathbf{w}^T \mathbf{R}_d \mathbf{w} \\ &= \sum_{j=1}^{J} \sum_{p,q=1}^{m} \sum_{\alpha,\beta}^{\infty} |N_j(\omega)|^2 \frac{\Gamma^{b_\alpha + b_\beta}}{(4\pi)^2 L_\alpha L_\beta} \psi^{(p+q-2)+\frac{L_\Delta}{d}} \qquad (4.30) \\ &= \sum_{j=1}^{J} \sum_{p,q=1}^{m} \sum_{\alpha,\beta} B(j,p,q,\alpha,\beta) \psi^{\mu(j,p,q,\alpha,\beta)} \quad , \qquad (4.31) \end{aligned}$$

which describes a set of delta functions in the time-domain with amplitude $B = |N_j(\omega)|^2 \frac{\Gamma^{b_\alpha + b_\beta}}{(4\pi)^2 L_\alpha L_\beta}$ at location $-\mu\tau = -(p+q-2)\tau - \frac{L_\Delta}{c}$.

4.A.2 Correlated noise

The analysis of the correlated noise component is similar to that of the discrete noise component, but the summation over sources is now replaced by an integral over an infinite sheet. Substituting Eq. (4.17) into the correlated term of Eq. (4.28) gives the elements of the CSDM due to the correlated noise component as

$$[\mathbf{R}_c]_{pq} = \frac{|S(\omega)|^2}{(4\pi)^2} \sum_{\alpha,\beta}^{\infty} \Gamma^{b_\alpha + b_\beta} \int_{r=0}^{\infty} \frac{e^{\imath k L_\Delta}}{L_\alpha L_\beta} \, 2\pi r \, dr \tag{4.32}$$

where the path length is $L_\alpha = \sqrt{r^2 + (2b_\alpha \Delta \pm z_p)^2}$.

The integral in Eq. (4.32) is evaluated by stationary phase approximation, in which the integral $\int e^{\imath k f(r)} 2\pi r \, dr$ is assumed to be dominated by contributions near the stationary point of $f(r)$[30]. This interference is more pronounced with a

large value of k and thus this approximation becomes more accurate with increasing frequency. Using $f = L_\Delta$ gives

$$\frac{df}{dr} = r\left(\frac{1}{L_\alpha} - \frac{1}{L_\beta}\right), \quad \frac{d^2 f}{dr^2} = \frac{1}{L_\alpha} - \frac{1}{L_\beta} - \frac{r}{L_\alpha^3} + \frac{r}{L_\beta^3} \quad . \tag{4.33}$$

Eq. (4.33) shows there is one stationary point at $r = 0$. Assuming $p \neq q$ and substituting the first two non-zero terms of the Taylor expansion of f around $r = 0$ in Eq. (4.32) gives,

$$[\mathbf{R}_c]_{pq} = \frac{|S(\omega)|^2}{(4\pi)^2} \sum_{\alpha,\beta} \Gamma^{b_\alpha + b_\beta} \frac{e^{\imath k(\tilde{z}_\alpha - \tilde{z}_\beta)}}{\tilde{z}_\alpha \tilde{z}_\beta} \int_{r=0}^{\infty} e^{\imath k \frac{r^2}{2} \Theta} \, 2\pi r \, dr \tag{4.34}$$

where the following substitutions have been made;

$$\begin{aligned} f(r=0) &= L_\alpha(r=0) - L_\beta(r=0) \\ &= (2b_\alpha \Delta \pm z_p) - (2b_\beta \Delta \pm z_q) = \tilde{z}_\alpha - \tilde{z}_\beta \qquad (4.35) \\ \left.\frac{d^2 f}{dr^2}\right|_{r=0} &= \frac{1}{\tilde{z}_\alpha} - \frac{1}{\tilde{z}_\beta} = \Theta \quad . \qquad (4.36) \end{aligned}$$

Making the substitution $u = re^{\imath\pi/4}\sqrt{k\Theta/2}$ gives

$$[\mathbf{R}_c]_{pq} = \frac{-\imath |S(\omega)|^2}{8\pi k} \sum_{\alpha,\beta} \Gamma^{b_\alpha + b_\beta} \frac{e^{\imath k(\tilde{z}_\alpha - \tilde{z}_\beta)}}{\tilde{z}_\alpha - \tilde{z}_\beta} \quad . \tag{4.37}$$

For simplicity, we assume no surface bounce occurs (α can take one of only two values: $\alpha = 0$ denotes the direct path from surface to the pth element and $\alpha = 1$ denotes a single bottom bounce) which implies

$$\begin{aligned} \tilde{z}_0 - \tilde{z}_0 &= z_q - z_p = (q-p)d \\ \tilde{z}_0 - \tilde{z}_1 &= z_p - (2\Delta - z_q) = -(\tilde{z}_1 - \tilde{z}_0) \\ \tilde{z}_1 - \tilde{z}_1 &= (2\Delta - z_p) - (2\Delta - z_q) = (q-p)d \qquad (4.38) \end{aligned}$$

where the constraint of no surface bounce reduces the $\pm z_p$ term in $\tilde{z}_\alpha$ to $-z_p$.

Substituting $z_p = z_a - (p-1)d$ and $\xi_0 = 2(\Delta - z_a)$, Eq. (4.37) then becomes

$$\begin{aligned}[\mathbf{R}_c]_{pq} &= \frac{-\imath c|S(\omega)|^2}{8\pi\omega}\Big[(1+\Gamma^2)\frac{\psi^{q-p}}{(q-p)d} \\ &\quad +\Gamma\frac{\psi^{-(p+q-2)-\xi_0/d}+\psi^{(p+q-2)+\xi_0/d}}{\xi_0+(p+q-2)d}\Big] \;\forall\, p\neq q \quad .\end{aligned} \tag{4.39}$$

Applying the steering vectors gives Eq. (4.18).

4.B Error terms in the stationary phase approximation

4.B.1 Frequency-dependent error terms

We are concerned with integrals of the general form

$$I = \int_{r=a}^{b} F(r)e^{\imath k f(r)}\,dr \tag{4.40}$$

$$= \int_{r=a}^{b} \frac{F}{\imath k\frac{df}{dr}}\frac{d}{dr}\left(e^{\imath k f}\right)\,dr$$

$$= \frac{F}{\imath k\frac{df}{dr}}e^{\imath k f}\Big|_{r=a}^{b} - \frac{1}{\imath k}\int_{r=a}^{b}\frac{d}{dr}\left(\frac{F}{\frac{df}{dr}}\right)e^{\imath k f}dr \tag{4.41}$$

where we have integrated by parts. Note that the same integration by parts can be repeated ad infinitum, as the integral in Eq. (4.41) is of the same form as that in Eq. (4.40). This yields an infinite series expansion of I. Each successive integration brings another factor of $1/(\imath k)$ and thus at high frequencies the behavior of I is dominated by the first term.

It is the behavior of the leading order term of I, with limits $a = 0$ and $b = \infty$, that was derived in App. 4.A and yields the depth of the seabed reflecting layers. Contributions from higher-order terms in the expansion, although not evaluated explicitly here, become increasingly significant at low frequencies. These terms may be the cause of the spurious peaks in the fathometer response at low frequencies as shown by simulation in Sec. 4.3.2.

4.B.2 Effect of seabed critical angle

In the previous use of the stationary phase approximations the seabed reflection coefficient, Γ was assumed independent of grazing angle. This is clearly not the case, as for rays incident on the seabed at angles shallower than the critical angle, the reflection coefficient is one. Here we consider a fathometer model where the reflection coefficient varies as a step function such that

$$\Gamma_\alpha(r) = \begin{cases} \gamma & \theta < \theta_c \\ 1 & \theta \geq \theta_c \end{cases} \tag{4.42}$$

where $\gamma < 1$ is a constant. As the stationary phase approximation used in App. 4.A is only valid for continuous functions, Eq. 4.39 is not correct for this case. Defining $\epsilon_\alpha = (2b_\alpha\Delta \pm z_a)/\tan\theta_c$ as the radial distance from the array at which rays from the α path are incident upon the ocean bottom at the critical angle θ_c and experience no attenuation from bottom loss, Eq. (4.32) becomes

$$\begin{aligned} [\mathbf{R}_c]_{pq} &= \frac{|S(\omega)|^2}{(4\pi)^2} \sum_{\alpha,\beta} \left[\gamma^{b_\alpha + b_\beta} \int_{r=0}^{\epsilon_\alpha} \frac{e^{\imath k(L_\alpha - L_\beta)}}{L_\alpha L_\beta} \, 2\pi r \, dr \right. \\ &\quad + \gamma^{b_\beta} \int_{r=\epsilon_\alpha}^{\epsilon_\beta} \frac{e^{\imath k(L_\alpha - L_\beta)}}{L_\alpha L_\beta} \, 2\pi r \, dr \\ &\quad \left. + \int_{r=\epsilon_\beta}^{\infty} \frac{e^{\imath k(L_\alpha - L_\beta)}}{L_\alpha L_\beta} \, 2\pi r \, dr \right] \end{aligned} \tag{4.43}$$

where $\epsilon_\beta > \epsilon_\alpha$.

The first term can be evaluated as in App. 4.A and yields the same result [Eq. (4.37)]. The other two terms cannot be evaluated by the stationary phase approximation as they have no stationary points within the limits of integration [conversely, the first term cannot be evaluated by the following method as the stationary point produces an infinite term when the limit $r = 0$ is substituted into Eq. (4.41)].

Substituting $F = 2\pi r/(L_\alpha L_\beta)$ and $f = L_\Delta$ and into the leading order term of Eq. 4.41 yields

$$\begin{aligned} I &\approx \frac{2\pi}{\imath k(L_\beta - L_\alpha)} e^{\imath k L_\Delta} \Big|_{r=a}^{b} \\ &= \frac{2\pi}{\imath k} \left[\frac{e^{\imath k L_\Delta(a)}}{L_\Delta(a)} - \frac{e^{\imath k L_\Delta(b)}}{L_\Delta(b)} \right] \quad . \end{aligned} \tag{4.44}$$

Substituting this into Eq. (4.43) with the appropriate limits of integration yields

$$[\mathbf{R}_c]_{pq} = \frac{-\imath|S(\omega)|^2}{8\pi k}\sum_{\alpha,\beta}\left[\gamma^{b_\alpha+b_\beta}\frac{e^{\imath k(\tilde{z}_\alpha-\tilde{z}_\beta)}}{\tilde{z}_\alpha-\tilde{z}_\beta} + \gamma^{b_\beta}\frac{e^{\imath k L_\Delta(\epsilon_\alpha)}}{L_\Delta(\epsilon_\alpha)} + (1-\gamma^{b_\beta})\frac{e^{\imath k L_\Delta(\epsilon_\beta)}}{L_\Delta(\epsilon_\beta)}\right] . \quad (4.45)$$

The second and third terms are error terms introduced by discontinuities in the noise field at the critical angle. Such discontinuities might be expected in a waveguide with low attenuation in the seabed and low scattering. If $\Gamma_\alpha(r)$ is not infinitely discontinuous, at high enough frequencies the wavelength of the oscillatory function $e^{\imath k(L_\alpha-L_\beta)}$ at $r=\epsilon$ is small enough that $\Gamma_\alpha(r)$ appears continuous and these error terms attenuate. Thus these error terms attenuate at high frequencies. As these terms are due to energy incident at the critical angle, their contribution to the passive fathometer response may be attenuated by use of MVDR steering vectors which more effectively excludes non-vertical noise.

Increased attenuation in the seabed will reduce the discontinuity in the spatial distribution of incident noise and may decrease the effect of these terms.

4.B.3 Moving sources

Data must be averaged over a finite amount of time in order to approximate the CSDM [Eq. (5)]. A discrete source that moves from $\mathbf{r}_1$ to $\mathbf{r}_2$ during this integration time will produce a similar effect on the CSDM [Eq. (4.29)] as a spatially distributed source that varies continuously between $\mathbf{r}_1$ and $\mathbf{r}_2$ and is zero elsewhere,

$$[\mathbf{R}_d]_{pq} = \frac{|N(\omega)|^2}{|\mathbf{r}_1-\mathbf{r}_0|}\sum_{\alpha,\beta}^{\infty}\frac{\Gamma^{b_\alpha+b_\beta}}{(4\pi)^2}\int_{\mathbf{r}_0}^{\mathbf{r}_1}\frac{e^{\imath\frac{\omega}{c}L_\Delta}}{L_\alpha L_\beta}\,d\mathbf{r} \quad . \quad (4.46)$$

For any given combination of paths α and β this gives an integral of the form in Eq. (4.44), which yields

$$[\mathbf{R}_d]_{pq} = \frac{-\imath|N(\omega)|^2}{8\pi k|\mathbf{r}_1-\mathbf{r}_0|}\sum_{\alpha,\beta}^{\infty}\Gamma^{b_\alpha+b_\beta}\left(\frac{e^{\imath\frac{\omega}{c}L_{\Delta(\mathbf{r}_0)}}}{L_{\Delta(\mathbf{r}_0)}}+\frac{e^{\imath\frac{\omega}{c}L_{\Delta(\mathbf{r}_1)}}}{L_{\Delta(\mathbf{r}_1)}}\right) \quad . \quad (4.47)$$

This is similar to the contribution produced by stationary sources [Eq. 4.29] but is scaled by the $1/(k|\mathbf{r}_1 - \mathbf{r}_0|)$ and thus the maximum contribution would be expected from stationary sources.

4.3 Acknowledgements

This chapter is a reprint of the material as it appears in the Journal of the Acoustical Society of America 2011. Traer, James; Gerstoft, Peter; Hodgekiss, William S., Acoustical Society of America, 2011. The dissertation author was the primary investigator and author of this paper.

This work was supported by the Office of Naval Research under grants N00014-05-1-0264 and N00014-08-1-0196.

Bibliography

[1] J. Rickett and J. Claerbout, "Acoustic daylight imaging via spectral factorization: Helioseismology and reservoir monitoring," The Leading Edge **18**, 957–960 (1999).

[2] R. L. Weaver and O. I. Lobkis, "Ultrasonics without a source: Thermal fluctuation correlations at MHz frequencies," Phys. Rev. Lett. **87**, 134301 (2001).

[3] P. Roux and W. A. Kuperman, "Extracting coherent wave fronts from acoustic ambient noise in the ocean," J. Acoust. Soc. Am. **116**, 1995–2005 (2004).

[4] P. Roux, K. G. Sabra, W. A. Kuperman and A. Roux, "Ambient noise cross-correlation in free space: Theoretical approach," J. Acoust. Soc. Am. **117**, 79–84 (2005).

[5] O. A. Godin, "Recovering the acoustic Green's function from ambient noise cross-correlation in an inhomogeneous moving medium," Phys. Rev. Lett. **97**, 053401 (2006), DOI:10.1103/PhysRevLett.97.054301.

[6] L. A. Brooks and P. Gerstoft, "Green's function approximation from cross-correlations of 20–100 Hz noise during a tropical storm," J. Acoust. Soc. Am. **125**, 723–734 (2009).

[7] M. J. Buckingham and S. A. S. Jones, "A new shallow-ocean technique for determining the critical angle of the seabed from the vertical directionality

of the ambient noise in the water column," J. Acoust. Soc. Am. **81**, 938–946 (1987).

[8] N. M. Carbone, G. B. Deane and M. J. Buckingham, "Estimating the compressional and shear wave speeds of a shallow water seabed from the vertical coherence of ambient noise in the water column," J. Acoust. Soc. Am. **103**, 801–813 (1998).

[9] C. H. Harrison and D. G. Simons, "Geoacoustic inversion of ambient noise: A simple method," J. Acoust. Soc. Am. **112**, 1377–1389 (2002).

[10] M. Siderius, C. H. Harrison and M. B. Porter, "A passive fathometer technique for imaging seabed layering using ambient noise," J. Acoust. Soc. Am. **120**, 1315–1323 (2006).

[11] P. Gerstoft, W. S. Hodgkiss, M. Siderius, C. F. Huang, and C. H. Harrison, "Passive fathometer processing," J. Acoust. Soc. Am. **123**, 1297–1305 (2008).

[12] C. H. Harrison and M. Siderius, "Bottom profiling by correlating beam-steered noise sequences," J. Acoust. Soc. Am. **123**, 1282–1296 (2008).

[13] C. H. Harrison, "Anomalous signed passive fathometer impulse response when using adaptive beam forming," J. Acoust. Soc. Am. **125**, 3511–3513 (2009).

[14] J. Traer, P. Gerstoft, H. C. Song and W. S. Hodgkiss, "On the sign of the adaptive passive fathometer impulse response," J. Acoust. Soc. Am. **126**, 1657–1658 (2009).

[15] M. Siderius, H. C. Song, P. Gerstoft, W. S. Hodgkiss and C. H. Harrison, "Adaptive passive fathometer processing," J. Acoust. Soc. Am. **127**, 2193–2200 (2010).

[16] S. L. Means and M. Siderius, "Effects of sea-surface conditions on passive fathometry and bottom characterization," J. Acoust. Soc. Am. **126**, 2234–2241 (2009).

[17] B. F. Cron and C. H. Sherman, "Spatial Correlation Functions for Various Noise Models," J. Acoust. Soc. Am. **34**, 1732–1236 (1962).

[18] W. A. Kuperman and F. Ingenito, "Spatial correlation of surface generated noise in a stratified ocean," J. Acoust. Soc. Am. **67**, 1988–1996 (1980).

[19] C. H. Harrison, "Formulas for ambient noise level and coherence," J. Acoust. Soc. Am. **99**, 2055–2066 (1996).

[20] C. H. Harrison, "Performance and limitations of spectral factorization for ambient noise sub-bottom profiling," J. Acoust. Soc. Am. **118**, 2913–2923 (2005).

[21] A. B. Baggeroer, W. A. Kuperman and H. Schmidt, "Matched field processing: Source localization in correlated noise as an optimum parameter estimation problem," J. Acoust. Soc. Am. **83**, 571–587 (1988).

[22] H. Nakahara, "A systematic study of theoretical relations between spatial correlation and Green's function in one-, two- and three-dimensional random scalar wavefields," Geophys. J. Int. **167**, 1097–1105 (2006).

[23] R. Snieder, K. Wapenaar and K. Larner, "Spurious multiples in seismic interferometry of primaries," Geophys. **71**, Sl111–Sl124 (2006).

[24] L. A. Brooks and P. Gerstoft, "Ocean acoustic interferometry," J. Acoust. Soc. Am. **121**, 3377–3385 (2007).

[25] Van Trees, H. L., *Optimum array processing*, (Wiley, New York, 2002), Chap. 2.

[26] K. G. Sabra, P. Roux and W. A. Kuperman, "Arrival-time structure of the time-averaged ambient noise cross-correlation function in an oceanic waveguide," J. Acoust. Soc. Am. **117**, 164–174 (2005).

[27] Van Trees, H. L., *Optimum array processing*, (Wiley, New York, 2002), Chap. 6.

[28] Jensen, F. B., Kuperman, W. A., Porter, M. B., and Schmidt, H., *Computational Ocean Acoustics*, (Springer-Verlag, New York, 2000), Chap. 2.

[29] Schmidt, H., *OASES Version 3.1 User Guide and Reference Manual*, (MIT, Cambridge, 2004).

[30] Bender, C. M. and Orszag, S. A., *Advanced mathematical methods for scientists and engineers: Asymptotic methods and perturbation theory*, (McGraw-Hill, New York, 1978), Chap. 6.

Chapter 5

Coherent averaging of the passive fathometer response using short correlation time

The passive fathometer algorithm was applied to data from two drifting array experiments in the Mediterranean, Boundary 2003 and 2004. The passive fathometer response was computed with correlation times from 0.34–90 s and, for correlation times less than a few seconds the observed Signal-to-Noise Ratio (SNR) agrees with a 1D model of SNR of the passive fathometer response in an ideal waveguide. In the 2004 experiment, the fathometer response showed the array depth varied periodically with an amplitude of 1 m and a period of 7 s consistent with wave driven motion of the array. This introduced a destructive interference which prevents the SNR growing with increasing correlation time. A peak tracking algorithm applied to the fathometer response of experimental data was used to remove this motion allowing the coherent passive fathometer response to be averaged over several minutes without destructive interference. Multirate adaptive beamforming, using 90 s correlation time to form adaptive steer vectors which were applied to 0.34 s data snapshots, increases the SNR of the passive fathometer response.

5.1 Introduction

The passive fathometer, which extracts the seabed impulse response from cross-correlation of ambient noise data from a drifting vertical array, has been the subject of much discussion in recent years. Theoretical models have been presented[1, 3, 2, 4, 5, 6, 7] and the seabed impulse response has been extracted from experimental data[1, 3, 2, 8, 9]. The technique relies on surface generated noise from wind and waves[10, 11]. Shipping noise disrupts the technique but this interference can be minimized with use of adaptive beamforming techniques[9, 7].

Most work to date has focused on measuring the depth of reflecting layers. Inference of the seabed reflection coefficient from ambient noise processing would greatly improve the scope of geo-acoustic inversion with the passive fathometer as it has been demonstrated that properties of the seabed are inter-related[12] and inference of the reflection coefficient would yield the seabed density, porosity, wave-speed and attenuation for compression and shear waves. Interpretation of the peak heights of the passive fathometer response requires an understanding of the factors that effect the peak height. Two factors are considered here: the correlation time and processing bandwidth.

Prior theories of the passive fathometer have assumed infinite correlation time[1, 3, 2, 4, 5, 6, 7] and prior experimental work has used 10s of seconds to minutes of data for an individual snapshot of the seabed[8, 9]. Other applications of ambient noise correlation in the ocean have used 10's of minutes to a day[13, 14] of data. However the ocean is a dynamic environment and both the sound field and environment may vary on the scale of seconds. In the presence of tropical storm generated noise, which is high amplitude and ideal for ambient noise processing, correlation peaks have been obtained with as little as 20 s [15]. Work with active sources suggests that increased temporal resolution can be obtained by processing a large bandwidth[16].

Green's function extraction from ambient noise cross-correlation, the basic technique that underlies the passive fathometer, has an extensive published literature, well summarized in Ref. [17], and has been utilized in helioseismology[18], ultrasonics[19], seismics[20, 21, 22], ocean acoustics[13, 14]. Theoretical models

of the amplitude of correlation peaks as a function of correlation time have been presented[23, 24] but the results are very general and not readily applicable to the passive fathometer.

The goal of this work is two-fold: (1) To present a simple and idealized model of correlation peak SNR in a model tailored to the passive fathometer. The variation of SNR with correlation time and processing bandwidth are considered theoretically for a 1D environment. (2) To show, with experimental data from the Boundary 2003 and 2004 experiments[25], that seabed profiling with the passive fathometer can be performed with less than a second of data. Not only are such short correlation times possible, but with large surface waves, they are necessary to extract the seabed impulse response as destructive interference is introduced by wave-driven motion of the array. Using multi-rate beamforming[26], long time averages are used to compute Minimum Variance Distortionless Response (MVDR) steering vectors which are applied to short time Cross-Spectral Density Matrix (CSDM) snapshots, allowing MVDR processing to be conducted with high temporal resolution.

5.2 Theory

Consider a sensor pair with sensor 2 placed d vertically above sensor 1 which is placed $\xi/2$ above the seabed with vertical reflection coefficient r_0. The noise field incident upon the sensor pair $S(t)$ is assumed delta correlated in time similar to prior models[27, 28]. Assume the sensors have sampling frequency f_s and the data is pass-band filtered with a bandwidth of B.

In 1D the cross-correlation of the signal at the two sensors gives a peak at the inter-element travel time d/c (App. 5.A)

$$\begin{aligned} \left\langle C^{1D}(\tau) \right\rangle &= \frac{1}{T}\int_0^T \langle x_1(t)x_2(t+\tau)\rangle \, dt \\ &= \sigma_0^2 \left[\Delta\!\left(\tau + \frac{d}{c}\right) + r_0 \Delta\!\left(\tau \pm \frac{\xi - d}{c}\right)\right] , \end{aligned} \tag{5.1}$$

where σ_0^2 is the variance of the signal $S(0,t)$ and $\Delta(\tau)$ is the Dirac measure, which is a peak at $\tau = 0$ with a height of 1 and a width of $1/f_s$. A peak at $\tau = d/c$ with

amplitude r_0^2 has been neglected. The location of the peak at $(\xi + d)/c$ gives the depth of the seabed reflecting layer.

5.2.1 Fathometer Processing

The passive fathometer employs a vertical array of m sensors, which are assumed here to be equispaced by d. The correlation of each pairing of sensors $C_{j,k}(\tau)$ is of the form of Eq. (5.1) with a δ-function at $\tau = (\xi_k + (k-j)d)/c$ where ξ_k is the distance from the kth sensor to the seabed. Summing all pairs with time delays such that the seabed reflection peak is at $\tau = \xi_0$, the fathometer response for positive times ($\tau > 0$) is[1, 3, 6, 7]

$$\begin{aligned} F^{1D}(\tau) &= \sum_{j=1}^{m}\sum_{k=1}^{m} \left\langle C_{j,k}^{1D}\left[\tau - (\xi_m - \xi_k - (k-j)d)\right]\right\rangle \\ F^{1D} &= m^2 r_0 \sigma_0^2 \Delta(\tau - \xi_0/c) \ . \end{aligned} \tag{5.2}$$

In the frequency domain, a time-delay of $\Delta_{j,k}$ is implemented by multiplying the correlation $C_{j,k}(\omega)$ by an exponential term $e^{\imath\omega\Delta_{j,k}}$ such that the frequency domain fathometer output can be obtained by applying steering vectors $\mathbf{w}$ to the cross-spectral density matrix[3, 6, 7] $\mathbf{R}_{j,k}(\omega) = \langle C_{j,k}(\omega)\rangle$

$$F^{1D}(\omega) = \mathbf{w}^T \mathbf{R}(\omega)\mathbf{w} \tag{5.3}$$

where the steering vector for downward propagating noise is given by

$$\mathbf{w} = (e^{\imath(m-1)\omega d/c}, e^{\imath(m-2)\omega d/c \ldots e^{\imath 2\omega d/c}}, e^{\imath\omega d/c}, 1)^{\mathrm{T}} \ . \tag{5.4}$$

5.2.2 Signal-to-Noise Ratio

Variance of noise correlation

The noise cross-correlation [Eq. (5.1)] is normalized such that the reflection peak height does not depend on correlation time T however the variance of the correlation, which may obscure this peak, is dependent on correlation time[23, 24].

The correlation variance is (Eq. 5.21)

$$\begin{aligned} \mathrm{Var}\left\{C(\tau)\right\} &= \left\langle C(\tau)^2 \right\rangle - \left\langle C(\tau) \right\rangle^2 \\ &= \frac{\sigma_0^4}{T^2} \int_0^T \int_0^T \Delta(t-t')\,\mathrm{d}t\mathrm{d}t' = \frac{2\sigma_0^4 B}{T f_s^2} \ . \end{aligned} \tag{5.5}$$

The SNR for the seabed reflection is given by dividing the reflection peak amplitude by the standard deviation

$$\mathrm{SNR}_{1D} = r_0 \sqrt{\frac{TB}{2}} \ . \tag{5.6}$$

Using plane wave beamforming and m sensors gives $m(m-1)$ sensor-pair cross-correlations $C_{j,k}(\tau)$ and m autocorrelations $C_{j,j}(\tau)$, which, yields m^2 correlations. Summing over these pairings increases the peak height by m^2 and the variance by m yielding

$$SNR_{1D} = m r_0 \sqrt{\frac{TB}{2}} \ . \tag{5.7}$$

5.2.3 Multi-rate adaptive processing

If the noise field contains discontinuities, due to the presence of discrete sources, such as ships, or the seabed critical angle, spurious peaks are introduced in the passive fathometer response[9, 7]. Minimum-Variance Distortionless Response (MVDR) processing may be more effective at attenuating these spurious contributions than conventional beamforming[3, 9, 7] however it is very susceptible to small errors in the estimation of the noise field. The accuracy of the CSDM estimate can be improved by averaging L independent snapshots of the CSDM ($L > m$ to ensure the CSDM is full-rank), such that

$$\mathbf{Q}_n = \sum_{j=n-L/2}^{n+L/2} \mathbf{R}_j \ . \tag{5.8}$$

This increases the time necessary to produce an estimate of the seabed response. If the array or noise field is non-stationary less correlation time is desirable.

Multi-rate beamforming uses different time averages to produce the MVDR steer vectors and the data CSDM. It was introduced to track a stable signal in the

presence of dynamic interferers[26]. In the case of the passive fathometer, if the array is moving with surface waves, the signal oscillates on the scale of seconds, while interfering noise from distant ships is likely to remain stable over several minutes or more.

At each frequency bin, the data snapshot obtained using a correlation time of T is used to form a rank-1 estimate of the CSDM $\mathbf{R}_j$. A set of L CSDM-snapshots, adjacent in time, is averaged to yield a full-rank matrix $\mathbf{Q}_n$ which is used to compute the MVDR steering vectors steered towards downward and upward propagating noise

$$\begin{aligned} \tilde{\mathbf{w}}_d &= \frac{\mathbf{Q}_n^{-1}\mathbf{w}}{\mathbf{w}^{\mathrm{H}}\mathbf{Q}_n^{-1}\mathbf{w}} \\ \tilde{\mathbf{w}}_u &= \frac{\mathbf{Q}_n^{-1}\mathbf{w}^*}{\mathbf{w}^{\mathrm{T}}\mathbf{Q}_n^{-1}\mathbf{w}^*} \ . \end{aligned} \tag{5.9}$$

The passive fathometer algorithm [Eq. (5.3)] can then be implemented by applying the adaptive steer vectors to the nth CSDM snapshot

$$\tilde{F}(\omega) = \tilde{\mathbf{w}}_u^{\mathrm{H}}\mathbf{R}_n\tilde{\mathbf{w}}_d \ . \tag{5.10}$$

Assuming the interfering noise which the MVDR minimizes is constant over LT the steering vectors can then be calibrated to minimize this, while the signal of interest need only be constant over a time period T.

Use of $\mathbf{Q}_n$ for both computation of the steer vectors and and as the data CSDM yields the usual MVDR fathometer response[3, 4, 5, 9, 7]

$$\tilde{F}(\omega) = \tilde{\mathbf{w}}_u^{\mathrm{H}}\mathbf{Q}_n\tilde{\mathbf{w}}_d \ . \tag{5.11}$$

5.3 Experiment

Data was from the Boundary 2003 and 2004 experiment[25], in which a 32-element array with 0.18 m inter-element spacing (design frequency 4167 Hz) and sampling frequency 12 kHz was set adrift in waters of 120 m depth in the Mediterranean. The array was assumed to remain at a constant depth of 73.5 m thoughout both experiments. Passive fathometry responses from the 2003 data

show MVDR processing allows good extraction of the seabed profile[9]. The 2003 drift was performed on July 22nd and the 2004 drift on May 12.

5.3.1 Overview of data set

The passive fathometer algorithm was performed on CSDMs formed from 90 s averages of 2^{14}-point (1.36 s) snapshots over the entire data sets recorded 23 July 2003 [Fig. 5.1(a)] and 12 May 2004 [Fig. 5.1(b)]. The MVDR passive fathometer output [Fig. 5.1(c)–(d)], spectra [Fig. 5.1(e)–(f)] and MVDR beamforms of data between 1.4–1.6 kHz [Fig. 5.1(g)–(h)] were obtained from the same periods. A 50–4000 Hz passband was used to form the MVDR fathometer response. Due to shipping noise a 200–4000 Hz and a 700–4000 KHz passband were used for the plane-wave fathometer response from the 2003 and 2004 experiments. Fig. 5.1(a) and (c) are identical to Fig. (5)(b) and (c) in Ref. [9].

The passive fathometer response from the 2003 drift shows the seabed and several sub-bottom reflecting layers. The response form the 2004 drift shows only one layer and it is obscured by large amplitude spurious peaks. The spectra [Fig. 5.1(e)–(f)] and beamforms [Fig. 5.1(g)–(h)] show the 2004 data set contains more horizontal interfering noise. However horizontal interfering noise is present at 5.5 h and 11–12 h have a small effect on the passive fathometer response, suggesting the beamforming effectively attenuates these contributions.

The beamform response [Fig. 5.1(g)–(h)] over the whole period shows more energy coming from above the array, consistent with surface generated noise[10, 11]. At times, strong signals are incident on the array from horizontal angles, consistent with distant sources from both shipping and the ocean surface propagating at angles shallower than the critical angle with negligible loss.

Wind measurements made before and during both drift experiments show the wind at the site did not exceed 10 m/s thoughout and for 15 h before the 2003 drift. 12 h before the 2004 drift winds reached a sustained velocity above 25 m/s for 2 h. This suggests that although the acoustic environments were similar for the drifts [Fig. 5.1(e)–(h)] the 2004 experiment had larger surface waves.

Thee 170 s regions from Fig. 5.1, marked I, II and III were examined at

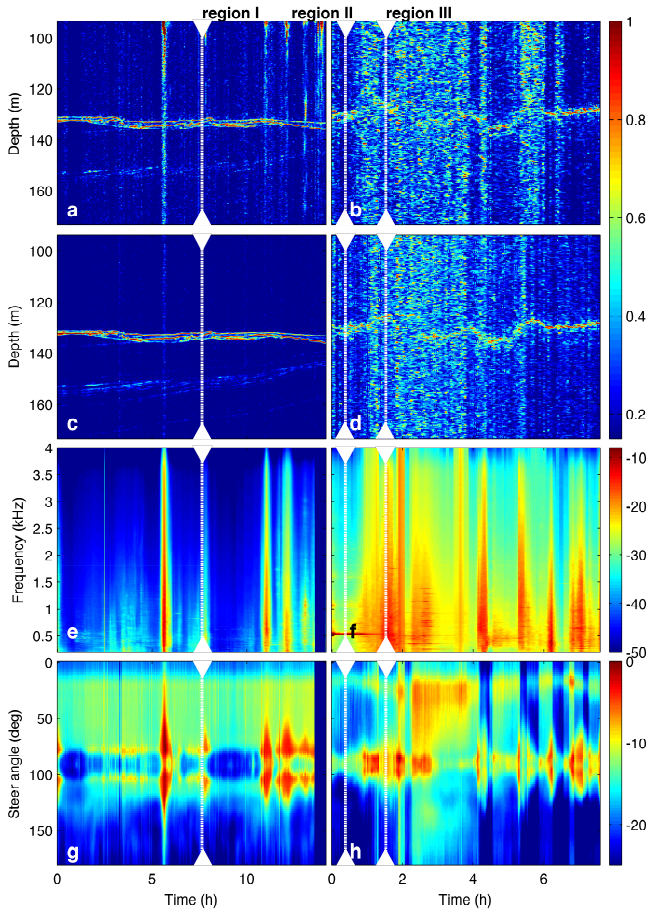

Figure 5.1: (Color online) For the (a,c,e,g) Boundary 2003 and (b,d,f,h) Boundary 2004, the envelope of the passive fathometer response with (a–b) conventional and (b–c) MVDR steering vectors, (e–f) the spectrograms and (g–h) MVDR beamform responses. The dashed lines indicate the sections investigated at high resolution in Sec. 5.3.2.

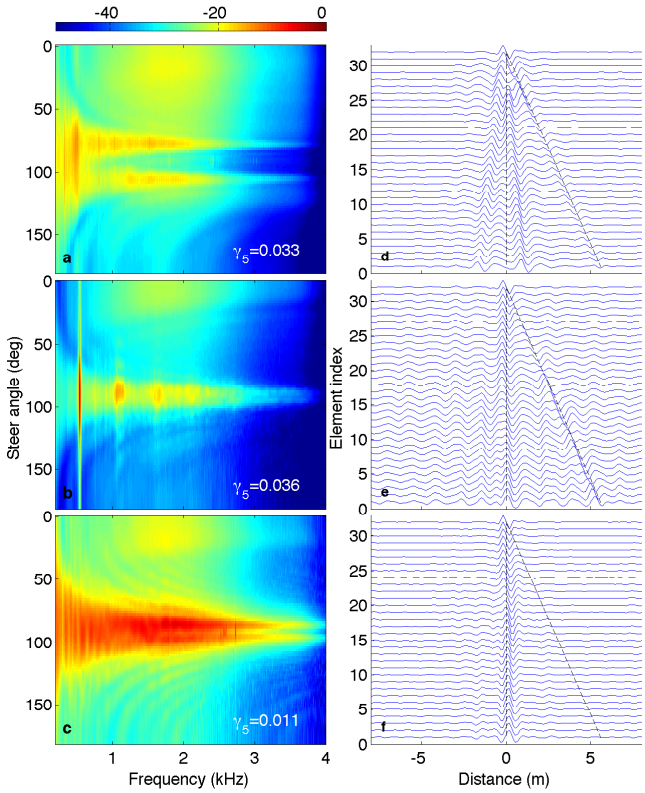

Figure 5.2: (Color online) Beamform response from 170 s of data obtained from regions (a) I, (b) II and (c) III as defined in Fig. 5.1 and (d)–(f) the noise cross-correlation of the each array element with the top element plotted against the travel-distance associated with the correlation time and 1500 m/s soundspeed for the same data sets. For the beamform responses the ratio of power incident on the array from 0–10° and the power incident from all directions γ_5 is shown. The zero offset time and vertically propagating wave are shown (dash lines).

high time resolution (Figs. 5.2–5.7). The data was split into 4096-point (0.34 s) snapshots with 50% overlap, Fourier transformed, and processed to obtain the beamform response, noise cross-correlations between sensor pairs and the fathometer response. Region I was obtained at 2129Z, region II at 1546Z and region III at 1654Z.

The beamform responses [Fig. 5.2(a)–(c)] show an asymmetry with more noise incident on the array from 0° then 180°, consistent with surface generated noise[10]. This asymmetry is manifested in the cross-correlations [Fig. 5.2(d)–(f)] as a peak with location equal to the inter-element separation in the positive domain

only. All regions contain interfering noise incident at 90°. In region I [Fig. 5.2(a)] the noise field contained two sharp peaks at $90 \pm 15°$ possibly due to critical angle reflections. These contributions produce two symmetrical peaks in the 2-element noise cross correlations [Fig. 5.2(d)]. Assuming the array is 50 m above the ocean bed the beamwidth for the noise correlation is 5°. γ_5 is measured as the sum of the beamform output between 0–5° divided by the sum of the total beamform response. Over region 1 $\gamma_5 = 0.033$.

In region II [Fig. 5.2(b) and (e)] the noise field is similar to that in region I with a narrowband interferer at 550 Hz. However despite this interferer, region II has a slightly higher value of γ_5 than region I [Fig. 5.2(a)–(b)], as the two experiments were conducted in similar environments, where r_0 and ξ_0 are similar this suggests the fathometer reflection peaks from these regions will have similar emergence times Over this region $\gamma_5 = 0.036$ which is approximately the same as region I.

Region III [Fig. 5.2(c) and (f)] has a strong horizontal interference which gives a value of $\gamma_5 = 0.011$ which is 1/3 the value in regions I and II and a strong peak at zero-correlation time [Fig. 5.2(f)]. Although the 2-element noise cross-correlations are dominated by the zero offset peak, the up and downgoing waves are still present and with array gain from multiple elements the seabed reflection may still be extracted.

5.3.2 Reflection peak signal-to-noise ratio

The fathometer responses from the 170 s regions shown in Fig. 5.2 were coherently averaged over 2 [Fig. 5.3(a),(c) and (e)] and 10 s [Fig. 5.3(b),(d) and (f)]. For each snapshot the SNR was estimated from the maximum peak height within a 4 m window around the seabed reflection and the standard deviation of the noise outside this window. These values were averaged over all the snapshots to give the estimated SNR of each region.

The response from region I [Fig. 5.3(a)–(b)] shows the seabed reflection peak appears at different depths at different times and is sometimes obscured by noise. This may be due to temporal changes in the noise field, changing characteristics of

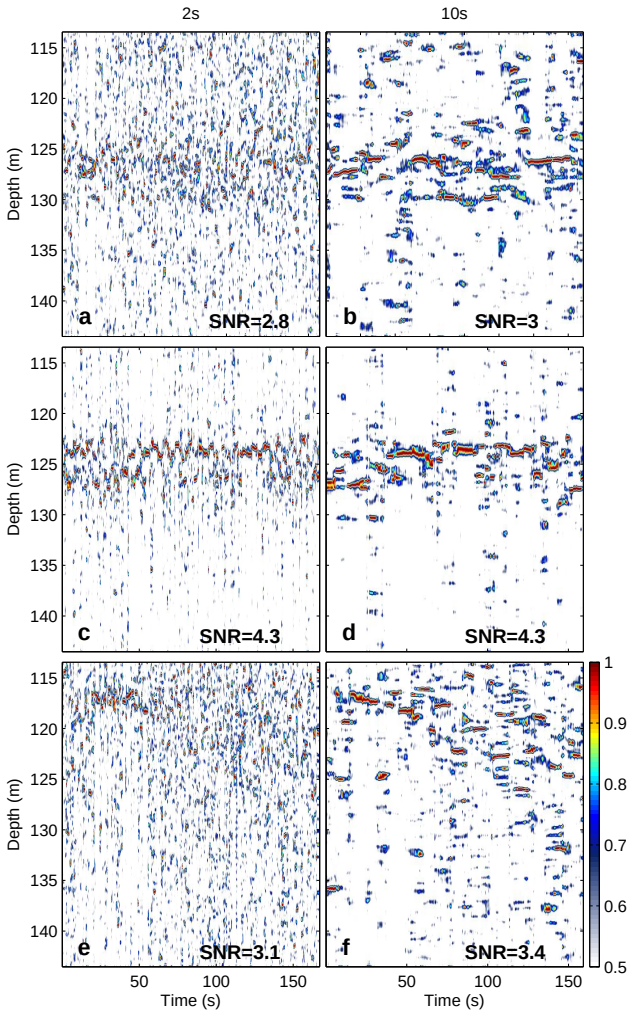

Figure 5.3: (Color online) Envelope of the passive fathometer from regions (a)–(b) I, (c)–(d) II and (e)–(f) III as defined in Fig. 5.1 obtained with correlation times of 2 and 10 s using 0.34 s snapshots with 50% overlap. The horizontal-axis shows the relative start time of each snapshot.

the seabed as the array drifts, or motion of the array. At 2 s correlation time [Fig. 5.3(a)], the seabed reflection peaks appear sporadically in time and are difficult to distinguish from spurious peaks.

The response from region II with 2 s correlation time[Fig. 5.3(c)] shows a higher SNR than region I and the correlation peaks from 2 reflecting layers oscillate around 124–126 m depth. The oscillations are 1 m in amplitude and occur with a 7 s period which is consistent with surface-wave driven motion of the array, which is tethered to a surface buoy.

Using 10 s correlation time [Fig. 5.3(d)] on the data from region II destroys the evidence of the short period array motion and does not increase the SNR of the seabed reflection peak as the motion of this reflection peak causes destructive interference.

The reflection peak from region III, is obtained only an hour after region II however the background noise is much larger [Fig. 5.3(e)–(f)] likely due to interfering noise [Fig. 5.2(c) and (f)].

MVDR processing

The processing from Sec. 5.3.2 was repeated MVDR steering vectors (Fig. 5.4). The MVDR results are similar to the conventional but the SNR for all thee regions is larger with 10 s correlation time, consistent with the larger attenuation of horizontal interference provided by MVDR processing.

The reflection peak depths in region I remain almost constant [Fig. 5.4(b)] whereas in regions II and III the peak depth changes suggesting that when 90 s averaging is used, as in Fig. 5.1(a)–(d) and in Ref. [9] the data from region I would be expected to give good results while the reflection peaks from regions II and III would be expected to attenuate due to destructive interference.

Using multi-scale MVDR processing, steering vectors were formed with averaging times of 2 and 10 s (10 and 57 snapshots) and applied to 0.34 s data snapshots (Sec. 5.2.3) from data from region II (Fig. 5.5)

The standard MVDR algorithm shows that averaging larger times obscures the second-scale motion of the array and produces only a single flat trace when

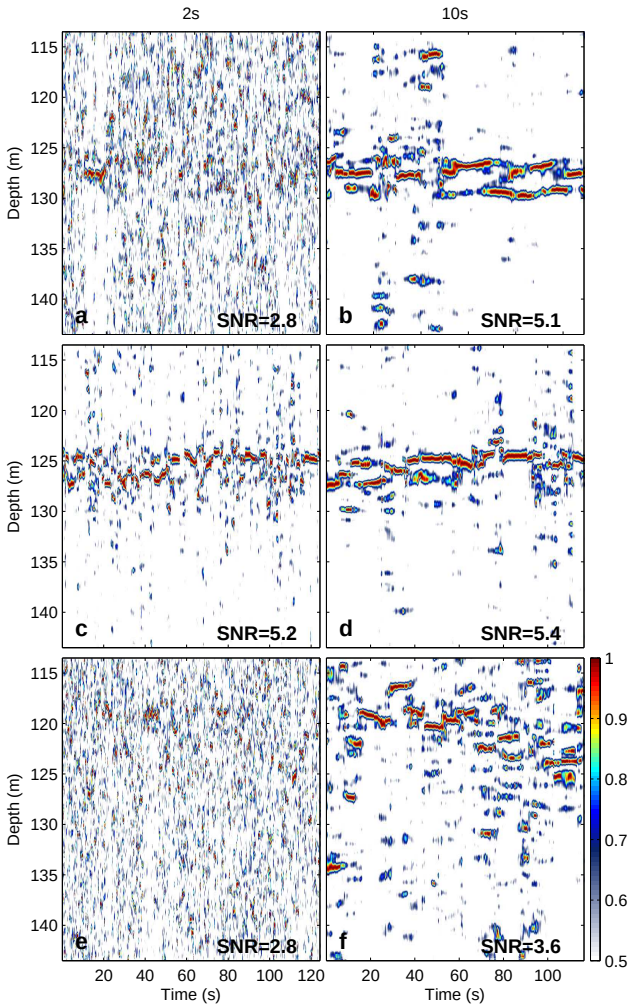

Figure 5.4: (Color online) Envelope of the MVDR passive fathometer response from the same data as Fig. 5.3 using 0.34 s snapshots with 50% overlap.

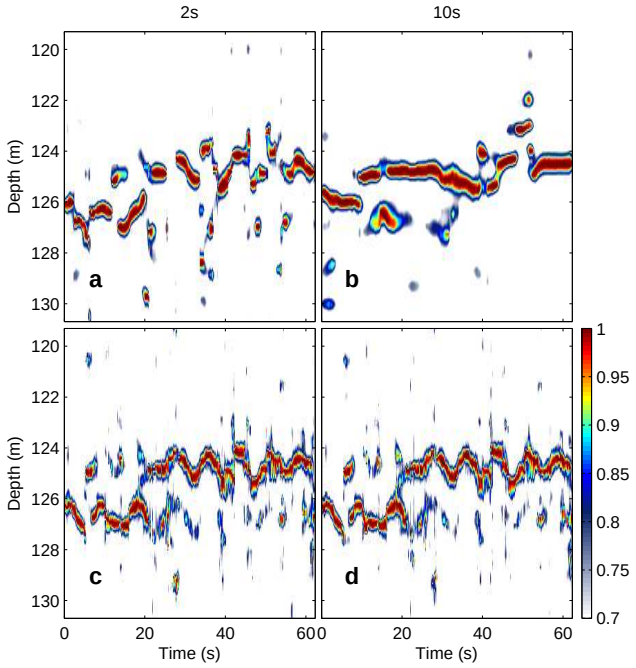

Figure 5.5: (Color online) MVDR passive fathometer response from the same data as Fig. 5.3(c)–(d) processed with (a)–(b) the CSDM formed from 2 and 64 s and (c)–(d) the same CSDMs used to form steering vectors which were applied to the individual 0.34 s snapshots.

10 s averaging time is used [Fig. 5.5(b)]. The results obtained with multi-rate MVDR processing, with steer vectors obtained from 2 and 10 s averaging applied to 0.34 s snapshots [Fig. 5.5(c)–(d)], give a continuous reflection peak that oscillates consistent with surface wave driven motion. Increasing the averaging time has little effect on the reflection trace although the SNR increases.

5.3.3 Coherent averaging

The reflection peak in Fig. 5.3(c) oscillates with a 1 m amplitude and a 7 s period. This is consistent with motion induced by short period surface waves which, as the array is connected to a surface buoy, might induce a vertically oscillating motion of the array.

A peak finder tracked the peak of the envelope of the fathometer response to estimate the motion of the array (Fig. 5.6) and this was used to align each snapshot of the fathometer response.

Two closely spaced reflecting layers are present in the fathometer response [Fig. 5.6(a)] which appear in the incoherent average [Fig. 5.6(g)]. The coherent average [Fig. 5.6(h)] does not show the peaks as the motion introduces destructive interference in the averaging process. Realignment removes this interference and allows the two reflection peaks to be obtained with higher resolution than incoherent averaging [Fig. 5.6(i)]. The alignment allows the seabed reflection peaks to be summed coherently and retain the phase, such that the fathometer response waveform can be computed [Fig. 5.6(l)].

5.3.4 Emergence time

To estimate the emergence time, the SNR of the reflection peak for the thee data regions was computed as a function of correlation time with and without alignment of the peak (Fig. 5.7). The 170 s of data from each region was divided into blocks and each block was averaged in time. The SNR was computed for each block by dividing the maximum peak within ± 2 m of the seabed reflection by the standard deviation of the response outside ± 2 of the reflection peak.

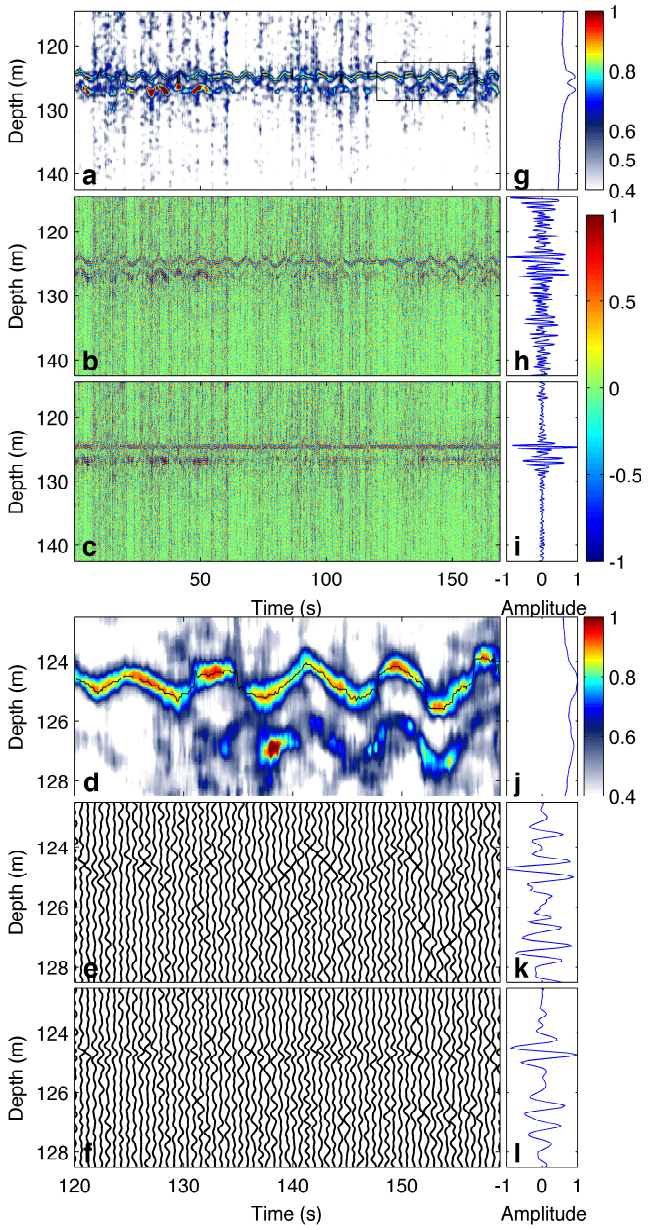

Figure 5.6: (Color online) (a) Envelope, (b) waveform and (c) aligned waveform of the passive fathometer response over a 170 s interval at 1549Z 12 May 2004. A peak tracker has been implemented on the envelope and the output of this tracker has been used to align the waveforms. The (g) incoherent (h) coherent and (i) aligned coherent averages. The region in the box is shown in detail for the (d) envelope, (e) waveform and (f) aligned coherent waveforms and (j)–(l) their respective averages over the 30 s period.

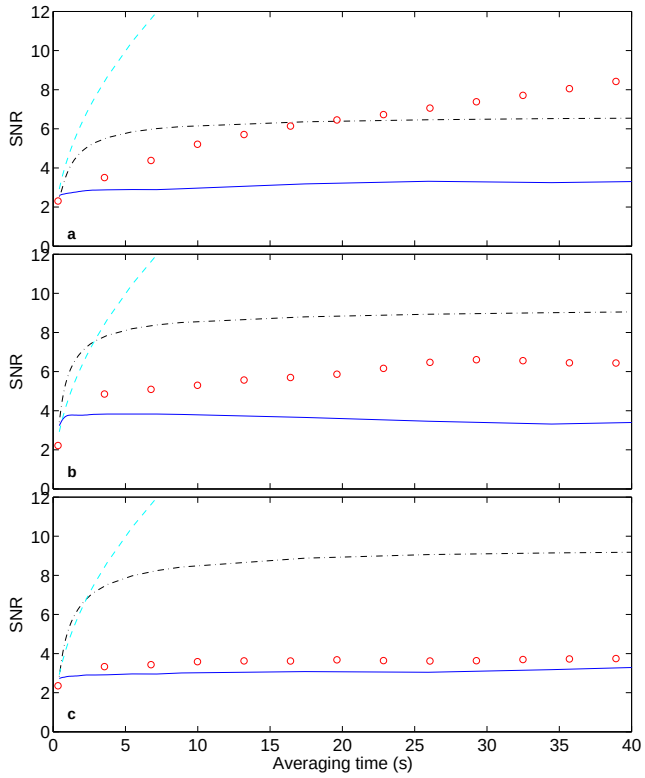

Figure 5.7: (Color online) SNR obtained by the passive fathometer algorithm with (dash-dot) and without (solid) alignment from the peak tracker as a function of correlation time for the data from sections (a) I, (b) II and (c) III as defined in Fig. 5.1. Also shown are the SNR of the MVDR passive fathometer response without alignment (circles) and the SNR predicted by the 1D theory (dashed).

Varying the averaging time from 0.3–40 s the SNR from region I obtained with conventional beamforming and no alignment increases slowly but monotonically from 2–3.5. The MVDR SNR increases from 2–8. The aligned fathometer SNR increases faster than the other traces reaching 6 with an averaging time of 4 s and remains constant as the averaging time is increased. None of the outputs perform as well as predicted by the 1D theory which does not account for spherical spreading or horizontal interference. Also the 1D theory is derived assuming an ideal waveguide environment and does not account for fluctuations in the noise field or motion of the array. However the SNR increases monotonically for all the fathometer responses. This data set showed good results when processed with 90 s correlation time[9].

The SNR from region II obtained with plane-wave beamforming increases quickly, reaching an SNR of 4 in 1 s of averaging time. However as the averaging time is increased beyond 1 s the SNR attenuates slightly. This is consistent with destructive interference introduced by averaging a moving peak. The SNR only grows as long as the averaging time is significantly smaller than the surface wave period. The MVDR passive fathometer similarly reaches a peak of 6 with 30 s averaging time and then attenuates as more averaging time is included. The SNR of the aligned fathometer response performs similarly the as in region I reaching an SNR of 8 with 5 s averaging time and remaining constant as more time is included.

The SNR in region III is similar to that in region II with the unaligned SNR never increasing above 4 and the aligned SNR reaching 8 with 5 s averaging time and remaining constant as averaging time is increased.

Sub-bottom structure

The alignment procedure in Sec. 5.3.3 increases the sensitivity of the fathometer as the SNR of weak reflecting layers is increased (Fig. 5.6).

Multirate MVDR beamforming was used with steer vectors formed from 90 s of data and applied to rank-1 CSDM estimates formed from 0.34 s snapshots. The alignment algorithm was applied and the output averaged over 11 s blocks. This was repeated for the entire 2004 drift experiment [Fig. 5.8(b)] and the final result

was smoothed with a median filter over 90 s blocks. Sections in which the amplitude of the recorded data was anomalously high were removed prior to processing.

The fathometer response obtained with multirate MVDR beamforming and alignment [Fig. 5.8] shows the primary reflecting layer more clearly than the MVDR passive fathometer algorithm [Fig. 5.1(d)] and a a sub-bottom reflector is visible which was obscured with the basic MVDR processing.

5.4 Conclusion

In a stationary environment the seabed reflection peak obtained from the passive fathometer improves with longer correlation time. In practice, the oceanic environment is non-stationary and too long an correlation time introduces destructive interference which attenuates the seabed reflection peak.

In cases where the drifting array is driven by wave motion this may limit the performance of the passive fathometer algorithm and prevent extraction of seabed reflections, except in the cases where the growth of SNR is rapid enough that the seabed depth can be determined with a second of correlation time. In this case a peak-tracking algorithm may be utilized to increase the reflection peak SNR and allow sub-bottom profiling. However, as the growth of the reflection peak SNR increases with the presence of non-vertical interfering noise, this reliance on short correlation times limits the efficacy of this algorithm to periods of low interfering noise.

MVDR processing reduces the effect of interfering noise and can dramatically improve the response of the passive fathometer. This technique requires the data CSDM to be inverted which requires averaging over multiple snapshots to achieve a full-rank matrix. This increases the necessary correlation time. If the interfering noise is stationary for a longer time than the surface wave period, multi-rate MVDR beamforming can be used with the MVDR steering computed with CSDMs averaged over several periods of oscillation and applied to short time CSDM snapshots. This stabilizes the CSDM used to obtain the steering vectors which can be applied to rank-1 approximations of the CSDM obtained over a sec-

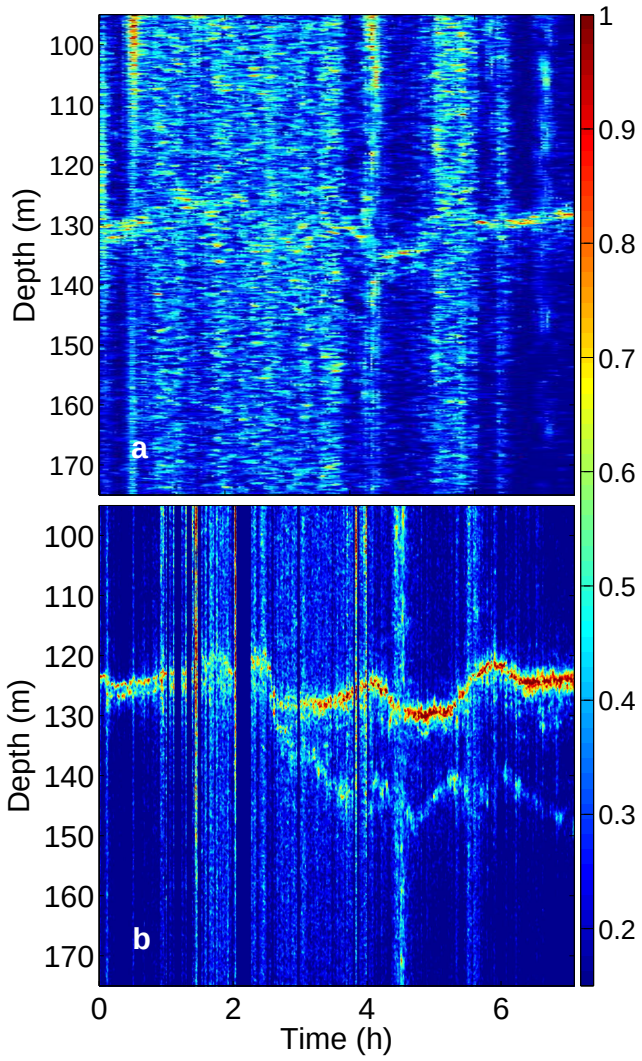

Figure 5.8: (Color online) Envelope of the passive fathometer response for data from May 12 2004 computed with (a) MVDR steer vectors and data CSDM formed from 90 s averages [identical to Fig. 5.1(d)] and (b) multirate MVDR beamforming with steer vectors formed from 90 s averaging applied to 0.34 s snapshots which were aligned and averaged over 11 s.

ond or less of correlation time. This achieves a greater SNR as MVDR processing can be used with high resolution in time.

5.5 Acknowledgements

This work was submitted top the Journal of the Acoustical Society of America for publication in June 2011. Thanks to Chris Harrison and Peter Nielsen from the NATO Undersea Research Centre (NURC) for the experiment data. This work was supported by the Office of Naval Research under grants N00014-08-1-0196 and N00014-11-1-0320.

5.A 1D environment

5.A.1 Correlation peaks

Consider two sensors, separated by d and separated from a reflecting layer by $\xi/2$. A signal $S(t)$, delta-correlated in time, is incident along the axis joining the two sensors. The recorded signals are

$$\begin{aligned} x_2(t) &= S(t - d/c) + r_0 S(t + \xi + d/c) \\ x_1(t) &= S(t) + r_0 S(t + \xi) \end{aligned} \tag{5.12}$$

where the lower sensor x_1 is at the origin. The signal is assumed to be pass-band filtered with a bandwidth B such that the observed signal is convolved with $2B\text{sinc}(2\pi Bt)$.

Assuming the signals are sampled at frequency f_s the cross-correlation of these signals over correlation time T gives

$$\begin{aligned} \langle C(\tau) \rangle &= \frac{1}{T} \int_0^T \langle x_1(t) x_2(t + \tau) \rangle \, dt \\ &= \sigma_0^2 \left[\Delta\left(\tau + \frac{d}{c}\right) + r_0 \Delta\left(\tau \pm \frac{\xi - d}{c}\right) \right] , \end{aligned} \tag{5.13}$$

where the r_0^2 term has been neglected, the signal variance for a single data point is

$$\sigma_0^2 = \left\langle S(t)^2 \right\rangle \tag{5.14}$$

and $\Delta(\tau - t)$ is the Dirac measure

$$\begin{aligned} \Delta(\tau - t) &= \begin{cases} 1 & \tau = t \\ 0 & \tau \neq t \end{cases} \\ \int \Delta(\tau - t)\, d\tau &= \frac{1}{f_s}\,, \end{aligned} \tag{5.15}$$

since $1/f_s$ is the width of one bin.

Convolving Eq. (5.13) by $2B\text{sinc}(2\pi Bt)$, gives

$$\langle C(\tau)\rangle = r_0\sigma_0^2\frac{2B}{f_s}\,. \tag{5.16}$$

5.A.2 Variance

The variance of the signal recorded by the sensors $x_{1,2}$ is $\langle C(\tau)^2\rangle - \langle C(\tau)\rangle^2$. Evaluating the first term gives

$$\begin{aligned} \left\langle C(\tau)^2\right\rangle &= \frac{1}{T^2}\int_0^T\int_0^T \langle x_1x_2x_3x_4\rangle \,\mathrm{d}t\mathrm{d}t' \\ \langle x_1x_2x_3x_4\rangle &= \langle x_1(t)x_2(t+\tau)x_1(t')x_2(t'+\tau)\rangle \\ &= \langle x_1x_2\rangle\langle x_3x_4\rangle + \langle x_1x_3\rangle\langle x_2x_4\rangle + \langle x_1x_4\rangle\langle x_2x_3\rangle \\ &= I(\tau) + J(\tau) + K(\tau) \end{aligned} \tag{5.17}$$

where the 4th order statistical moment has been decomposed into the sum of thee 2nd order moments[24]. Evaluating the first term[24] yields $\langle C(\tau)\rangle^2$ such that

$$\text{Var}\left\{C(\tau)\right\} = J(\tau) + K(\tau)\,. \tag{5.18}$$

The second term gives

$$\begin{aligned} J(\tau) &= \frac{1}{T^2}\int_0^T\int_0^T\langle x(t)x_1(t')\rangle\langle x_2(t'+\tau)x_4(t'+\tau)\rangle \,\mathrm{d}t\mathrm{d}t' \\ &= \frac{\sigma_0^4}{T^2}\int_0^T\int_0^T\Delta(t-t')\,\mathrm{d}t\mathrm{d}t' = \frac{\sigma_0^4}{Tf_s} \end{aligned} \tag{5.19}$$

and the final term

$$\begin{aligned} K(\tau) &= \frac{1}{T^2}\int_0^T\int_0^T\langle x(t)x_4(t'+\tau)\rangle\langle x_2(t'+\tau)x_1(t')\rangle \,\mathrm{d}t\mathrm{d}t' \\ &= \frac{\sigma_0^4}{T^2}\int_0^T\int_0^T\Delta(t-t')\Delta(t-\tau)\,\mathrm{d}t\mathrm{d}t' = \frac{\sigma_0^4}{(Tf_s)^2} \end{aligned} \tag{5.20}$$

As the $K(\tau)$ decays with $(Tf_s)^2$ it can be neglected relative to $J(\tau)$. As the signal is bandpass filtered the variance is rescaled by $2B/f_s$

$$\text{Var}\left\{C(\tau)\right\} \;=\; \frac{2\sigma_0^4 B}{T f_s^2}\;. \tag{5.21}$$

5.A.3 Signal-to-noise ratio

The signal-to-noise ratio (SNR) of the seabed reflection peak is obtained by dividing Eq. (5.16) by the square-root of Eq. (5.21) to give

$$SNR_{1D} = r_0\sqrt{\frac{TB}{2}} \tag{5.22}$$

which is dependent on the time-bandwidth product consistent with similar models[24].

Bibliography

[1] M. Siderius, C. H. Harrison, and M. B. Porter, "A passive fathometer technique for imaging seabed layering using ambient noise," J. Acoust. Soc. Am. **120**, 1315–1323 (2006).

[2] C. H. Harrison and M. Siderius, "Bottom profiling by correlating beam-steered noise sequences," J. Acoust. Soc. Am. **123**, 1282–1296, (2008).

[3] P. Gerstoft, W. S. Hodgkiss, M. Siderius, C. F. Huang, and C. H. Harrison, "Passive fathometer processing," J. Acoust. Soc. Am. **123**, 1297–1305, (2008).

[4] C. H. Harrison Anomalous signed passive fathometer impulse response when using adaptive beam forming," J. Acoust. Soc. Am. **125**, 3511–3513 (2009).

[5] J. Traer, P. Gerstoft, H. C. Song, and W. S. Hodgkiss "On the sign of the adaptive passive fathometer impulse response," J. Acoust. Soc. Am. **126**, 1657–1658 (2009).

[6] J. Gebbie, M. Siderius, L. Muzi and J. Paddock "Extracting the Rayleigh reflection coefficient from the passive fathometer," IEEE Oceans, Seattle (2010).

[7] J. Traer, P. Gerstoft, and W. S. Hodgkiss, "Ocean bottom profiling with ambient noise: A model for the passive fathometer," J. Acoust. Soc. Am. **129**, 1825–1836, (2011).

[8] S. L. Means and M. Siderius, "Effects of sea-surface conditions on passive fathometry and bottom characterization," J. Acoust. Soc. Am. **127**, 2193–2200 (2010).

[9] M. Siderius, H. C. Song, P. Gerstoft, W. S. Hodgkiss, and C. H. Harrison, "Adaptive passive fathometer processing," J. Acoust. Soc. Am. **126**, 2234–2241, (2010).

[10] B. F. Cron and C. H. Sherman, "Spatial Correlation Functions for Various Noise Models ," J. Acoust. Soc. Am., **34**, 1732–1736, (1962)

[11] W. A. Kuperman and F. Ingenito Spatial correlation of surface generated noise in a stratified ocean," J. Acoust. Soc. Am. **67**, 1988–1996 (1980).

[12] M. J. Buckingham, "Theory of acoustic attenuation, dispersion, and pulse propagation in unconsolidated granular materials including marine sediments," J. Acoust. Soc. Am., **102**, 2579–2596 (1997).

[13] P. Roux and W. A. Kuperman "Extracting coherent wave fronts from acoustic ambient noise in the ocean," J. Acoust. Soc. Am. **116**, 1995–2005 (2004).

[14] L. A. Brooks and P. Gerstoft "Green's function approximation from cross-correlations of 20–100 Hz noise during a tropical storm," J. Acoust. Soc. Am. **125**, 723–734 (2009).

[15] L. A. Brooks and P. Gerstoft, "Multichannel array diagnosis using noise cross-correlation," J. Acoust. Soc. Am. **124**, EL203–EL209, (2008).

[16] J. Krolik and D. Swingler, "Multiple Broad-Band Source Location Using Steered Covariance Matrices," lEEE Trans. Acoust., Speech, Signal Processing, **37**, 1481–1494, (1989).

[17] P. Gouédard, L. Stehly, F. Brenguier, M. Campillo, Y. Colin de Verdière, E. Larose, L. Margerin, P. Roux, F. J. Sánchez-Sesma, N. M. Shapiro and R. L. Weaver "Cross-correlation of random fields: mathematical approach and applications," Geophys. Prospecting **56**, 375–393 (2008).

[18] J. Rickett and J. Claerbout, "Acoustic daylight imaging via spectral factorization: Helioseismology and reservoir monitoring," The Leading Edge **18**, 957–960 (1999).

[19] R. L. Weaver and O. I. Lobkis "Ultrasonics without a source: Thermal fluctuation correlations at MHz frequencies," Phys. Rev. Lett. **87**, 134301 (2001).

[20] R. Snieder, "Extracting the Green's function from the correlation of coda waves: a derivation based on stationary phase," Phys. Rev. **69**, 046610 (2001).

[21] K. G. Sabra, P. Gerstoft, W. A. Kuperman and M. C. Fehler Extracting time-domain Green's function estimates from ambient seismic noise," Geophys. Res. Lett. **32**, L03310

[22] P. Gouedard, P. Roux, M. Campillo, and A. Verdel, "Convergence of the two-point correlation function toward the Green's function in the context of a seismic-prospecting data set," Geophys. **73**, V47–V53 (2008).

[23] R. L. Weaver and O. I. Lobkis, "Fluctuations in diffuse fieldfield correlations and the emergence of the Greens function in open systems," J. Acoust. Soc. Am., **117**, 3432–3439 (2005).

[24] K. G. Sabra, P. Roux and W. A. Kuperman, "Emergence rate of the time-domain Green's function from the ambient noise cross-correlation function", J. Acoust. Soc. Am. **118**, 3524–3531, (2005).

[25] C. H. Harrison, "Performance and limitations of spectral factorization for ambient noise sub-bottom profiling," J. Acoust. Soc. Am. **118**, 2913–2923, (2005).

[26] H. Cox, "Mult-rate adaptive beamfroming (MRABF)", Proceedings of the 2000 lEEE, 306–309, (2000).

[27] O. Godin, "Emergence of the acoustic Green's function from thermal noise," J. Acoust. Soc. Am. **121**, EL97–EL102 (2007).

[28] O. Godin, "Accuracy of the deterministic travel time retrieval from cross-correlations of non-diffuse ambient noise," J. Acoust. Soc. Am. **126**, EL183–EL189 (2009).

Chapter 6

Conclusion

The acoustic signals generated by tropical storms Ernesto and Florence (2006) were measured, both with seabed mounted hydrophones and land-based seismometers. Although Double Frequency (DF) acoustic signatures, characteristic of wave-wave interactions were recorded by the hydrophones the acoustic signature in the ocean and the seismic signature recorded on land exhibited many differences in temporal and spectral variation, suggesting a non-linear interaction between acoustic signals at the seabed and propagating seismic signals.

Tropical storm Ernesto traveled close to shore and eventually passed onto land, producing large waves in shallow waters on the continental shelf. Florence remained in deep water. Both storms produced similar seismic signals, despite the larger wave heights and surface area of Florence suggesting that interaction with coastlines and shallow water regions is an important factor for microseism generation.

Adaptive array processing techniques can increase the resolution and sensitivity of ambient noise measurements and therefore can increase the performance of geophysical inversion from ambient noise measurements. Application of Minimum-Variance Distortionless Response (MVDR) beamforming to the passive fathometer will, in theory, improve the response of the passive fathometer in the presence of interfering noise. In practice, it also results in the application of a negative multiplicative factor to the response. This is explained by an eigenvalue decomposition of the Cross-Spectral Density Matrix (CSDM) which shows that MVDR process-

ing retains all the same components as plane wave beamforming but rescales the components by different factors. These multiplicative rescaling factors increase the height of the seabed reflection relative to incoherent noise and, as the rescaling factor is negative for the seabed reflection, flip the waveform of the response consistent with experimental observations.

This eigenvalue decomposition of the CSDM could be applied to a more complicated noise model that included an infinite sheet of surface noise and discrete interferers. Such a noise model was used to describe the asymptotic passive fathometer response with both plane-wave and MVDR beamforming. The leading order term is shown to correspond to the multipath structure of vertically propagating noise and hence yield the seabed structure. MVDR processing is shown to attenuate non-vertically propagating signal.

A theory for the Signal-To-Noise (SNR) of the passive fathometer response as a function of averaging time is presented. As, in a dynamic environment such as the ocean, the time available for averaging may be limited this is an important consideration for robust geophysical inversion. Using short averaging times a passive fathometer was used to detect a seabed reflection using less than a second of data. Such resolution showed the array moved with ocean surface waves which, when the amplitude of this motion was large enough, resulted in lower SNR than measurements made in similar acoustic environments with a stationary array. Application of a peak tracker to infer the array motion and realign the fathometer response from subsequent snapshots allowed averaging times larger than the period of the wave motion to be used without destructive interference.